Coherent Raman Scattering: Methods Towards Imaging with High Sensitivity

by

Brandon Richard Bachler

A dissertation submitted in partial fulfillment
of the requirements for the degree of
Doctor of Philosophy
(Physics)
in The University of Michigan
2012

Doctoral Committee:

Assistant Professor Jennifer P. Ogilvie, Chair
Professor Zhan Chen
Professor Eitan Geva
Professor Jean Krisch
Professor Jens-Christian Meiners

This work is dedicated to my wife, Carrie.

ACKNOWLEDGEMENTS

Coming to Michigan in my first year of graduate school, my mind was made up to specialize in experimental high-energy physics. Throughout my undergraduate career, I worked with particle detection for dark matter for Professor Daniel Akerib at Case Western Reserve University, who instilled in me a passion for devising clever ways of detecting what our eyes cannot see. My natural instinct was to progress from dark matter detection to high energy particle detection – an idea that was only solidified with the (then) upcoming completion of the LHC.

My first week or two at Michigan, I attended a seminar by Professor Jennifer Ogilvie regarding the observation of ultrafast time dynamics of molecules using femtosecond laser pulses. My interest was immediately piqued by her presentation, and before I knew it, I was working in her group in an area with which I had no experience. It was the best decision I made during graduate school. The passion with which she approaches science is truly remarkable, and I have a great deal of admiration for her knowledge and integrity. She embodies exactly what I strive to be as a scientist, and I am extremely grateful for all that she's done for me during my time at Michigan.

In a similar way, I have a great deal of admiration for Meng Cui, the graduate student who worked on the coherent Raman microscopy projects before me. The times that I worked with him were always a pleasure, as his superior ability as a scientist was readily apparent. I have constantly tried to emulate his proficiency in the lab, and even when I came up short, he has always served as a role model for me.

Sarah Nichols joined our group at the beginning on 2009 as a postdoctoral fellow, and I worked with her for two years on various Raman microscopy projects. She taught me a great deal about how to be a better scientist, and she always had great insight for our experiments. I have worked off and on with Meredith Brenner, who has helped me tremendously with several projects that I would not have been able to finish alone. I admire her extraordinary work ethic, and I am grateful for the great conversation she has provided me during long days in the lab.

Kristin Lewis and Jeff Meyers joined the group at the same time as me, and we shared our mutual experience throughout graduate school. They have always been great to talk to, and I am thankful that I was able to have them for support. Dan Wilcox and Franklin Fuller have always been extremely insightful members of our group, and I am thankful for all of the tough questions they ask. I appreciate their dedication to understanding the material well. With the more recent additions of Anton Loukianov, Daniel Flynn, Seckin Senlik, and Dawen Cai to our group, I know that the future of science in our lab is in good hands.

I want to thank my committee members Professors Geva, Chen, Krisch, and Meiners for helping me through the final stages of my time here at Michigan. They took on this task on relatively short notice, and for that I am very grateful. The time they are devoting to ensure my success will forever be appreciated.

I want to thank my parents, Joan and Richard Bachler. They have always encouraged me to pursue my education as far as I want to, and they have always provided the means to do so. They have been incredibly supportive of me throughout this whole process, and I hope that I may some day repay them for all they've done for me.

More than anyone, I want to thank my wife, Carrie. She has supported me in every way imaginable, and there is nothing I can do to thank her enough. I have never met a more caring and generous individual in my life, and if it weren't for her, I never would have made it through graduate school. From cooking some of the best food I've ever eaten to providing emotional support during the most stressful of times, she has done everything I could ask and more.

TABLE OF CONTENTS

DEDICATION ii

ACKNOWLEDGEMENTS iii

LIST OF FIGURES viii

LIST OF ABBREVIATIONS xii

ABSTRACT xiv

CHAPTER

I. Introduction 1

1.1 Motivation for Raman Microscopy 1
1.2 Third-order Nonlinear Susceptibility 7
1.3 Nonresonant Signal Suppression 8
1.4 Thesis Outline and Chapter Overview 9

II. Theory 15

2.1 Spontaneous Raman scattering 15
2.2 Coherent anti-Stokes Raman Scattering 21
2.3 Stimulated Raman Spectroscopy 24
2.4 Raman-induced Kerr Effect scattering 26
  2.4.1 Signal to noise of RIKES 29
2.5 Surface-enhanced Raman scattering 31
  2.5.1 Surface-enhanced coherent anti-Stokes Raman scattering 33

III. Coherent versus spontaneous Raman 39

3.1 Motivation 39
3.2 History 41

- 3.3 Experimental Setup . . . 43
- 3.4 Measurements in solution . . . 48
- 3.5 Imaging polystyrene beads . . . 53
- 3.6 Calculation . . . 57
- 3.7 Discussion . . . 61
- 3.8 Conclusions . . . 62

IV. Multiplexed Raman-induced Kerr Effect Microscopy . . . 70

- 4.1 Introduction . . . 70
- 4.2 History . . . 73
- 4.3 Birefringent background . . . 74
- 4.4 Experimental Setup . . . 76
- 4.5 Experimental Results . . . 80
  - 4.5.1 RIKES Spectroscopy . . . 80
  - 4.5.2 RIKES Microscopy . . . 89
- 4.6 Discussion . . . 98
- 4.7 Conclusions . . . 100

V. Surface-enhanced Raman Spectroscopy . . . 106

- 5.1 Introduction . . . 106
- 5.2 History . . . 108
- 5.3 Introduction to Surface Plasmons . . . 111
- 5.4 Experimental Setup and Previous Results . . . 114
- 5.5 Experimental Results . . . 124
- 5.6 Conclusions and Future Directions . . . 139

VI. Conclusion . . . 145

- 6.1 Future Directions . . . 147

LIST OF FIGURES

Figure

1.1 Energy level diagram for fluorescence. 2

1.2 Spontaneous Raman energy level diagram 4

1.3 Raman spectrum of P22 virus with expanded fingerprint region . . . 5

1.4 Energy level diagram for the coherent anti-Stokes Raman scattering (CARS) process 6

1.5 Energy level diagrams of coherent anti-Stokes Raman scattering, coherent Stokes Raman scattering, the nonresonant background, stimulated Raman scattering, and the Raman-induced Kerr effect 8

2.1 Spontaneous Raman energy level diagram 15

2.2 CARS, CSRS, nonresonant background, and SRS/RIKES energy level diagrams 21

2.3 Stimulated Raman scattering energy level diagram 24

2.4 Energy level diagram for the Raman-induced Kerr effect (RIKES) process 27

2.5 Incident beam geometry for surface-enhanced coherent anti-Stokes Raman scattering with a spherical particle 34

3.1 Experimental setup of original coherent anti-Stokes Raman scattering experiment by Maker and Terhune 42

3.2 Experimental results of Pestov's coherent versus spontaneous Raman comparison 44

3.3 Energy level diagram for coherent Stokes Raman scattering 45

3.4 Spectrum of Ti:sapph oscillator 46

3.5 Amplitude mask used for three-color coherent Stokes Raman scattering experiment with polystyrene 47

3.6 Experimental diagram for CSRS versus spontaneous Raman scattering measurement 48

3.7 Autocorrelation for three pulses in CSRS versus spontaneous Raman measurement 49

3.8 Spontaneous Raman spectrum for 2-propanol 51

3.9 Coherent Stokes Raman scattering versus spontaneous Raman scattering data and fit in solution of 2-propanol 52

3.10 Critical power of solution of 2-propanol for CSRS and Raman . . . 53

3.11 Coherent Stokes Raman scattering image of 7.3 micron diameter polystyrene beads with spectrum 54

3.12 Coherent Stokes Raman scattering image of 4.3 micron diameter polystyrene beads with spectrum 54

3.13 CSRS versus spontaneous Raman images for 7.3 micron beads with spectra 56

3.14 CSRS versus spontaneous Raman images for 4.3 micron beads with spectra 58

3.15 CSRS versus spontaneous Raman signal strength ratio as a function of power and concentration 63

4.1 Energy level diagrams for various types of coherent Raman spectroscopy, including CARS, RIKES/SRS, and multiplex RIKES/SRS. 72

4.2 Experimental setup of the original Raman-induced Kerr effect experiment by Levenson. 74

4.3 Experimental setup of single band RIKES microscopy by Freudiger, et al. 75

4.4 Experimental setup of our RIKES microscopy experiment 77

4.5 Polarization purity of beamsplitter as a function of linear polarization orientation 78

4.6 Spectrum of continuum generated with Corning Hi980 fiber 81

4.7 Raman-induced Kerr effect spectrum of carbon disulfide 82

4.8 FSRS versus RIKES for carbon disulfide 84

4.9 Spectrum of continuum generated with broadband fiber 85

4.10 Spontaneous Raman spectra for polystyrene and toluene 87

4.11 FSRS versus RIKES for toluene, unchopped 88

4.12 Unchopped versus chopped spectrum of toluene 88

4.13 RIKES imaging of 10 μm polystyrene beads without chopping scheme as a function of frequency 90

4.14 RIKES imaging of 10 μm polystyrene beads with and without chopping scheme 92

4.15 RIKES imaging of 10 μm polystyrene beads in cytoseal versus excitation power 93

4.16 FSRS versus RIKES images of polystyrene beads 95

4.17 Raman-induced Kerr effect images of onion cells 96

4.18 Sign flipping phenomenon in RIKES onion images 97

5.1 Experimental configuration for original surface-enhanced Raman observation by Fleischmann 109

5.2 Experimental configuration for surface-enhanced coherent anti-Stokes Raman scattering (SECARS) measurement by Shen et al. 110

5.3 Diagrams of the Otto configuration and Kretschmann configuration for the excitation of surface plasmon waves 113

5.4 SEM images of the nanostructured metal substrate 115

5.5 Picture of Klarite® substrate mounted on glass slide 116

5.6 Diagram of simulated plasmon resonance locations and strengths in metal substrate . . . 116

5.7 Reflection spectra of Klarite® surface for coated and uncoated nanostructured substrate . . . 117

5.8 Experimental setup diagram for surface-enhanced Raman scattering (SERS) experiment . . . 119

5.9 Pictures of experimental setup of 4f pulse shaper and pulse picker . 120

5.10 Spontaneous Raman spectrum for benzenethiol . . . 122

5.11 FTCARS results for benzenethiol adsorbed on Klarite® substrate . 123

5.12 Picture of Klarite® used in our experiment, with measurement locations 1-5, A, B indicated . . . 124

5.13 Surface-enhanced spontaneous Raman data (taken in Morris lab) for benzenethiol adsorbed on structured portion of Klarite® substrate . 125

5.14 Spontaneous Raman data (taken in Morris lab) for benzenethiol adsorbed on flat portion of Klarite® substrate . . . 126

5.15 Coherent and spontaneous Raman data on nanostructured portion of Klarite® . . . 128

5.16 Nonresonant and resonant data in polystyrene for comparison . . . 129

5.17 Surface-enhanced CSRS data for various combinations of pump and probe beams . . . 133

5.18 Surface-enhanced CSRS data from benzenethiol on Klarite® substrate for various probe delay times . . . 135

5.19 Surface-enhanced CSRS data from Klarite® substrate without benzenethiol . . . 136

LIST OF ABBREVIATIONS

CARS	Coherent anti-Stokes Raman scattering
CCD	Charge-coupled device
CSRS	Coherent Stokes Raman scattering
CW	Continuous wave
EOM	Electro-optic modulator
FWM	Four-wave mixing
LSPR	Localized surface plasmon resonance
MIIPS	Multiphoton intrapulse interference phase scan
NA	Numerical aperture
NR	Nonresonant
PMT	Photomultiplier tube
PUSCARS	Pulse-sequenced coherent anti-Stokes Raman scattering
RIKES	Raman-induced Kerr effect spectroscopy
SECARS	Surface-enhanced coherent anti-Stokes Raman scattering
SEM	Scanning electron microscope
SERS	Surface-enhanced Raman scattering
SHG	Second harmonic generation
SLM	Spatial light modulator
SPM	Self-phase modulation
TDCARS	Time-delay coherent anti-Stokes Raman scattering

THG Third harmonic generation

TM Transverse magnetic

ABSTRACT

Coherent Raman Scattering: Methods Towards Imaging with High Sensitivity

by

Brandon Richard Bachler

Chair: Jennifer P. Ogilvie

Coherent Raman spectroscopy is a powerful tool for molecular identification. For imaging applications, Raman spectroscopy techniques have offered a way of achieving endogenous chemical contrast without the need for fluorescent labeling. Increasing the sensitivity of Raman scattering microscopy is vital to performing high speed, chemically selective imaging. This thesis presents three experiments with the ultimate goal of increasing the sensitivity and quantifying limitations of different Raman techniques. The first experiment is a comparison of spontaneous and coherent Raman signal strengths under biological imaging conditions. While it is commonly stated in the literature that coherent Raman techniques provide orders of magnitude higher signal than spontaneous Raman, such a comparison has not been done under the low concentration, low excitation power conditions relevant for biological imaging. We determine a critical power above which coherent Raman methods provide higher signal and below which spontaneous Raman methods provide higher sensitivity. Contrary to what is commonly stated in the literature, spontaneous Raman can provide higher signal levels under common biological imaging conditions.

The second experiment is a demonstration of the first multiplexed Raman-induced Kerr effect (RIKES) microscopy setup to date. We compare the signal-to-noise ratios between femtosecond stimulated Raman (FSRS) and RIKES for spectroscopy applications in solution and for microscopy applications with polystyrene beads. We find that for our samples, RIKES consistently provides a higher signal-to-noise ratio than FSRS for both applications. We also use RIKES microscopy to map out the distribution of cytoplasm in onion cells.

Finally, a surface-enhanced Raman experiment is performed to observe and compare highly enhanced signals for spontaneous and coherent Raman spectroscopy. We use a commercial SERS substrate and observe significantly enhanced spontaneous Raman signals from benzenethiol adsorbed onto the substrate. For coherent Raman techniques, we observe a large background signal that contains no chemical information. We investigate the nature of the background, finding that it is a four-wave mixing signal, likely arising from radiation coupling with surface plasmons on the nanostructured substrate. This background compromises the ability to use surface enhancement for increasing the sensitivity of coherent Raman imaging and sensing applications.

CHAPTER I

Introduction

1.1 Motivation for Raman Microscopy

As a tool, microscopy has progressed from simply a method of identifying features invisible to the naked eye to a way of understanding the very nature of matter. Today, we use imaging techniques to provide important information in a wide realm of disciplines. Doctors rely on X-ray and magnetic resonance imaging to aid in the prevention and treatment of disease. Physicists use scanning electron and atomic force microscopy to explore our world on the nanoscale. Astronomers even use optical imaging techniques to explore our place in the universe.

Standard optical microscopy has long been a tool at the forefront of studying cellular function and structure in both fixed and living samples. In its most basic form, microscopy is a wide field imaging technique that measures properties of light after it impinges on a sample. This has often taken the form of bright field microscopy, in which a sample is placed between the light source and microscope objective, giving the observer a view of the absorption of light through the sample. While this can often provide a beautiful picture of cellular dynamics in the case of biological imaging, very little information is gained beyond what is seen through the eyepiece. In addition, contrast can be extremely low in many samples, making it difficult or impossible to discern any structure at all [1]. As a result, more advanced methods

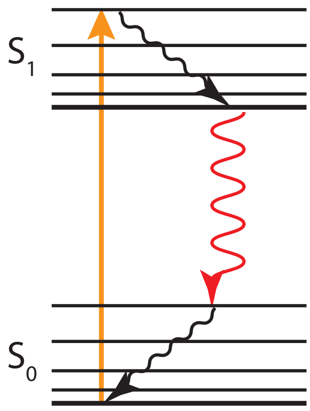

Figure 1.1: Energy level diagram for fluorescence. The orange arrow represents optical excitation to an excited electronic and vibrational state at S_1. The molecule then undergoes vibrational relaxation to the lowest vibrational state in S_1. The red arrow represents Stokes-shifted fluorescence emitted at a lower energy than the excitation light, bringing the molecule back into the ground state, where it again undergoes vibrational relaxation.

of microscopy have been developed to increase contrast and information gained from imaging. Phase contrast, differential interference contrast, dark field, interference reflection, polarization, and fluorescence microscopy have all been used to increase imaging contrast.

Following the pioneering work of Coons and Kaplan, who demonstrated localized staining of tissues and cells with fluorescent markers [2], fluorescence microscopy has become one of the most widely-used methods for biological imaging. The primary advantages offered by fluorescence as an imaging tool are high signal levels and chemical specificity. Fluorescence is a process by which a molecule absorbs a photon with enough energy to excite a higher electronic state and vibrational state of the molecule. Figure 1.1 shows a Jablonski diagram of the fluorescence process. Fast vibrational relaxation within excited electronic state S_1 occurs on the timescale of picoseconds (10^{-12} s). As a consequence of the fast speed of vibrational relaxation, all subsequent relaxation pathways – such as fluorescence – occur from the lowest vibrational state in S_1 [3].

Fluorescence microscopy gained popularity quickly for a number of reasons. 1) The light emitted from fluorescence is shifted spectrally (Stokes-shifted) from the excitation light, allowing spectral filters to isolate the signal with low background. 2) Fluorescent labeling allows the attachment of fluorescent dyes such as green fluorescent protein (GFP) to functional molecules in biological samples [4–7]. Cellular function can be traced by imaging the movement of these labeled molecules. 3) Fluorescence is a strong effect, enabling detection with extremely high (single-molecule) sensitivity [1]. Despite these advantages, however, fluorescence microscopy has a number of limitations that make it unsuitable for many imaging applications. Photobleaching can cause the loss of fluorescence in the dye molecules as the fluorescent molecules become damaged through electronic excitation. This causes a limited observation lifetime before the fluorophores no longer fluoresce. While photobleaching can be exploited to study molecular motion using specialized techniques, such as fluorescence recovery after photobleaching (FRAP) [8] and fluorescence loss in photobleaching (FLIP) [9], it is generally regarded as a serious drawback of fluorescence microscopy. Another limitation of fluorescence microscopy is the formation of oxygen radicals through nonradiative energy transfer upon excitation, which can kill the labeled cell or reduce its function. In cases where the fluorescent dye is much larger than the molecule it is attached to, significant changes in molecular function may be induced. Samples that can be labeled with fluorophores are limited, and finding fluorophores with enough spectral separation to image multiple chemical species is often difficult.

These limitations have necessitated the development of microscopy methods with endogenous chemical contrast. Samples with intrinsic fluorescence are not always available, and nonlinear microscopy modalities are proving to be extremely useful for obtaining endogenous chemical contrast. Second harmonic generation (SHG) [10], third harmonic generation (THG) [11, 12], and self-phase modulation (SPM) [13]

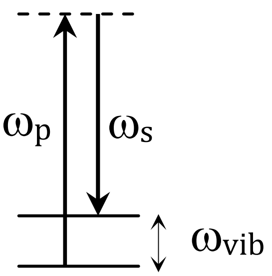

Figure 1.2: Spontaneous Raman energy level diagram. Pump (ω_p) and Stokes (ω_S) fields are shown, with the frequency difference between the two equal to the vibrational energy level frequency (ω_{vib}).

have all been used as modalities for imaging applications. While all of these imaging techniques provide excellent contrast, they do not offer the chemical specificity that can be achieved with fluorescent labels.

Discovered on November 28, 1928, the Raman scattering effect is the inelastic scattering of light off of molecular vibrational states [14]. The Raman scattered photon has an energy difference relative to the incident photon equal to the energy of the excited vibrational level. Figure 1.2 shows the energy level diagram for Raman scattering, where ω_p is the frequency of the incident (pump) photon and ω_S is the frequency of the scattered (Stokes) photon. Because the scattering occurs off a virtual energy level (dotted line), the process is instantaneous, as opposed to fluorescence, which excites an electronic energy level and remains in the excited state on the timescale of nanoseconds. The significance of Raman scattering lies in the fact that the vibrational energy level frequencies ω_{vib} are unique to the scattering medium, allowing the frequency of the scattered light ω_S to be used to identify the molecule being excited. Unlike fluorescence, this is completely endogenous and thus requires no labeling or other potentially disruptive sample treatment.

Figure 1.3 shows a sample spectrum obtained through Raman scattering, plotted as a function of frequency shift from the excitation light in wavenumber (cm^{-1}) [15]. The sample used for this spectrum is the P22 virus, with specific vibrational peaks

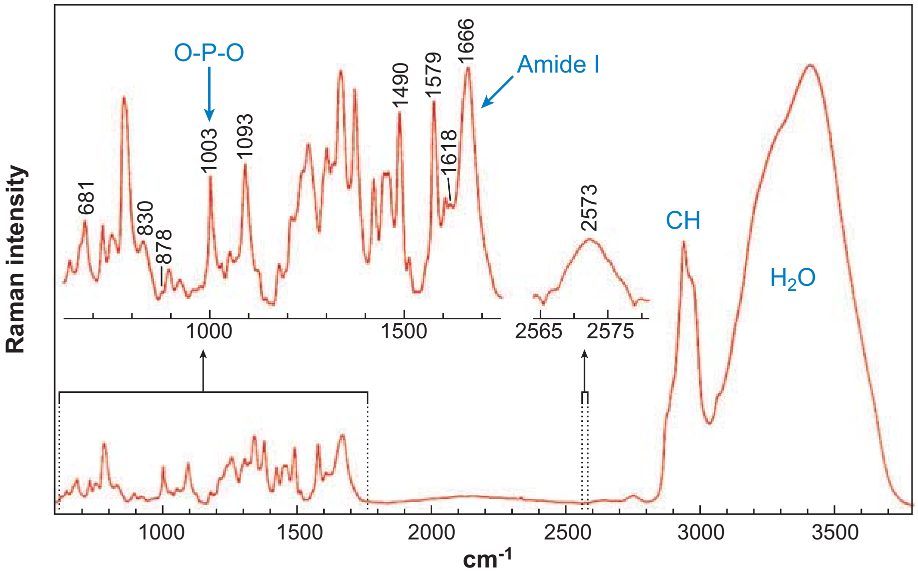

Figure 1.3: Raman spectrum of P22 virus with characteristic vibrational frequencies labeled. Shown in the inset is the fingerprint region ($\sim$ 600 cm^{-1} - 1700 cm^{-1}) where a high density of vibrational modes can be used to obtain high chemical specificity. [15]

labeled in the figure. The spectral peaks represent discrete modes of molecular vibration in the sample and can thus be used to determine the chemical composition of the sample. The inset of Figure 1.3 shows the "fingerprint" region from $\sim$ 600 cm^{-1} - 1700 cm^{-1}, which contains a high density of Raman peaks, providing a Raman "fingerprint" for chemical identification.

Over the past few years, the field of Raman microscopy has grown rapidly. Its promise of endogenous chemical contrast has been particularly exciting, allowing the differentiation of chemical species in an image without the need for potentially toxic fluorescent labeling. However, it is an extremely weak process that suffers from extremely low signal levels due to the small cross section for Raman scattering (Raman conversion efficiencies are typically less than 1 in 10^{18} [15], more than ten orders of magnitude smaller than fluorescence). Significantly higher signals can often be obtained by coherently exciting the Raman transition, which can be done in a variety of excitation configurations. Coherent Raman microscopy has been an extremely

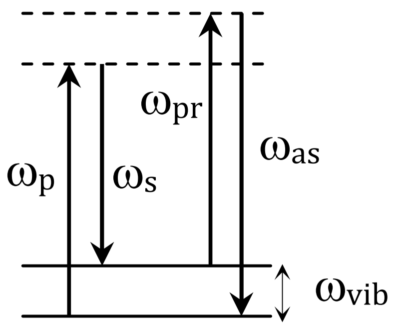

Figure 1.4: Energy level diagram of coherent anti-Stokes Raman scattering (CARS). The pump (ω_p) and Stokes (ω_S) beams excite a coherence at a vibrational energy level (ω_{vib}), and the probe field (ω_{pr}) inelastically scatters off the coherence, yielding a photon at the anti-Stokes frequency (ω_{as}).

active field over the past fifteen years due to its potential for high signal levels, which in turn give rise to fast imaging speeds [16, 17]. A number of different coherent Raman imaging modalities have been explored in an effort to improve signal-to-noise levels and maintain the Raman spectral information that makes the technique so useful [18–27].

The most popular method of coherent Raman microscopy is coherent anti-Stokes Raman scattering (CARS) microscopy [16–18, 20, 21, 28]. First discovered by Maker and Terhune [29], coherent anti-Stokes Raman scattering is a four-wave mixing (FWM) process that probes the third order nonlinearity of a sample. Shown in Figure 1.4, this is achieved by exciting a vibrational coherence at ω_{vib} using two beams, a pump beam at ω_p and a Stokes beam at ω_S. If the frequency difference between the two beams ($\omega_p - \omega_S$) matches a characteristic molecular vibrational frequency of the sample, the pump and Stokes fields will modulate the polarizability of the sample. The third pulse at ω_{pr} probes the vibrational coherence generated by the first two pulses and generates light at the anti-Stokes frequency ω_{as}, which is spectrally separated from all excitation frequencies. Coherent Stokes Raman scattering (CSRS) is the identical process with the emission on the Stokes (red) side of the excitation wavelengths. The coherent excitation of molecules in the focal region allows the CARS signal to add coherently along the excitation volume, in contrast with the incoherent addition of signal in the case of spontaneous Raman. Under the right conditions, this can lead to large increases in signal with CARS relative to spontaneous Raman [17, 18]. The experimental conditions under which this occurs are explored in chapter III of this dissertation.

1.2 Third-order Nonlinear Susceptibility

According to Maxwell's equations, the polarization response of a medium is related to the excitation field by the electric susceptibility $\vec{\chi}$ by the following relationship [30]:

$$\mathbf{P} = \vec{\chi} \cdot \mathbf{E} \tag{1.1}$$

which can be expanded in a power series as:

$$P_\alpha = \chi_{\alpha\beta} E_\beta + \chi^{(2)}_{\alpha\beta\gamma} E_\beta E_\gamma + \chi^{(3)}_{\alpha\beta\gamma\delta} E_\beta E_\gamma E_\delta + ... \tag{1.2}$$

where the subscripts denote Cartesian coordinates. As a four-wave mixing process, CARS relies on the third-order term in the expansion $\chi^{(3)}$. $\chi^{(3)}$ is a fourth-rank tensor with up to 81 components. In an isotropic medium, however, most of these terms vanish [30], leaving the four remaining elements

$$\chi^{(3)}_{1111}, \chi^{(3)}_{1122}, \chi^{(3)}_{1212}, \chi^{(3)}_{1221}.$$

that fulfill the relationship

$$\chi^{(3)}_{1111} = \chi^{(3)}_{1122} + \chi^{(3)}_{1212} + \chi^{(3)}_{1221} \tag{1.3}$$

Different coherent Raman spectroscopy modalities will probe different components

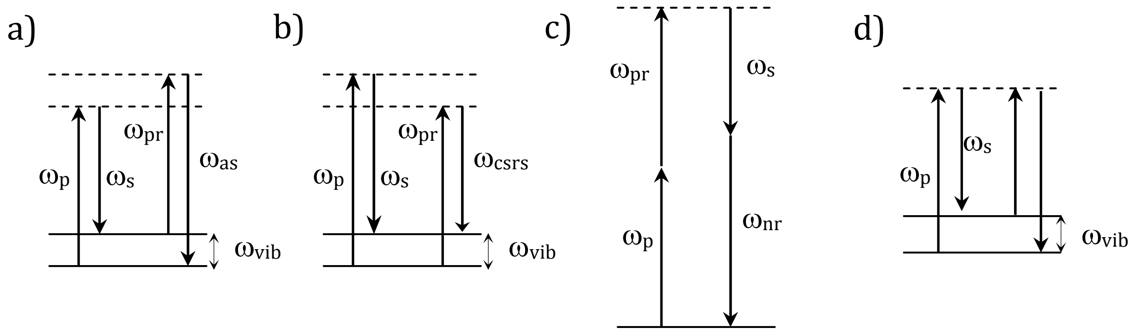

Figure 1.5: Energy level diagram of a) coherent anti-Stokes Raman scattering (CARS), b) coherent Stokes Raman scattering (CSRS), c) the nonresonant background (NR), and d) stimulated Raman scattering/Raman-induced Kerr effect (RIKES). Anti-Stokes radiation ω_{as} and nonresonant background ω_{nr} have the same energy and are indistinguishable spectrally. A similar nonresonant background exists for CSRS.

of the nonlinear susceptibility. Several imaging applications of these modalities are explored in this dissertation, including coherent Stokes Raman scattering (CSRS) in chapter III, Stimulated Raman scattering (SRS) in chapter IV, and Raman-induced Kerr effect spectroscopy (RIKES) in chapter IV.

1.3 Nonresonant Signal Suppression

With Coherent anti-Stokes Raman scattering (CARS) and coherent Stokes Raman scattering (CSRS), the primary source of background is a nonresonant background [16, 19]. The nonresonant background is a purely electronic response that is independent of molecular vibrational modes. For chemical imaging, the non-chemically specific aspect of the nonresonant background reduces contrast and makes chemical identification difficult. The nonresonant background can also introduce distortions into the Raman lineshape. Figure 1.5 shows an energy level diagram of CARS, CSRS, and the nonresonant background. Also shown is the energy level diagram for SRS and RIKES for comparison.

Several methods of nonresonant background suppression have been applied with varying degrees of success. One method of discriminating between the resonant and nonresonant contributions to the signal is using the different polarizations of the two contributions. Because the polarization of the nonresonant background is generally different than the polarization of the resonant signal, one can use an analyzing polarizer to suppress the nonresonant background [31]. This has successfully been applied to spectroscopy applications in solution [32] as well as microscopy applications [19]. The downside to this technique is that it is more difficult to set up experimentally than CARS, and the degree of nonresonant signal suppression suffers from any birefringence in the sample.

Another method of nonresonant signal suppression takes advantage of the different timescales of nonresonant and resonant signals. Because the nonresonant signal is electronic in nature, it is very short lived – on the order of femtoseconds. The coherence generated by the pump and Stokes pulses in CARS, however, can last picoseconds, making discrimination between the two contributions possible in the time domain. By delaying the probe pulse with respect to the pump pulses, the electronic nonresonant signal is suppressed with only a small loss in resonant signal. This is commonly referred to as pulse-sequenced coherent anti-Stokes Raman scattering (PUSCARS) [33] or time-delay coherent anti-Stokes Raman scattering (TDCARS) [20, 34]. This method is used in chapter III of this work. Stimulated Raman scattering (SRS) and Raman-induced Kerr effect spectroscopy (RIKES), under the right conditions, do not exhibit this nonresonant background.

1.4 Thesis Outline and Chapter Overview

This thesis is comprised of three distinct but related experiments. The aim of all three experiments is the analysis and/or development of methods for increasing sensitivity in Raman scattering for imaging and sensing applications. Raman techniques covered are spontaneous Raman scattering, coherent anti-Stokes Raman scattering (CARS), stimulated Raman scattering (SRS), Raman-induced Kerr effect spectroscopy (RIKES), surface-enhanced Raman scattering (SERS), and surface-enhanced coherent anti-Stokes Raman scattering (SECARS).

Chapter II provides the theoretical background for all of the Raman processes covered in this thesis. Starting with a formulation of spontaneous Raman scattering, the theory proceeds with an analysis of all coherent techniques covered. The derivation of the differential and total Raman scattering cross sections are shown, followed by the derivation of total CARS signal, including contributions from resonant and nonresonant susceptibilities. The intensity of signals from RIKES, SERS, and SECARS are derived.

Chapter III presents a systematic comparison of spontaneous and coherent Raman scattering signal levels under conditions relevant for biological imaging. For low-concentration samples and low-excitation power imaging, the advantages conferred by coherent Raman excitation are reduced. Due to the relative dependencies of coherent and spontaneous Raman on concentration and power, there exists a critical power at which the two schemes will give equal signal levels. We explore the experimental conditions under which this is the case and show that, in many biological imaging applications, spontaneous Raman will in fact provide higher signal intensity than coherent Raman techniques.

In **Chapter IV**, we demonstrate the first multiplexed RIKES microscopy experiment. Using a photonic crystal fiber to generate a continuum probe, we demonstrate the ability to get high-resolution Raman spectra over a broad bandwidth. By using the high signal-to-noise ratio offered by RIKES, we have performed spectrally-resolved vibrational imaging of polystyrene beads with high sensitivity. We compare the results with femtosecond stimulated Raman scattering (FSRS) microscopy using a chopping scheme to provide modulation. Comparison of signal levels is also performed in solution.

Chapter V explores surface-enhanced effects with Raman scattering. We perform surface-enhanced Raman spectroscopy on commercial SERS substrates, showing large enhancement for benzenethiol molecules adsorbed onto nanostructured gold films. We apply a similar coherent Stokes Raman scattering (CSRS) setup as in **Chapter III** to investigate surface-enhanced coherent Raman signals. We observe a large unidentified broadband four-wave mixing signal that makes the detection of surface-enhanced coherent Raman signals difficult. This work identifies obstacles that must be overcome to combine surface enhancement and coherent Raman methods for high sensitivity imaging and sensing applications.

Chapter VI summarizes the findings in this thesis. Using several different coherent Raman techniques, we are able to analyze and/or increase the sensitivity for chemical imaging. Future directions include analyzing the relative signal strengths of CARS and spontaneous Raman for picosecond pulses, implementing multiplexed Raman-induced Kerr effect microscopy with biological tissue samples, and investigating methods of suppressing the four-wave mixing background for surface-enhanced CARS.

References

[1] E. Keller and R. D. Goldman. *Basic Methods in Microscopy*, chapter Light Microscopy, pages 1–42. Cold Spring Harbor Laboratory Press, 2006.

[2] Coons and Kaplan. Localization of antigen in tissue cells; improvements in a method for the detection of antigen by means of fluorescent antibody. *J Exp Med.*, 91:1–13, 1950.

[3] Keith Berland. *Methods in Cellular Imaging.* Oxford University Press, 2001.

[4] R. Heim, A. B. Cubitt, and R. Y. Tsien. Improved Green Fluorescence. *Nature*, 373:663–664, 1995.

[5] M. Ormo, A. B. Cubitt, K. Kallio, L. A. Gross, R. Y. Tsien, and S. J. Remington. Crystal structure of the Aequorea victoria green fluorescent protein. *Science*, 273:1392–1395, 1996.

[6] A. Miyawaki, J. Llopis, R. Heim, J. M. McCaffery, J. A. Adams, M. Ikura, and R. Y. Tsien. Fluorescent indicators for Ca2+ based on green fluorescent proteins and calmodulin. *Nature*, 388:882–887, 1997.

[7] R. Y. Tsien. The green fluorescent protein. *Annual Review of Biochemistry*, 67:509–544, 1998.

[8] J. Stricker, P. Maddox, E. D. Salmon, and H. P. Erickson. Rapid assembly dynamics of the Escherichia coli FtsZ-ring demonstrated by fluorescence recovery after photobleaching. *Proceedings of the National Academy of Sciences of the United States of America*, 99:3171–3175, 2002.

[9] N. B. Cole, C. L. Smith, N. Sciaky, M. Terasaki, M. Edidin, and J. Lippincott-Schwartz. Diffusional mobility of Golgi proteins in membranes of living cells. *Science*, 273:797–801, 1996.

[10] P. J. Campagnola and L. M. Loew. Second-harmonic imaging microscopy for visualizing biomolecular arrays in cells, tissues, and organisms. *Nature Biotechnology*, 21:1356–1360, 2003.

[11] Y. Barad, H. Eisenberg, M. Horowitz, and Y. Silberberg. Nonlinear scanning laser microscopy by third harmonic generation. *Applied Physics Letters*, 70:922–924, 1997.

[12] D. Debarre, W. Supatto, A. M. Pena, A. Fabre, T. Tordjmann, L. Combettes, M. C. Schanne-Klein, and E. Beaurepaire. Imaging lipid bodies in cells and tissues using third-harmonic generation microscopy. *Nature Methods*, 3:47–53, 2006.

[13] M. C. Fischer, H. C. Liu, I. R. Piletic, Y. Escobedo-Lozoya, R. Yasuda, and W. S. Warren. Self-phase modulation signatures of neuronal activity. *Optics Letters*, 33:219–221, 2008.

[14] C. V. Raman. The Raman Effect: Investigations on Molecular Structure by Light Scattering. *Transactions of the Faraday Society*, 25:781–792, 1929.

[15] C. L. Evans and Xie. X. S. Coherent Anti-Stokes Raman Scattering MIcroscopy: Chemical Imaging for Biology and Medicine. *Annual Review of Analytycal Chemistry*, 1:883–909, 2008.

[16] J. X. Cheng, A. Volkmer, and X. S. Xie. Theoretical and experimental characterization of coherent anti-Stokes Raman scattering microscopy. *Journal of the Optical Society of America B-Optical Physics*, 19(6):1363–1375, Jun 2002.

[17] J. X. Cheng and X. S. Xie. Coherent anti-Stokes Raman scattering microscopy: Instrumentation, theory, and applications. *Journal of Physical Chemistry B*, 108:827–840, 2004.

[18] A. Zumbusch, G. R. Holtom, and X. S. Xie. Three-dimensional vibrational imaging by coherent anti-Stokes Raman scattering. *Physical Review Letters*, 82(20):4142–4145, May 17 1999.

[19] J. X. Cheng, L. D. Book, and X. S. Xie. Polarization coherent anti-Stokes Raman scattering microscopy. *Optics Letters*, 26(17):1341–1343, Sep 1 2001.

[20] A. Volkmer, L. Book, and X. S. Xie. Time-resolved coherent anti-Stokes Raman scattering microscopy: Imaging based on Raman free induction decay. *Applied Physics Letters*, 80:1505, 2002.

[21] J. P. Ogilvie, E. Beaurepaire, A. Aleandrou, and M. Joffre. Fourier-transform coherent anti-Stokes Raman scattering microscopy. *Optics Letters*, 31:480–482, 2006.

[22] E. Ploetz, S. Laimgruber, S. Berner, W. Zinth, and P. Gilch. Femtosecond stimulated Raman microscopy. *Applied Physics B-Lasers and Optics*, 87(3):389–393, May 2007.

[23] M. Cui, J. Skodack, and J. P. Ogilvie. Chemical imaging with Fourier transform coherent anti-Stokes Raman scattering microscopy. *Applied Optics*, 47(31):5790–5798, Oct 08-10 2008.

[24] C. W. Freudiger, W. Min, B. G. Saar, S. Lu, G. R. Holtom, C. W. He, J. C. Tsai, J. X. Kang, and X. S. Xie. Label-Free Biomedical Imaging with High Sensitivity by Stimulated Raman Scattering Microscopy. *Science*, 322(5909):1857–1861, Dec 2008.

[25] B. G. Saar, C. W. Freudiger, J. Reichman, C. M. Stanley, G. R. Holtom, and X. S. Xie. Video-Rate Molecular Imaging in Vivo with Stimulated Raman Scattering. *Science*, 330(6009):1368–1370, Dec 2010.

[26] C. W. Freudiger, M. B. J. Roeffaers, X. Zhang, B. G. Saar, W. Min, and X. S. Xie. Optical heterodyne-detected Raman-induced Kerr effect (OHD-RIKE) microscopy. *The Journal of Physical Chemistry B*, 5(ASAP):103–109, 2011.

[27] D. Zhang, M. N. Sipchenko, and J. X. Cheng. Highly Sensitive Vibrational Imaging by Femtosecond Pulse Stimulated Raman Loss. *Journal of Physical Chemistry Letters*, 2(11):1248–1253, Jun 2011.

[28] M. D. Duncan, J. Reintjes, and T. J. Manuccia. Scanning coherent anti-Stokes Raman microscope. *Opt. Lett.*, 7(8):350–352, 1982.

[29] P. D. Maker and R. W. Terhune. Study of optical effects due to an induced polarization third order in electric field strength. *Physical Review*, 137:801–819, 1965.

[30] M. D. Levenson and S. S. Kano. *Introduction to Nonlinear Laser Spectroscopy.* Academic Press, Inc., 1988.

[31] S. A. Akhmanov, A. F. Bunkin, S. G. Ivanov, and N. I. Koroteev. Coherent ellipsometry of Raman-scattering of light. *JETP Letters*, 25:416–420, 1977.

[32] J. L. Oudar, R. W. Smith, and Y. R. Shen. Polarization-sensitive coherent anti-Stokes Raman spectroscopy. *Applied Physics Letters*, 34:758–760, 1979.

[33] F. M. Kamga and M. G. Skeats. Pulse-sequenced coherent anti-Stokes Raman scattering spectroscopy: a method for suppression of the nonresonant background. *Optics Letters*, 5:126, 1980.

[34] M. Cui, B. Bachler, and J. P. Ogilvie. Comparing coherent and spontaneous Raman scattering under biological imaging conditions. *Optics Letters*, 34:773–775, 2009.

CHAPTER II

Theory

2.1 Spontaneous Raman scattering

Spontaneous Raman scattering is an inelastic process that produces redshifted light at a frequency shift determined by vibrational resonances in a molecule. An energy level diagram of spontaneous Raman scattering is shown in Figure 2.1. The excitation light is labeled ω_p and the Raman signal is labeled ω_S, shifted in frequency from the excitation light by a frequency equal to that of a Raman active vibrational mode of the molecule ω_{vib}. The process can be described by semiclassical theory [1, 2]. In this description, we will follow the theory review described by Wang [2]. Using the dipole approximation, the Hamiltonian describing the interaction between an electric

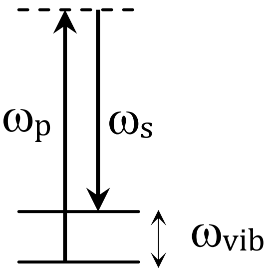

Figure 2.1: Spontaneous Raman energy level diagram. Pump (ω_p) and signal (ω_S) fields are shown.

field and a molecule can be written as:

$$H = H_0 - \mathbf{M} \cdot \mathbf{E} \tag{2.1}$$

where H_0 is the Hamiltonian of the molecule with no applied field, $\mathbf{M}$ is the electric dipole moment of the molecule, and $\mathbf{E}$ is the applied electric field:

$$\mathbf{E} = \mathbf{E}_{-} e^{-i\omega t} + \mathbf{E}_{+} e^{i\omega t} \tag{2.2}$$

where, because $\mathbf{E}$ is real, $\mathbf{E}_{-} = (\mathbf{E}_{+})^{*}$. If the quantity $\mathbf{M} \cdot \mathbf{E}$ is significantly smaller than H_0, perturbation theory can be used to find the solution to the Schrödinger equation:

$$\{H_0 - \mathbf{M} \cdot \mathbf{E}_{-} e^{-i\omega t} - \mathbf{M} \cdot \mathbf{E}_{+} e^{i\omega t}\}\Psi = i\hbar \frac{\partial \Psi}{\partial t} \tag{2.3}$$

For a trial solution

$$\Psi = \psi_{0l} e^{\frac{iE_{0l}t}{\hbar}} + \left[\psi_{l-} e^{-i\omega t} + \psi_{l+} e^{i\omega t}\right] e^{\frac{-iE_{0l}t}{\hbar}} \tag{2.4}$$

with an eigenfunction $\psi_{0l} e^{-E_{0l}t/\hbar}$ of H_0, with ψ_{l-} and ψ_{l+} first order in the perturbation, we get:

$$\left[H_0 - \epsilon_{0l} \pm \hbar\omega\right] \psi_{l\pm} = \sum_{\alpha} M_{\alpha} E_{\alpha\pm} \psi_{0l} \tag{2.5}$$

where α denotes the components of $\mathbf{E}$ and $\mathbf{M}$, and $\psi_{l\pm}$ expanded as:

$$\psi_{l\pm} = \frac{1}{\hbar} \sum_{r} \sum_{\alpha} \frac{\langle s|M_{\alpha}|l\rangle}{\omega_{rl} + \omega} E_{\alpha\pm} \psi_{0l} \tag{2.6}$$

Substituting back into equation 2.4, we get a perturbed wavefunction of the following form [2]:

$$\Psi_l = e^{-iE_{0l}t/\hbar}\left\{\psi_{0l} + \frac{1}{\hbar}\sum_\beta\sum_r\left[\frac{\langle r\,|M_\beta|\,l\rangle}{\omega_{rl}-\omega}\psi_{0r}E_{\beta-}e^{-i\omega t} + \frac{\langle r\,|M_\beta|\,l\rangle}{\omega_{rl}+\omega}\psi_{0r}E_{\beta+}e^{i\omega t}\right]\right\} \tag{2.7}$$

with β representing the vector components of **E** and **M** and l representing the quantum number associated with the state. The expectation value, then, of the electric dipole moment $m_\alpha(t)$ for the transition between l and m states is:

$$m_\alpha(t) = \sum_\beta\left\{\left[\alpha^{lm}_{\alpha\beta}(\omega)\right]^* E_{\beta-}e^{i(\omega+\omega_{lm})t} + \alpha^{lm}_{\alpha\beta}(\omega)E_{\beta+}e^{i(\omega+\omega_{lm})t}\right\} \tag{2.8}$$

where the transition polarizability $\alpha^{lm}_{\alpha\beta}(\omega)$ is given by:

$$\alpha^{lm}_{\alpha\beta}(\omega) = \frac{1}{\hbar}\sum_r\left\{\frac{\langle l|M_\alpha|r\rangle\langle r|M_\beta|m\rangle}{\omega_{rm}+\omega} + \frac{\langle l|M_\beta|r\rangle\langle r|M_\alpha|m\rangle}{\omega_{rl}-\omega}\right\} \tag{2.9}$$

Following Placzek's use of the Born-Oppenheimer approximation and the normal mode expansion, the results can be simplified [3]. The nuclear and electronic motion of the system can be separated in the adiabatic approximation, allowing the eigenfunction of H_0 to be written [2]:

$$\Psi_{n\nu}(x,X) = \chi_{n\nu}(X)\varphi_n(x,X) \tag{2.10}$$

where $\varphi_n(x,X)$ is the wave function of the electrons moving in the field of the nuclei. n corresponds to the quantum number associated with the wavefunction of electronic motion in the fixed state of the nuclei. Although the motions of molecules include translational, rotational, vibrational, and electronic motions, translational and rotational motion can be neglected in the static approximation – they are much slower than vibrational and electronic motion.

The nuclear component of the motion is denoted by $\chi_{n\nu}(X)$ (with ν representing the vibrational quantum number for nuclear motion), moving in an effective potential $E_n(X) - E_n(X_0)$. The eigenvalue of H_0 can then be written [2]:

$$E_n(X_0) + \epsilon_{n\nu} \tag{2.11}$$

where $\epsilon_{n\nu} \ll E_{n'}(X) - E_n(X)$. The transition polarizability associated with a vibrational transition may be written as:

$$\alpha_{\alpha\beta}^{vv'}(\omega) = \frac{1}{\hbar}\sum_{n''}\sum_{v''}\left\{\frac{\langle 0v|M_\alpha|n''v''\rangle\langle n''v''|M_\beta|0v'\rangle}{\omega_{n''v'',0v}+\omega} + \frac{\langle 0v|M_\beta|n''v''\rangle\langle n''v''|M_\alpha|0v'\rangle}{\omega_{n''v'',0v}-\omega}\right\} \tag{2.12}$$

The summation over n'' may be split according to the two cases $n'' = 0$ and $n'' \neq 0$. Also using the approximation $\omega_{n''v'',0v} = \omega_{n'',0}$, the transition polarizability may be written:

$$\begin{aligned}\alpha_{\alpha\beta}^{vv'} =& \frac{1}{\hbar}\sum_{v''}\left\{\frac{\langle v|M_\alpha(X)|v''\rangle\langle v''|M_\beta(X)|v'\rangle}{\omega_{v''v'}+\omega} + \frac{\langle v|M_\beta(X)|v''\rangle\langle v''|M_\alpha(X)|v'\rangle}{\omega_{v''v}-\omega}\right\} \\ &+ \frac{1}{\hbar}\sum_{n''}\left\{\frac{\langle 0v|M_\alpha|n''v''\rangle\langle n''v''|M_\beta|0v'\rangle}{\omega_{n''0}+\omega} + \sum_{v''}\frac{\langle 0v|M_\beta|n''v''\rangle\langle n''v''|M_\alpha|0v'\rangle}{\omega_{n''0}-\omega}\right\}\end{aligned} \tag{2.13}$$

where

$$M(X) = \int \varphi_0^*(x,X)M(x,X)\varphi_0(x,X)dx \tag{2.14}$$

The first term in Equation 2.13 is called the ionic part of the polarizability, depending only on the nuclear motion with electrons in the lowest level. Because the nuclear wave equations satisfy the relationship $\sum_v \chi_{nv}(X')\chi_{nv}^*(X) = \delta(X - X')$, the second term of Equation 2.13 may be written as:

$$\langle v|\alpha_{\alpha\beta}(\omega X)|v'\rangle \tag{2.15}$$

with the electronic polarizability:

$$\alpha_{\alpha\beta}(\omega X) = \frac{1}{\hbar}\sum_{n''\neq 0}\left\{\frac{\langle 0|M_\alpha|n''\rangle\langle n''|M_\beta|0\rangle}{\omega_{n''0}+\omega} + \frac{\langle 0|M_\beta|n''\rangle\langle n''|M_\alpha|0\rangle}{\omega_{n''0}-\omega}\right\} \tag{2.16}$$

In the optical region, $\omega \approx \omega_{n''0} \gg \omega_{v''v}$, making the first term in Equation 2.13 much smaller than the second (electronic) term. If the polarizability is expanded in a Taylor series with respect to the normal-mode coordinate $q = \frac{X}{\sqrt{(\mu)}}$ (for reduced mass μ) of the molecular vibration, we can write [2]:

$$\alpha(\omega, X) = \alpha(\omega, X_0) + \sum_i \left(\frac{\partial\alpha}{\partial q_i}\right)_0 q_i + \frac{1}{2}\sum_{ij}\left(\frac{\partial^2\alpha}{\partial q_i \partial q_j}\right) q_i q_j + \dots \tag{2.17}$$

The first order term in Equation 2.17 represents contributions to the first Stokes or anti-Stokes Raman scattering. The higher-order terms represent contributions from multiphoton processes. The matrix element for the first order term can be written as:

$$\begin{aligned}\langle v|\alpha(\omega, X)|v'\rangle &= \sum_i \langle v|\left(\frac{\partial\alpha}{\partial q_i}\right)_0 q_i|v'\rangle \\ &= \sum_i \left(\frac{\partial\alpha}{\partial q_i}\right)_0 \langle v|q_i|v'\rangle\end{aligned} \tag{2.18}$$

where it can be seen that only the normal mode coordinate q is involved in the dynamics. The coupling constant between the optical field and the vibrational modes of the molecule is given by the term $(\partial\alpha/\partial q)_0$.

We can use this formulation to calculate the cross-section for the Raman interaction. Equation 2.10 shows that the incident field will induce an oscillating electric dipole moment [2]:

$$m_\alpha(t) = m_{\alpha-}e^{-i\omega_s t} + m_{\alpha+}e^{i\omega_s t} \tag{2.19}$$

where $\omega_s = \omega - \omega_v$, $\omega_v = -\omega_{lm} = (1/\hbar)(\epsilon_{01} - \epsilon_{00})$, and $m_{\alpha-} = \sum_\beta \left[\alpha_{\alpha\beta}^{vv'}\right]^* E_{\beta-}$,

$m_{\alpha+} = \sum_\beta \alpha_{\alpha\beta}^{vv'}(\omega) E_{\beta+}$. This gives rise to a classical radiation field per unit solid angle of:

$$\frac{dP}{d\Omega} = \frac{1}{4\pi c^3} \left(\frac{\partial^2 m}{\partial t^2} \right)^2 (t) \sin^2 \varphi = \frac{\omega_S^4}{2\pi c^3} \sum_\alpha m_{\alpha+} m_{\alpha-} \sin^2 \varphi \tag{2.20}$$

where φ is the angle between the dipole moment vector and the direction of dipole radiation emission. For a linearly polarized excitation field, $\langle 1|q|0 \rangle = (\hbar/2\omega_v)^{1/2}$, and using Equation 2.18, the power radiated per unit solid angle can be written:

$$\frac{dP}{d\Omega} = \frac{\omega_S^4}{2\pi c^3} \left(\frac{\partial \alpha}{\partial q} \right)_0^2 \frac{\hbar}{2\omega_v} |E_L|^2 \cos^2 \theta \tag{2.21}$$

where θ is the angle between the incident and scattered wavevectors. Integrating over the full 4π solid angle, we get:

$$P = \frac{4\omega_S^4}{3c^3} \left(\frac{\partial \alpha}{\partial q} \right)_0^2 \frac{\hbar}{2\omega_v} |E_L|^2 \tag{2.22}$$

From Equations 2.21 and 2.22, the differential and total cross section for spontaneous Raman is:

$$\frac{d\sigma}{d\Omega} = \frac{dP}{d\Omega} \left(\frac{c|E_L|^2}{4\pi} \right)^{-1} = \frac{2\omega_S^4}{c^4} \left(\frac{\partial \alpha}{\partial q} \right)_0^2 \frac{\hbar}{2\omega_v} \cos^2 \theta \tag{2.23}$$

and

$$\sigma = \frac{16\pi\omega_S^4}{3c^4} \left(\frac{\partial \alpha}{\partial q} \right)_0^2 \frac{\hbar}{2\omega_v} \tag{2.24}$$

which is on the order ($\approx 10^{-30}$ cm^2). This cross section represents the strength of the Raman mode oscillation for a given excitation field for incoherent spontaneous Raman scattering.

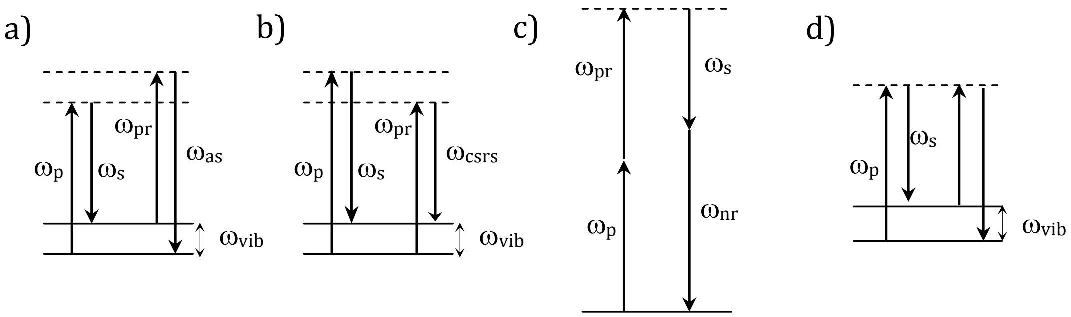

Figure 2.2: a) CARS, b) CSRS, and c) nonresonant background energy level diagrams. CARS signal and nonresonant background frequencies (ω_{as} and ω_{nr}, respectively) are equal. CSRS also has an associated nonresonant background (not shown). d) Stimulated Raman/Raman-induced Kerr effect energy level diagram shown for comparison.

2.2 Coherent anti-Stokes Raman Scattering

Figure 2.2 shows an energy level diagram for coherent anti-Stokes Raman scattering (CARS) and coherent Stokes Raman scattering (CSRS). First observed by Maker and Terhune in 1965 [4], CARS is a four-wave mixing process by which two excitation beams E_p of frequency ω_p (pump) and E_S of frequency ω_S (Stokes) excite a vibrational coherence in a molecule when the frequency difference is equal to the vibrational mode frequency ($\omega_p - \omega_S = \omega_{vib}$), while a third probe beam ω_{pr} mixes with the coherence to produce output light at the anti-Stokes frequency ω_{as}. In an isotropic medium, the theory of CARS can be described classically as in Shen [5]:

$$\left[\nabla^2 + \frac{\omega_{as}^2}{c^2}\varepsilon_{as}(\omega_{as})\right]\mathbf{E}_{as} = -\frac{4\pi\omega_{as}^2}{c^2}\mathbf{P^{(3)}}(\omega_{as}) \tag{2.25}$$

where $\mathbf{P^{(3)}}(\omega_{as}) = \chi^{(3)}(\omega_{as} = \omega_p - \omega_S + \omega_{pr}) : \mathbf{E}_p(\omega_p)\mathbf{E}_S^*(\omega_S)\mathbf{E}_{pr}(\omega_{pr})$ and ε_{as} is the permittivity of the medium at the anti-Stokes frequency. The solution to the wave equation 2.25 gives the CARS output intensity I_{as} from a Raman medium of length l:

$$I_{as} = \frac{c}{2\pi}\left|E_{as}\right|^2 = \frac{2\pi\omega_{as}^2}{c\varepsilon_{as}}\left|\chi_{as}^{(3)}\right|^2\left|E_p\right|^2\left|E_S\right|^2\left|E_{pr}\right|^2\frac{\sin^2(\frac{1}{2}\Delta k_l l)}{(\frac{1}{2}\Delta k_l l)^2} \tag{2.26}$$

where

$$\chi_{as}^{(3)} = \hat{e}_{as} \cdot \chi^{(\mathbf{3})} : \hat{e}_p \hat{e}_S \hat{e}_{pr}$$
$$\Delta k_l = \Delta \mathbf{k} \cdot \hat{l}$$
$$\Delta \mathbf{k} = \mathbf{k}_{as} - (\mathbf{k}_p - \mathbf{k}_S + \mathbf{k}_{pr}) \tag{2.27}$$

$\chi_{as}^{(3)}$ can be separated into a resonant part $\chi_R^{(3)}$ and a nonresonant part $\chi_{NR}^{(3)}$. The resonant part $\chi_R^{(3)}$ will have frequency peaks at Raman vibrational modes of the molecule, while the nonresonant part $\chi_{NR}^{(3)}$ gives rise to a non-chemically specific nonresonant background due to processes such as those illustrated in Figure 2.2, which is generally undesirable in CARS applications. If we separate the resonant term into its real and imaginary parts, $\chi^{(3)}$ can be written [6]:

$$\chi = \chi^{NR} + \chi' + i\chi'' \tag{2.28}$$

where χ' is the real part of the resonant susceptibility and χ'' is the imaginary part of the resonant susceptibility. The tensor component 1111 and the superscript (3) denoting third-order nonlinear susceptibility are dropped for convenience. For all further equations in this section, both are implied. The resulting field may be written as [6]:

$$E(\omega_{as}) = \frac{3}{8} i\omega_{as} \sqrt{\frac{\mu_0}{\varepsilon_0 \varepsilon_{as}}} \left[\chi^{NR} + \chi' + i\chi''\right] E(\omega_p) E(\omega_S) E(\omega_{pr}) l \frac{\sin \frac{1}{2}\Delta k l}{\frac{1}{2}\Delta k l} \tag{2.29}$$

where μ_0 and ε_0 are the permeability and permittivity of free space, respectively.

The detected intensity from this field is:

$$I(\omega_{as}) = \frac{c}{2} n_{as} \varepsilon_0 \left|E(\omega_{as})\right|^2 \tag{2.30}$$

which can thus be written [6]:

$$I(\omega_{as}) = \frac{9}{16}\frac{\omega_{as}^2}{n_p^2 n_S n_{pr}}\left(\frac{\mu_0}{\varepsilon_0}\right)^2 I(\omega_p)I(\omega_S)I(\omega_{pr})l^2\frac{\sin^2(\frac{1}{2}\Delta k_l l)}{(\frac{1}{2}\Delta k_l l)^2}$$
$$\times\left[\left|\chi^{NR}\right|^2 + \left|\chi'\right|^2 + \left|\chi''\right|^2 + 2\chi^{NR}\chi'^*\right] \tag{2.31}$$

where n is the index of refraction at the wavelength indicated by the subscript.

As can be seen from Equation 2.31, there are four primary contributions to the CARS signal: 1) a nonresonant background contribution from χ^{NR}, 2) a dispersive resonant term from χ', 3) a Lorentzian lineshape resonant component from χ'', and 4) a cross term $2\chi^{NR}\chi'$. Thus, CARS generally has a complex lineshape that takes contributions from all of the $\chi^{(3)}$ components.

As seen in Equation 2.31, the intensity also depends on a phase matching term given by the sinc function:

$$\frac{\sin^2(\frac{1}{2}\Delta k_l l)}{(\frac{1}{2}\Delta k_l l)^2} \tag{2.32}$$

which in a collinear geometry implies a coherent interaction length of

$$L_c = \frac{\pi}{\Delta k} \tag{2.33}$$

that will provide a maximum signal, with Δk given by:

$$\Delta k = \frac{[n_p\omega_p + n_{pr}\omega_{pr} - n_S\omega_S - n_{as}(\omega_p + \omega_{pr} - \omega_S)]}{c} \tag{2.34}$$

for all four fields involved in the interaction.

For perfect phase-matching, this quantity Δk must be equal to zero. However, when tight-focusing is used for excitation (as in our case, with an objective lens), the phase-matching condition is relaxed. With a high numerical aperture with objective lenses, there is a large cone of wave vectors and short interaction length, automatically

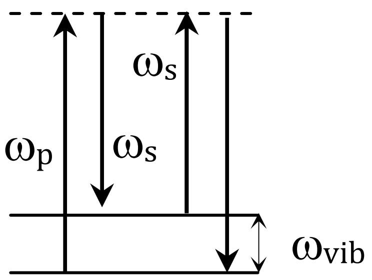

Figure 2.3: Stimulated Raman scattering energy level diagram. Pump (ω_p) and probe (ω_S) fields are shown.

fulfilling the phase-matching condition without needing to adjust the angle of the excitation beams [7].

2.3 Stimulated Raman Spectroscopy

First observed in 1962 [8], stimulated Raman spectroscopy is a process in which two beams can combine to coherently excite molecular vibrational modes of a sample. Figure 2.3 shows the energy level diagram for stimulated Raman scattering. If the frequency difference between a pump (ω_p) and Stokes (ω_S) beam matches that of a Raman vibrational resonance ($|\omega_p - \omega_S| = \omega_{vib}$), a Raman loss or gain will occur in the pump or Stokes beam, respectively. For analysis of the signal strength of stimulated Raman scattering and Raman-induced Kerr effect spectroscopy, we follow the derivation by Eesley [6, 9].

For pump and Stokes beams parallel to each other, we can write the excitation fields as [6]:

$$\begin{aligned} \vec{E}(\omega_S) &= E_x(\omega_S)\hat{x} \\ \vec{E}(\omega_p) &= E_x(\omega_p)\hat{x} \end{aligned} \tag{2.35}$$

with corresponding nonlinear polarization density

$$P_x(\omega_S) = \frac{6}{8}\chi_{1111}(-\omega_S, \omega_S, -\omega_p, \omega_p)E_x(\omega_S)\left|E_x(\omega_p)\right|^2 \tag{2.36}$$

where the superscript (3) in $\chi^{(3)}_{1111}$ has again been dropped for convenience.

To calculate the signal field generated by this nonlinear polarization, we can write

$$\frac{\partial}{\partial z}E_x(\omega_S) = \frac{3}{4}i\omega_S\sqrt{\frac{\mu_0}{\varepsilon_0\varepsilon_S}}\chi_{1111}(-\omega_S, \omega_S, -\omega_p, \omega_p)E_x(\omega_S)\left|E_x(\omega_p)\right|^2 \tag{2.37}$$

where μ_0 is the vacuum permeability of free space, ε_0 is the vacuum permittivity of free space, and ε_S is the permittivity of the medium at the Stokes wavelength.

Inserting the z dependence of $E_x(\omega_S, z)$, the equation can be solved to give

$$E_x(\omega_S, L) = \exp\left[\frac{3iL\omega_S}{4n_S}\sqrt{\frac{\mu_0}{\varepsilon_0}}\chi_{1111}(-\omega_S, \omega_S, -\omega_p, \omega_p)E_x(\omega_S)\left|E_x(\omega_p)\right|^2\right]E_x(\omega_S, 0) \tag{2.38}$$

where L is the interaction length through the sample.

From this equation, we can see that the incident pump field $E_x(\omega_S, 0)$ undergoes an exponential growth as it travels through a medium with interaction length L, as $E_x(\omega_S, L) \propto e^L E_x(\omega_S, 0)$. This coherent buildup of signal through the medium mirrors that of other stimulated emission processes. The intensity of the signal can thus be written as

$$I(\omega_S, L) = I(\omega_S, 0)\exp\left[-\frac{3\omega_S L}{n_p n_S}\left(\frac{\mu_0}{\varepsilon_0}\right)\mathrm{Im}(\chi_{1111})I(\omega_p)\right] \tag{2.39}$$

where it can be seen that only the imaginary part of $\chi^{(3)}$contributes to the signal level. Since the nonresonant signal is real, it will not contribute to the detected sensitivity, making SRS a particularly sensitive technique for mapping out Raman spectra that are very similar to the spontaneous Raman spectra.

The relationship between $\operatorname{Im}\chi_{11ii}$ and the differential Raman scattering cross section is derived by Eesley [6]:

$$\operatorname{Im}\chi_{11ii}(-\omega_S,\omega_S,-\omega_p,\omega_p)=\frac{8\pi^3}{3}\left(\frac{n_p\varepsilon_0^2c^4}{n_S h\omega_p\omega_S^3}\right)\frac{d^2\sigma_{xi}}{d\Omega d\omega_S}(e^{-\frac{h(\omega_p-\omega_S)}{kT}}-1) \tag{2.40}$$

Notice that for $\omega_S > \omega_p$, the argument of the exponential function in Eqn. 2.39 is negative, indicating Raman loss in the probe and Raman gain in the pump. For $\omega_p > \omega_S$, the exponent is positive, leading to stimulated Raman gain in the probe and stimulated Raman loss in the pump.

2.4 Raman-induced Kerr Effect scattering

First observed in 1975 by Heiman et al. [10], Raman-induced Kerr effect scattering (RIKES) is a four-wave mixing process by which polarization changes to a weak probe (Stokes) pulse can be induced by a strong pump. Figure 4.1 shows the energy level diagram for RIKES. The weak probe (Stokes beam) is polarized linearly at frequency ω_S, while the strong pump can be circularly polarized or linearly polarized at 45° with respect to the probe at frequency ω_p. The configuration of RIKES with a linear pump probes the nonlinear susceptibility tensor ($\chi^{(3)}$) element $\chi^{(3)}_{1122}+\chi^{(3)}_{1212}$, whereas the configuration of RIKES with a circular pump probes the nonlinear susceptibility tensor element $i\cdot\left(\chi^{(3)}_{1122}-\chi^{(3)}_{1212}\right)$ [11]. $\chi^{(3)}$ may be expressed in expanded form as $\chi_{ijkl}=\chi^{NR}_{ijkl}+\chi'_{ijkl}+\chi''_{ijkl}$, where $\chi'_{ijkl}=\operatorname{Re}(\chi_{ijkl})$ and $\chi''_{ijkl}=\operatorname{Im}(\chi_{ijkl})$. As a result, the nonresonant contribution to the signal for the circular case is proportional to $\chi^{NR}_{1122}-\chi^{NR}_{1212}$. Although they do not cancel perfectly, these two terms are generally similar in magnitude, offering up to two orders of magnitude reduction in nonresonant background [12, 13]. Because the equivalent nonresonant contribution in the linear pump case is proportional to $\chi^{NR}_{1122}+\chi^{NR}_{1212}$, the nonresonant terms do not cancel and a large frequency-independent nonresonant background can be seen in the signal. For

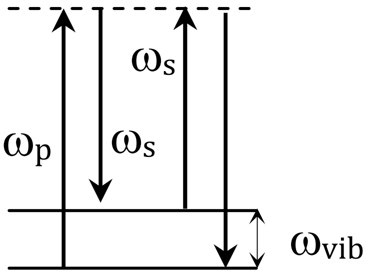

Figure 2.4: Raman-induced Kerr effect scattering (RIKES) energy level diagram. Pump (ω_p) and probe (ω_S) fields are shown.

this reason, we only perform RIKES with a circular pump in this work.

For RIKES with circular pump polarization and linear probe polarization, the components of the excitation fields may be written as

$$\begin{aligned} \vec{E}(\omega_S) &= E_y(\omega_S)\hat{y} \\ \vec{E}(\omega_p) &= E_x(\omega_p)\hat{x} + iE_y(\omega_p)\hat{y} \end{aligned} \tag{2.41}$$

where, for circular polarization

$$|E_x(\omega_p)| = |E_y(\omega_p)| = \frac{\left|\vec{E}(\omega_p)\right|}{\sqrt{2}} \tag{2.42}$$

For the Raman-induced Kerr effect, a nonlinear polarization density is created at the probe frequency ω_S orthogonal to the excitation field; that is, in the $\hat{x}$ direction. The polarization density can be written as:

$$\begin{aligned} P_x(\omega_S) = \frac{6i}{8}[&\chi_{1212}(-\omega_S,\omega_S,-\omega_p,\omega_p)E_y(\omega_S)E_x^*(\omega_p)E_y(\omega_p) \\ &-\chi_{1221}(-\omega_S,\omega_S,-\omega_p,\omega_p)E_y(\omega_S)E_y^*(\omega_p)E_x(\omega_p)] \end{aligned} \tag{2.43}$$

where using Eqn. 2.42, this reduces to

$$P_x(\omega_S) = \frac{3i}{8}\left[\chi_{1212} - \chi_{1221}\right] E_y(\omega_S) \left|E(\omega_p)\right|^2 \tag{2.44}$$

The signal field generated by this polarization is polarized perpendicular to the excitation field:

$$E_x(\omega_S) = -\frac{3\omega_S}{8n_S}\sqrt{\frac{\mu_0}{\varepsilon_0}}\chi_{eff}(-\omega_S, \omega_S, -\omega_p, \omega_p)E_y(\omega_S)\left|E(\omega_p)\right|^2 L \tag{2.45}$$

where $\chi_{eff} \equiv \chi_{1212} - \chi_{1221}$ at $|\omega_p - \omega_S| = \omega_{vib}$ (on resonance).

The relationship between $\operatorname{Im}\chi_{11ii}$ and the differential Raman scattering cross section is the same as in stimulated Raman scattering (see section 2.3):

$$\operatorname{Im}\chi_{11ii}(-\omega_S, \omega_S, -\omega_p, \omega_p) = \frac{8\pi^3}{3}\left(\frac{n_p\varepsilon_0^2 c^4}{n_S h\omega_p\omega_S^3}\right)\frac{d^2\sigma_{xi}}{d\Omega d\omega_S}(e^{-\frac{h(\omega_p-\omega_S)}{kT}} - 1) \tag{2.46}$$

allowing it to be shown that

$$\operatorname{Im}\chi_{eff}(-\omega_S, \omega_S, -\omega_p, \omega_p) = \frac{8\pi^3}{3}\left(\frac{n_p\varepsilon_0^2 c^4}{n_S h\omega_p\omega_S^3}\right)(1-3\rho)\frac{d^2\sigma_{xx}}{d\Omega d\omega_S}\left[e^{-\frac{h\omega_{vib}}{kT}} - 1\right] \tag{2.47}$$

where ρ is the depolarization ratio of the Raman mode ($\rho = \sigma_{xy}/\sigma_{xx}$) and $d^2\sigma_{xx}/d\Omega d\omega_S$ is the polarized peak differential Raman cross section per unit volume.

The intensity of the signal field is then:

$$I_x(\omega_S) = \frac{9}{16}\frac{\omega_S^2 L^2}{n_p^2 n_S^2}\left(\frac{\mu_0}{\varepsilon_0}\right)\left|\chi_{eff}(-\omega_S, \omega_S, -\omega_p, \omega_p)\right|^2 I_y(\omega_S) I^2(\omega_p) \tag{2.48}$$

The final Raman-induced Kerr effect intensity is thus proportional to the square of the sample interaction length as well as the pump intensity. It is linear in the probe intensity. This highlights the reason it is experimentally wise to use a strong pump and a weak probe, particularly in applications that are limited by photodamage caused by high combined average power of the two beams.

One of the main advantages of RIKES over CARS is the lack of any phase-matching requirement. Because the generated photons are emitted at frequency ω_S, the phase mismatch can be written:

$$\Delta\vec{k} = \vec{k_S} - \vec{k_p} + \vec{k_p} - \vec{k_S} = 0 \tag{2.49}$$

and thus the phase matching condition is identically satisfied. The overlap angle of the pump and probe beams does not matter experimentally.

2.4.1 Signal to noise of RIKES

For RIKES, the dominant source of noise is the birefringent background caused by depolarization of the probe pulse [6]. As the linearly polarized probe propagates from the initial polarizer to the analyzer, it passes through several optics. Each intervening optical element will contain some degree of static strain birefringence, introducing a slight ellipticity to the probe. When the signal is analyzed, the component of the probe beam now polarized perpendicular to the original probe beam will pass through the analyzer and show up as a background on the signal.

The signal current can be written as [6, 9]:

$$i^2_{signal} = [KAI_x(\omega_S)]^2 = K^2 P^2_R(\omega_S) \tag{2.50}$$

where A is the active detector area, $I_x(\omega_S)$ is given by Eqn. 2.48, and $P_R = AI_x$ being the incident power on the detector. The constant $K = Gqe/\hbar\omega$, where G is the gain of the detector, q is the quantum efficiency of the detector, and e is the charge of the electron. The classical noise power, then, associated with the birefringent background is

$$\varepsilon_B 1^2_B = \varepsilon_S K^2 P^2_B(\omega_S) \tag{2.51}$$

where $\varepsilon_S = \frac{<i^2_S(t) - i^2_S>}{i^2_S}$ is the fractional noise on the probe. Because the birefringent background $P_B(\omega_S)$ is itself a fraction of the total probe power (depending on the total degree of birefringence in the system), it can be written as

$$P_B = \delta P_y(\omega_S) \tag{2.52}$$

so that

$$\varepsilon_B i_B^2 = \varepsilon_S \left[K\delta P_y(\omega_S)\right]^2 \tag{2.53}$$

In addition to the classical laser noise contributed by the birefringent background, in the limit of very small Raman signal amplitudes, the shot noise of the background will also contribute to the overall noise. The shot noise may be written:

$$i_Q^2 = K_Q \left[i_d + K\delta P_y\right] \tag{2.54}$$

where i_d is the detector dark current and K_Q is the current of one electron per unit response time.

The final source of noise on the signal will be in the form of thermal noise, K_T. This is given by:

$$K_T = \frac{4kT\Delta\nu}{R} \tag{2.55}$$

where T is the temperature, k is Boltzmann's constant, $\Delta\nu$ is the detector bandwidth, and R is the detector load resistance.

We can combine the sources of noise in Eqns. 2.53, 2.54, and 2.55 to get a total noise of

$$\varepsilon_S \left[K\delta P_y(\omega_S)\right]^2 + K_Q \left[i_d + K\delta P_y\right] + \frac{4kT\Delta\nu}{R} \tag{2.56}$$

For our thermoelectrically cooled CCD camera, dark current and thermal noise is negligible compared to laser noise, giving a total signal-to-noise ratio for RIKES of

[6]:

$$(SNR)_{RIKES} = \frac{P_R^2}{\delta^2 P_y^2 (\varepsilon_S + \frac{2\hbar\omega_S \Delta\nu}{q\delta P_y})} \tag{2.57}$$

Remembering that the birefringent background power $P_B = \delta P_y(\omega_S)$, we can see that the size of the noise (denominator) is primarily determined by the size of the birefringent background. Thus, the birefringent background is the limiting factor in what kind of signal-to-noise ratio can be achieved in a Raman-induced Kerr effect experiment [6]. Further details on the birefringent background are discussed in section 4.3.

2.5 Surface-enhanced Raman scattering

Surface-enhanced Raman scattering (SERS) is the phenomenon of highly magnified Raman signals at the surface of nanoparticles or nanostructured substrates. Experiments of pyridine adsorbed on gold or silver particles of sub-wavelength size, dispersed colloidally in an aqueous medium, have shown surface-enhanced Raman signals at the surface of the particles [14–17]. For the general case of an analyte adsorbed to the surface of a spherical particle, an analytical solution can be calculated with the help of Lorenz-Mie theory. Although surface-enhanced Raman scattering can be detected on a variety of substrates, including nanostructured surfaces, nanoparticles, and nanorods, the case of a spherical particle is used in this derivation for computational simplicity.

Following the derivation of Wang, et al. [18], we consider a Raman scattering molecule located at coordinate $\mathbf{r}'$ on the surface or outside of a spherical particle of radius a and relative complex refractive index m_0 at frequency ω_0. For incident radiation as a plane wave of frequency ω_0, the scattering molecule may be approximated as a classical oscillating dipole radiating at a Raman frequency ω with dipole moment $\mathbf{p} = \alpha \mathbf{E}_p(\mathbf{r}', \omega_0)$, where α is the molecular Raman polarizability. The primary field $\mathbf{E}_p(\mathbf{r}', \omega_0)$ represents the incident field plus the elastically scattered field at $\mathbf{r}'$, calculated by Lorenz-Mie theory [18]:

$$\mathbf{E}_p(\mathbf{r}', \omega_0) = \mathbf{E}_i(\mathbf{r}', \omega_0) + \mathbf{E}_{LM}(\mathbf{r}', \omega_0) \tag{2.58}$$

For the limiting case of a small sphere centered at the origin, the primary field at $\mathbf{r}'$ is [18]:

$$\mathbf{E}_p(\mathbf{r}', \omega_0) = \mathbf{E}_i(\mathbf{r}', \omega_0) + \left(\frac{a^3}{\mathbf{r}'^3}\right) g_0 \left\{3\hat{n}' \left[\hat{n}' \cdot \mathbf{E}_i(\mathbf{r}', \omega_0)\right] - \mathbf{E}_i(\mathbf{r}', \omega_0)\right\} \tag{2.59}$$

where $\hat{n}' = \mathbf{r}'/r'$ and

$$g_0 = \frac{(m_0^2 - 1)}{(m_0^2 + 2)} \tag{2.60}$$

where the expression for $\mathbf{E}_{LM}(\mathbf{r}', \omega_0)$ in equation 2.58 is represented by the field of a point dipole at the origin. This primary field will induce the molecule to oscillate at the Raman frequency ω with dipole moment $\mathbf{p} = \alpha \mathbf{E}_p(\mathbf{r}', \omega_0)$. At the origin, the field induced by the Raman scattering dipole is given by:

$$\mathbf{E}_d(0, \omega) = \frac{[3\hat{n}'(\hat{n}' \cdot \mathbf{p}) - \mathbf{p}]}{r'^3} \tag{2.61}$$

In the radiation zone, the total electric field can be represented as due to that of dipole $\mathbf{p}$ coherently added to the field of a dipole located at the origin given by [18]:

$$\mathbf{p}' = g a^3 \mathbf{E}_d(0, \omega) \tag{2.62}$$

where

$$g = \frac{(m^2 - 1)}{(m^2 + 2)} \tag{2.63}$$

with m being the relative refractive index at ω.

The total power, then, in the radiation zone is given by:

$$P_1 = \left(\frac{ck^4}{3}\right) \left|\mathbf{p}' + \mathbf{p}\right|^2 \tag{2.64}$$

where $k = n_0\omega/c$, n_0 is the index of refraction of the medium surrounding the particle, and c is the speed of light.

To calculate the enhancement factor, we can consider the Raman scattered field in the absence of the nanosphere as an electric dipole with a dipole moment $\mathbf{p}'' = \alpha\mathbf{E}_i(\mathbf{r}', \omega_0)$ and a total radiated power of $P_2 = \left[\frac{ck^4}{3}\right] \cdot \left|\mathbf{p}''\right|^2$. The enhancement factor can be written [18]:

$$EF = \frac{\left|\mathbf{p}' + \mathbf{p}\right|^2}{\left|\mathbf{p}''\right|^2} \tag{2.65}$$

Substituting the proper expressions for the dipole moments, we arrive at an enhancement factor of:

$$EF = \left|\hat{i} + \frac{a^3}{r'^3} g_0 \left[3\hat{n}'\left(\hat{n}' \cdot \hat{i}\right) - \hat{i}\right] + \frac{a^3}{r'^3} g \left[\left(\frac{a^3}{r'^3} g_0 - 1\right)\hat{i} + \left(\frac{a^3}{r'^3} g_0 + 1\right) 3\hat{n}'\left(\hat{n}' \cdot \hat{i}\right)\right]\right|^2 \tag{2.66}$$

For particles with size sufficiently smaller than the wavelength of excitation light, the enhancement factor is independent of particle size. For m_0^2 or $m^2 \rightarrow -2$, very large enhancements are possible.

2.5.1 Surface-enhanced coherent anti-Stokes Raman scattering

Surface-enhanced coherent anti-Stokes Raman scattering (SECARS) is a process that is analogous to SERS in which CARS is performed on molecules near a nanostructured metal surface. In this manner, analysis of the radiation outside of spherical particle can proceed in a similar way to that of section 2.5. Figure 2.5 shows the excitation geometry for the analysis of SECARS by Chew, et al. for a spherical particle [19]. Two incident laser beams at frequencies ω_1 and ω_2 are incident on a particle

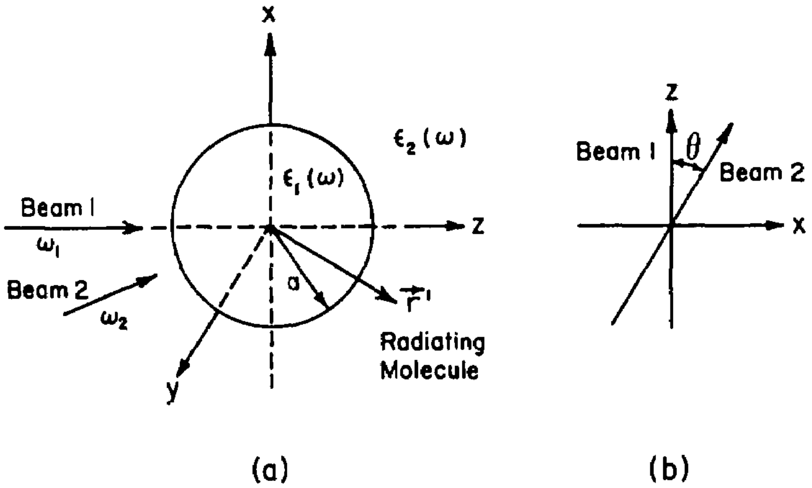

Figure 2.5: Incident beam geometry for surface-enhance coherent anti-Stokes Raman scattering with a spherical particle. a) Geometry of incident beams with particle. b) Directions of incident beams in the x-z plane [19].

with radius a (centered at the origin). Beam 1 propagates along the z axis and beam 2 propagates at angle θ with respect to the z axis, with the beams intersecting at the small particle. The medium inside the particle can be labeled 1, and the medium inside the particle can be labeled 2.

Similar to the analysis of the preceding section, we consider a Raman-active molecule at coordinate $\mathbf{r}'$ outside the particle. Again, the local field $E_\alpha(\omega_\alpha, \mathbf{r}')$ at frequency $\omega_\alpha(\alpha = 1, 2)$ at $\mathbf{r}'$ is the sum of the incident and scattered fields. These local fields E_1 and E_2 produce a dipole moment $\mathbf{p}_c$, which in turn radiates at the CARS frequency $\omega_3 = 2\omega_1 - \omega_2$. The dipole moment can be written [20, 21]:

$$\begin{aligned}\mathbf{p}_c = \mathbf{p}_c(\mathbf{r}') &= 6\chi_{1122}(\omega_1, \omega_1, -\omega_2)E_1(\omega_1, \mathbf{r}')E_2^*(\omega_2, \mathbf{r}')E_1(\omega_1, \mathbf{r}') \\ &\quad + 3\chi_{1221}(\omega_1, \omega_1, -\omega_2)E_1(\omega_1, \mathbf{r}')E_1(\omega_1, \mathbf{r}')E_2^*(\omega_2, \mathbf{r}') \\ &\equiv \chi E_1 E_2^* E_1 + \chi' E_1 E_1 E_2^* \end{aligned} \tag{2.67}$$

where χ_{1122} and χ_{1221} are components of the nonlinear susceptibility tensor, with

$\chi = 6\chi_{1122}$ and $\chi' = 3\chi_{1221}$. The dipole field produced at $\mathbf{r}$ is then [22]:

$$\begin{aligned}\mathbf{E}_d(\omega_3, \mathbf{r}, \mathbf{r}') = &\sum_{\ell,m} \frac{ic}{n_2^2(\omega_3)\omega_3} a_E^d(\ell, m) \nabla \times \left[h_\ell^{(1)}(k_3 r) \mathbf{Y}_{\ell\ell m}(\hat{r}) \right] \\ &+ \sum_{\ell,m} a_M^d(\ell, m) h_\ell^{(1)}(k_3 r) \mathbf{Y}_{\ell\ell m}(\hat{r}) \end{aligned} \tag{2.68}$$

where $n_2(\omega_3)$ is the refractive index outside of the medium at the CARS frequency and k_3 is the corresponding wave number, with $\mathbf{Y}$ representing the relevant spherical harmonic and $h_\ell^{(1)}$ representing the Hankel function of the first kind. $a_E^d(\ell, m)$ and $a_M^d(\ell, m)$ are given by [22]:

$$a_E^d(\ell, m) = 4\pi k_3^2 \sqrt{\frac{\mu_2(\omega_3)}{\epsilon_2(\omega_3)}} \times \mathbf{p}_c(\mathbf{r}') \cdot \left\{ \nabla' \times \left[h_\ell^{(1)}(k_3 r') \mathbf{Y}_{\ell\ell m}^*(\hat{r}) \right] \right\} \tag{2.69}$$

$$a_M^d(\ell, m) = 4\pi i \left(\frac{k_3^2 \omega_3}{c} \right) \sqrt{\frac{\mu_2(\omega_3)}{\epsilon_2(\omega_3)}} \times h_\ell^{(1)}(k_3 r') \mathbf{p}_c(\mathbf{r}') \cdot \mathbf{Y}_{\ell\ell m}^*(\hat{r}) \tag{2.70}$$

The scattered field $\mathbf{E}_{sc}$ at $\mathbf{r}$ can be shown to be [22]:

$$\begin{aligned}\mathbf{E}_{sc}(\omega_3, \mathbf{r}, \mathbf{r}') = &\sum_{\ell,m} \frac{ic}{n_2^2(\omega_3)\omega_3} b_\ell(\omega_3) a_E^d(\ell, m) \nabla \times h_\ell^{(1)}(k_3 r) \mathbf{Y}_{\ell\ell m}(\hat{r}) \\ &+ \sum_{\ell,m} a_l(\omega_3) a_M^d(\ell, m) h_\ell^{(1)}(k_3 r) \mathbf{Y}_{\ell\ell m}(\hat{r}) \end{aligned} \tag{2.71}$$

where $a_\ell(\omega_3)$ and $b_\ell(\omega_3)$ are Lorenz-Mie coefficients evaluated at the CARS frequency. The total CARS field at $\mathbf{r}$ will be:

$$\mathbf{E}_{tot}(\omega_3, \mathbf{r}, \mathbf{r}') = \mathbf{E}_d(\omega_3, \mathbf{r}, \mathbf{r}') + \mathbf{E}_{sc}(\omega_3, \mathbf{r}, \mathbf{r}') \tag{2.72}$$

Far away from the surface of the particle, the detected field will be:

$$E_{tot}(\omega_3, \mathbf{r}, \mathbf{r}') \rightarrow \frac{e^{ik_3 r}}{r} \left[E_d(\mathbf{r}, \mathbf{r}') + E_{sc}(\mathbf{r}, \mathbf{r}') \right] \tag{2.73}$$

where

$$E_d(\mathbf{r},\mathbf{r}') = \sum_{\ell,m} i^{-\ell+1}\left[\frac{c}{n_2^2(\omega_3)\omega_3} a_E^d(\ell,m)\hat{r}\times\mathbf{Y}_{\ell\ell m}(\hat{r}) - a_M^d(\ell,m)\mathbf{Y}_{\ell\ell m}(\hat{r})\right] \tag{2.74}$$

and

$$E_{sc}(\mathbf{r},\mathbf{r}') = \sum_{\ell,m} i^{-\ell+1}\left[\frac{cb_\ell(\omega_3)}{n_2^2(\omega_3)\omega_3} a_E^d(\ell,m)\hat{r}\times\mathbf{Y}_{\ell\ell m}(\hat{r}) - a_\ell(\omega_3)a_M^d(\ell,m)\mathbf{Y}_{\ell\ell m}(\hat{r})\right] \tag{2.75}$$

It can be seen from these results that the CARS field can be enhanced in several different ways. If the laser frequency ω_1 is located at a resonance frequency of the particle, the local field $E_1(\omega_1,\mathbf{r}')$ will be enhanced because the scattered field will be large, resulting in an enhanced dipole moment from equation 2.67. Enhancement will also occur if the resonance overlaps with ω_2, although the increase will not be as large due to the linear dependence of $\mathbf{p}_c$ on E_2 relative to its quadratic dependence on E_1. For particle resonances overlapping ω_3, enhancement occurs owing to the magnification of the Mie coefficients $a_\ell(\omega_3)$ and $b_\ell(\omega_3)$ in the magnitude of the scattered field E_{sc} (equation 2.75). For SERS substrates with very broad plasmonic resonances, the possibility of quadruple resonances exists if all CARS fields overlap in frequency with the surface plasmon resonances [22]. In this case, extremely high enhancement factors are thought to be possible in surface-enhanced CARS experiments.

References

[1] M. Born and K. Huang. *Dynamical Theory of Crystal Lattices.* Clarendon Press, 1954.

[2] C. S. Wang. Theory of stimulated Raman scattering. *Physical Review*, 182:482–494, 1969.

[3] G. Placzek. *Marx Handbuch der Radiologie.* Academische Verlagsgesellschaft, 1934.

[4] P. D. Maker and R. W. Terhune. Study of optical effects due to an induced polarization third order in electric field strength. *Physical Review*, 137:801–819, 1965.

[5] Y. R. Shen. *The Principles of Nonlinear Optics.* John Wiley & Sons, Inc., 2003.

[6] G. L. Eesley. *Coherent Raman Spectroscopy.* Elsevier, Oxford, 1981.

[7] A. Zumbusch, G. R. Holtom, and X. S. Xie. Three-dimensional vibrational imaging by coherent anti-Stokes Raman scattering. *Physical Review Letters*, 82(20):4142–4145, May 17 1999.

[8] E. J. Woodbury and W. K. Ng. Ruby operation in the Near IR. *Proc. Inst. Radio Eng.*, 50:2367, 1962.

[9] G. L. Eesley. Coherent Raman Spectroscopy. *Journal of Quantitative Spectroscopy & Radiative Transfer*, 22(6):507–576, 1979.

[10] D. Heiman, R. W. Hellwarth, M. D. Levenson, and G. Martin. Raman-induced Kerr Effect. *Physical Review Letters*, 36(4):189–192, 1976.

[11] C. W. Freudiger, M. B. J. Roeffaers, X. Zhang, B. G. Saar, W. Min, and X. S. Xie. Optical heterodyne-detected Raman-induced Kerr effect (OHD-RIKE) microscopy. *The Journal of Physical Chemistry B*, 5(ASAP):103–109, 2011.

[12] M. D. Levenson and N. Bloembergen. Dispersion of the nonlinear optical susceptibility tensor in centrosymmetric media. *Physical Review B*, 10:4447–4463, 1974.

[13] R. T. Lynch, M. D. Levenson, and N. Bloembergen. Experimental test for deviation from Kleinman's symmetry in the third order susceptibility tensor. *Physics Letters A*, 50:61–62, 1974.

[14] J. A. Creighton, C. G. Blatchford, and M. G. Albrecht. Plasma Resonance Enhancement of Raman-scattering by Pyridine Adsorbed on Silver or Gold Sol Particles of Size Comparable to the Excitation Wavelength. *Journal of the Chemical Society-Faraday Transactions II*, 75:790–798, 1979.

[15] A. Campion and P. Kambhampati. Surface-enhanced Raman scattering. *Chemical Society Reviews*, 27:241, 1998.

[16] M. Moskovits. Surface-enhanced Raman Spectroscopy: a Brief Perspective. *Topics in Applied Physics*, 103:1–17, 2006.

[17] P. L. Stiles, J. A. Dieringer, N. C. Shah, and R. P. van Duyne. Surface-Enhanced Raman Spectroscopy. *Annual Review of Analytical Chemistry*, 1:601–626, 2008.

[18] D. S. Wang, H. Chew, and M. Kerker. Enhanced Raman scattering at the surface (SERS) of a spherical particle. *Applied Optics*, 19:2256–2257, 1980.

[19] H. Chew, D. S. Wang, and M. Kerker. Surface enhancement of coherent anti-Stokes Raman scattering by colloidal spheres. *Journal of the Optical Society of America B*, 1:56–66, 1984.

[20] J. Cooney and A. Gross. Coherent anti-Stokes Raman scattering by droplets in the Mie size range. *Optics Letters*, 7:218–226, 1982.

[21] A. Gross. *Coherent anti-Stokes Raman scattering by droplets of the Mie size range*. PhD thesis, Drexel University, 1982.

[22] H. Chew, M. Kerker, and D. D. Cooke. Electromagnetic scattering by a dielectric sphere and in diverging radiation field. *Physical Review A*, 16:320–323, 1977.

CHAPTER III

Coherent versus spontaneous Raman

In this chapter, the methods and experimental setup of a systematic comparison between coherent and spontaneous Raman spectroscopy and microscopy are explained in detail. We utilize a configuration in which the mode of excitation can be easily switched between spontaneous and coherent Raman. Spectroscopy measurements are made in solution comparing signal levels as a function of excitation power, and a microscopy comparison is performed via Raman imaging of polystyrene beads. We find that for low-concentration, low-excitation power conditions (such as those relevant for biological imaging), spontaneous Raman often provides higher signal levels than coherent Raman techniques.

3.1 Motivation

A number of purported advantages over spontaneous Raman scattering has made coherent anti-Stokes Raman scattering (CARS) the subject of many spectroscopy and microscopy studies over the past decade [1–5]. Most recent literature has held the general assumption that CARS is superior to spontaneous Raman scattering methods on the basis of several advantages. First, as a multiphoton process, CARS provides automatic 3D sectioning when used with microscopy. Due to the nonlinear dependence on incident intensity, as the excitation beam diverges from its focus, the signal drops off much more quickly than it does in the case of spontaneous Raman. Thus, similar to confocal microscopy, CARS does not suffer from out-of-focus signal background in the same way that spontaneous Raman does. Second, CARS can be detected to the blue (anti-Stokes) side of the excitation wavelengths. This allows signal detection in a spectral region that will not suffer from background due to fluorescence (although care must still be taken to avoid background due to two-photon excited fluorescence). Because spontaneous Raman signals are redshifted, samples with significant fluorescence overlap with the Raman bands will have severe non-vibrational signal contamination. Finally, the coherent oscillation of molecules in the sample give rise to a collective signal generation that adds up constructively over the interaction length, greatly enhancing the Raman signal. CARS has been shown to provide several orders of magnitude signal improvement over spontaneous Raman under the right experimental conditions [6].

For imaging biological samples, the final advantage is perhaps the most appealing. Due to the sensitivity of biological samples to photodamage, orders of magnitude higher signal means much lower excitation power, allowing microscopy of tissue without loss of cellular function. Although CARS microscopy has quickly grown in popularity in recent years, very little work has been done to systematically compare the relative signal strengths of CARS and spontaneous Raman methods. Despite this, claims of 4-5 orders of magnitude are often cited in the literature [7–11]. For biological imaging, however, we are limited to low excitation powers and low sample concentrations, both of which mitigate the advantages conferred by CARS. In the work presented here, we compare the relative signal strengths of CARS and spontaneous Raman scattering under the low-concentration and low-power conditions relevant to biological imaging. We show that the signal strengths of the two methods are comparable in this situation [12], contrary to what is commonly asserted in the literature [1, 2, 4].

In making a valid comparison between CARS and spontaneous Raman, methods of suppressing the nonresonant background must be employed to isolate the chemically-specific Raman signal. Techniques include pulse-delay CARS, which takes advantage of the short lifetime of the nonresonant signal to isolate the resonant signal [13, 14]. Also used are polarization CARS, which takes advantage of the difference in polarization state of the nonresonant signal relative to the resonant signal [15], phase-matching-based methods [16], amplitude-based methods [17, 18], and heterodyne-detected CARS [19]. The method of suppressing nonresonant background used in this work is a time delay method. Similar studies have been performed recently using time delay suppression, using nJ-μJ pulses with a low repetition rate laser (kHz-MHz). These studies have compared coherent Stokes Raman scattering (CSRS) to spontaneous Raman, finding an increased CSRS signal level over spontaneous Raman by a factor of $100 - 10^5$ [20–22].

Biological imaging, on the other hand, has low tolerance for such high pulse energies. Generally, high repetition rate (∼80 MHz) lasers must be used with low intensity (pJ) pulses for non-destructive imaging of biological samples. Photodamage studies have shown cell destruction at relatively low powers using near-IR 80 MHz excitation. In hamster ovary cells, cell death has been shown to occur at ∼4.5 mW for 240 fs duration pulses and ∼7.3 mW for 2.2 ps duration pulses [23]. In bovine adrenal cells, loss of cell viability has been shown to occur at ∼2.5-3.0 mW for 190 fs duration pulses [24]. It is under conditions similar to these that we present our comparison between CSRS and spontaneous Raman.

3.2 History

Coherent anti-Stokes Raman scattering (CARS) was first demonstrated by Maker and Terhune at Scientific Laboratory of the Ford Motor company [25]. Using a pulsed ruby laser with a pulse energy of 0.1 J with 30 ns duration, Maker and Terhune

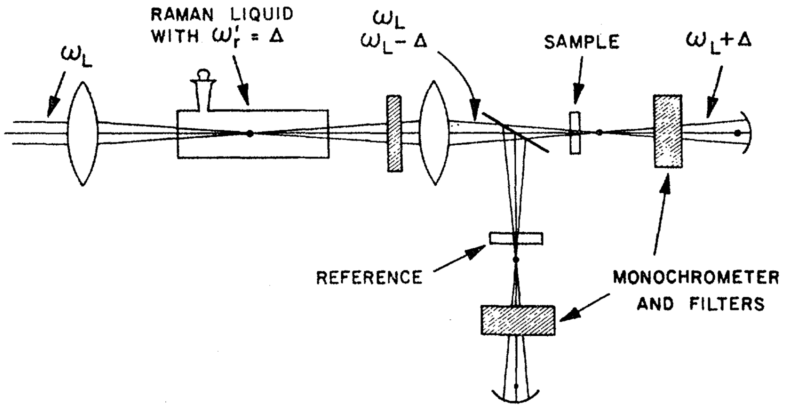

Figure 3.1: Experimental setup of first CARS experiment by Maker and Terhune [25].

produced a second beam using Raman laser action in a 20 cm long benzene cell with frequency components at $\omega \pm n\Delta$, where n is an integer and Δ is a Raman frequency of the liquid. All frequencies except those at ω and $\omega - \Delta$ are then filtered out. Combining these two beams in a sample, Maker and Terhune were able to detect frequency components at $\omega + \Delta$. Though they referred to these experiments simply at "Three Wave Mixing Experiments", this process would later become known as coherent anti-Stokes Raman scattering. Figure 3.1 shows a diagram of the original CARS experiment by Maker and Terhune.

CARS microscopy was first demonstrated nearly twenty years later with the developments of Duncan et al. in 1982[1], but the complicated nature of the noncollinear setup made such an implementation difficult in practice. In addition, the visible dye lasers used gave rise to large nonresonant background signals that degraded the chemical contrast. In the 90s it was shown that use of a high numerical aperture objective can relax the phase-matching requirement, allowing a collinear geometry to be used [3, 26]. The use of near-IR excitation light also reduced the observed nonresonant background signals. It was this development that allowed the rapid expansion of CARS as a method of vibrational microscopy, as an experimental geometry that allows the collinear recombination of beams allows the use of a laser-scanning microscope. With sufficiently high signal and single-band detection, video rate CARS imaging can be achieved in such a geometry [27].

The rapid advancement of CARS microscopy has highlighted a need to carefully evaluate its advantages and disadvantages in comparison to spontaneous Raman. As mentioned in section 3.1, Pestov et al. recently performed such a comparison in solutions of pyridine. Figure 3.2 shows the comparison of spontaneous and coherent Raman spectra retrieved from pyridine. These results show a significant improvement in CSRS over spontaneous Raman for the excitation conditions used. The conditions used for this measurement were 0.13 mW (0.13 μJ/pulse 1 kHz repetition rate) for spontaneous spectra with loose focusing ($\gtrsim 50\mu m$ spot size for the excitation beams). For CSRS measurements, the same pulses are used as the probe pulses, delayed by 1.8 picoseconds with respect to the 0.72 μJ/pulse pump and the 1.36 μJ/pulse Stokes pulses. The low repetition rate and high pulse energies used in this experiment are generally not viable for biological imaging, necessitating the systematic study of the relative performance under such conditions.

The work presented in this chapter extends this previous work to biological imaging conditions. Rather than using pulse energies on the order of 1 μJ at 1 kHz, we will perform the studies with pulse energies on the order of 1 pJ at 75 MHz. The low pulse energy and high repetition rate used here will allow us to determine whether coherent or spontaneous Raman methods will deliver higher signal levels for fragile biological samples.

3.3 Experimental Setup

To make the most straightforward comparison possible between coherent and spontaneous Raman, we use the three-color time delay approach similar to Petrov et al. [21]. Shown in Figure 3.3, the excitation scheme consists of a pump pulse (ω_p) and a Stokes pulse (ω_S) exciting a coherence in the sample. A time delay τ later,

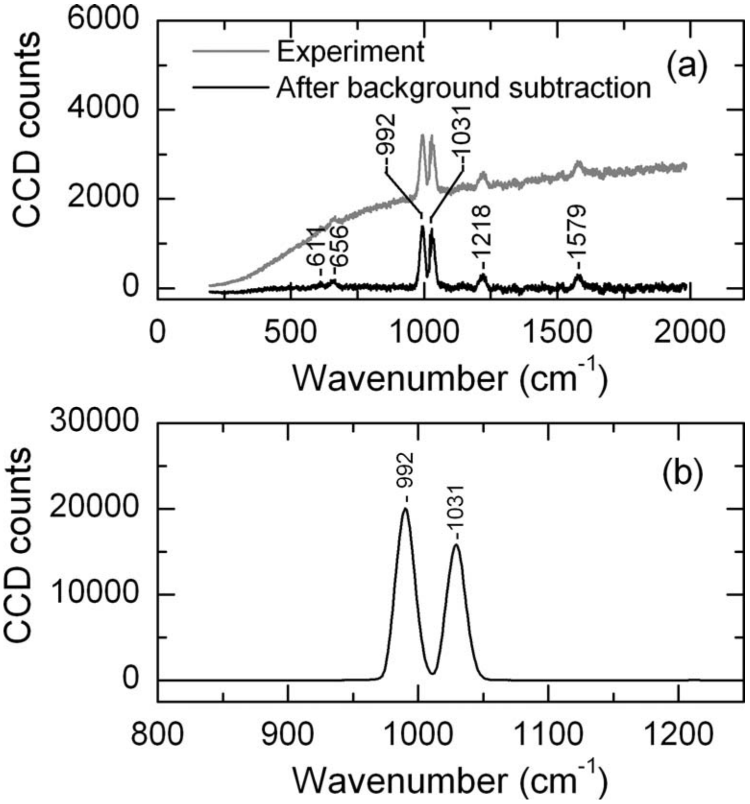

Figure 3.2: Experimental results of Pestov's coherent versus spontaneous Raman comparison. a) spontaneous Raman spectrum of pyridine. b) CSRS spectrum of pyridine [20].

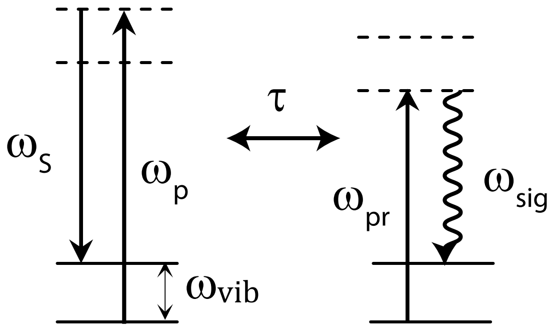

Figure 3.3: Energy level diagram for coherent Stokes Raman scattering. Relevant beam frequencies denoted as ω_S (Stokes), ω_p (pump), ω_{pr} (probe), and ω_{sig} (signal).

a third pulse (ω_{pr}) probes the sample, at which point Stokes radiation (ω_{sig}) can be detected. Because coherent nonresonant background is an electronic four-wave mixing process, it has a much shorter lifetime than the resonant signal. By choosing τ to be longer than the electronic nonresonant lifetime but shorter than the lifetime of the coherence generated by the pump and Stokes pulses, effective nonresonant signal suppression can be achieved. Coherent Stokes Raman scattering (CSRS) is used rather than coherent anti-Stokes Raman scattering (CARS) because the experimental implementation is easier for direct comparison. Changing the setup between CSRS and spontaneous Raman requires only blocking the CSRS pump pulses at the Fourier plane and allowing the probe to act as the spontaneous excitation beam. No changes in detector or experimental alignment are necessary.

The laser source used for the experiment is a broadband Ti:sapphire oscillator (Femtosource Synergy) with 12 nJ pulses (110 nm bandwidth) centered at 785 nm, operating at a 75 MHz repetition rate. The full spectrum of the oscillator is shown in Figure 3.4. The beam is spectrally dispersed in a 4f pulse shaper, and an amplitude mask is placed at the Fourier plane to produce the three distinct excitation pulses. Figure 3.5 shows the spectrum of the three excitation pulses used. The pump pulse at ω_p is centered at 736 nm and the Stokes pulse at ω_S is centered at 793 nm, giving

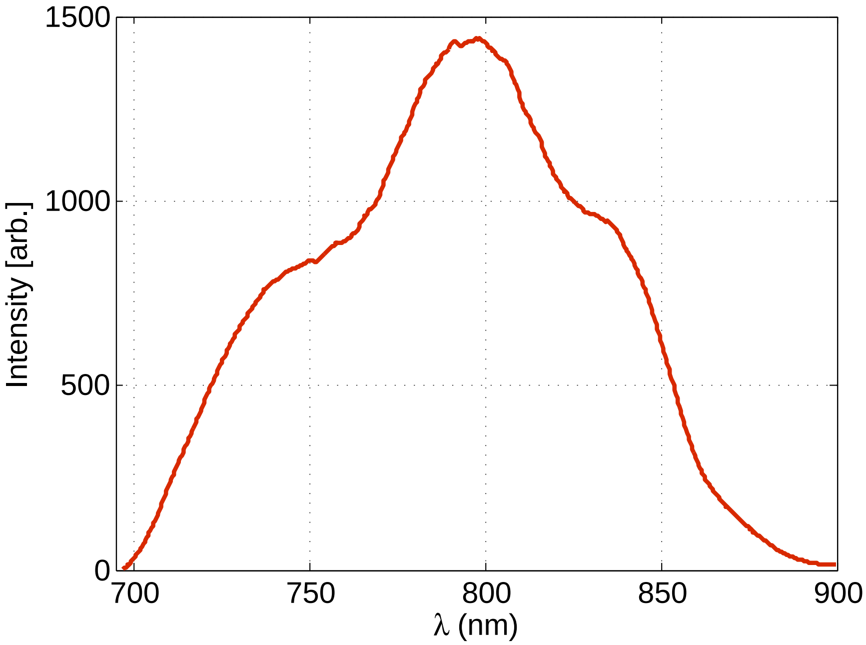

Figure 3.4: Full spectrum of Femtosource Synergy Ti:sapph oscillator.

$\sim$1000 cm^{-1} separation between them to excite the 1000 cm^{-1} Raman vibrational mode of polystyrene. The probe pulse at ω_{pr} is centered at 835 nm, putting the CSRS detection wavelength at 911 nm. The spectral resolution of the signal is determined by the spectral width of the probe, which has a bandwidth of 43 cm^{-1}.

Figure 3.6 shows the experimental setup for the measurement. The beam comes out of the oscillator and is immediately sent into a reflective 4f pulse shaper, where it is dispersed with an amplitude mask at the Fourier plane. The amplitude mask consists of three slits – one for each of the excitation beams shown in Fig. 3.5. In the path of the probe pulse, an 800 fs time delay is introduced by a small glass coverslide. This provides the time delay τ sufficient to suppress the nonresonant background signal at 1000 cm^{-1} while maintaining $> 80\%$ of the resonant signal. When switching between coherent and spontaneous measurements, a physical beam block is placed in front of the pump and Stokes slits at the Fourier plane, and an ND filter placed before the objective is adjusted to equalize the total power between the two methods.

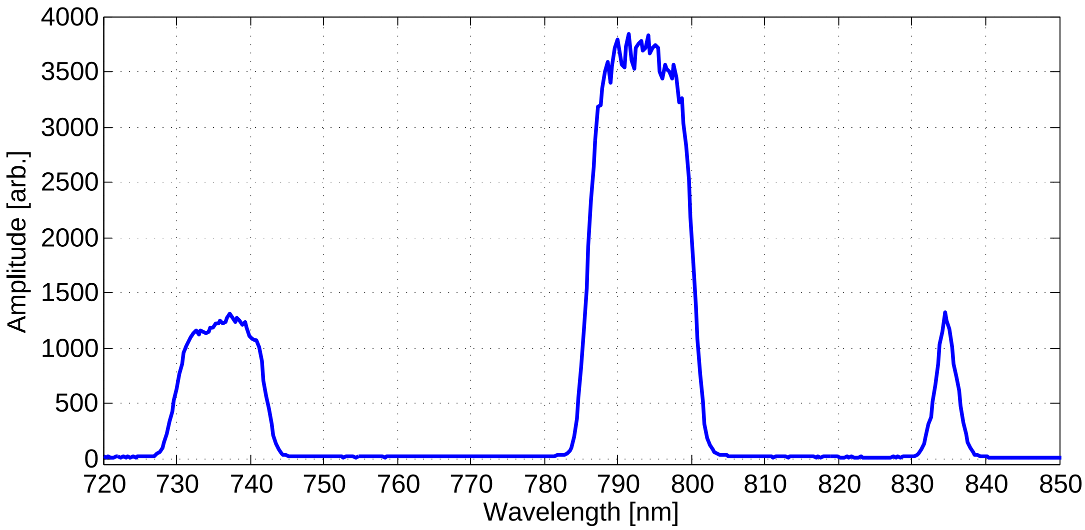

Figure 3.5: Amplitude mask used for three-color CSRS experiment with polystyrene sample.

The excitation pulses are compensated for second-order group velocity dispersion using chirped mirrors. Each of the pulses is characterized by second-order autocorrelation using a two-photon GaAsP photodiode. Figure 3.7 shows autocorrelation traces for each of the beams: a) pump, b) Stokes, and c) probe. The pump pulse (Fig. 3.7a) has a duration of 106 fs. The Stokes pulse (Fig. 3.7b) has a duration of 113 fs. The probe pulse (Fig. 3.7c) has a duration of 672 fs. Each of the pulse durations is within 10% of its respective transform-limited pulse duration. After dispersion compensation, the beams are focused onto the sample by a 0.4 NA air objective (Olympus LM plan IR, 20 ×) giving a confocal parameter of $8.0 \pm 0.4\mu m$. The approximate focal volume of the beam in the sample is calculated to be

$$\begin{aligned} V &= \pi(1.3 \pm 0.07)^2 \times (8 \pm 0.4)\mu m^3 \\ &\approx 42.5\mu m^3 \end{aligned} \tag{3.1}$$

Following the objective, the beam is focused onto the sample, which is mounted on an $x - y$ piezo stage for raster-scanning images. The signal is collected with collection

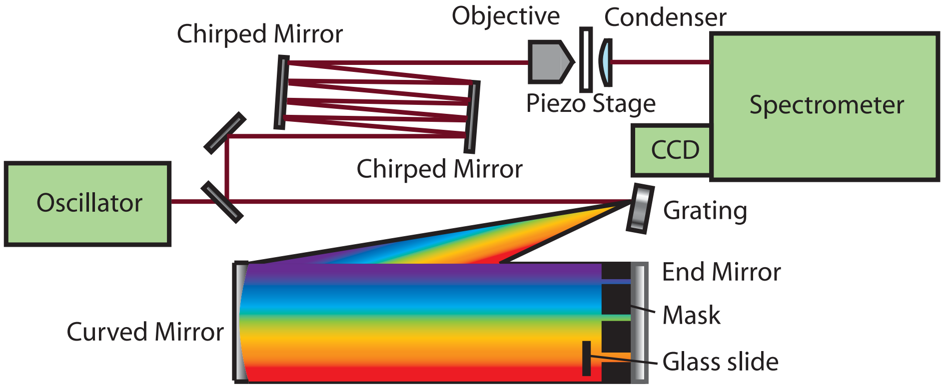

Figure 3.6: Experimental diagram for CSRS versus spontaneous Raman scattering measurement.

optics with a total NA of 0.6, where the excitation pulses are spectrally filtered using interference filters. The signal is directed into a spectrometer (Jobin Yvon IHR320), and spectra are acquired with a Pixis 100F CCD. Samples used in the experiment are 2-propanol for solution measurements and polystyrene beads (7.3 μm and 4.3 μm diameter) for imaging.

3.4 Measurements in solution

As a simple test of the power dependence of CSRS versus spontaneous Raman signal, measurements are first performed in solution. A solution of pure 2-propanol is prepared and placed at the focus of the excitation beams, in place of the piezo stage in Figure 3.6. Because the depth of focus of the excitation beams after the objective is $\sim 8\mu m$, we must be careful when preparing our sample to ensure a valid comparison between the two methods is made. CSRS is a multiphoton process, so the coherent excitation will only occur over the extent of the ($\sim 8\mu m$) tight focus. Spontaneous Raman, on the other hand, is a one-photon linear process and will occur throughout the full beam path within the sample cell. As a result, we want to make our sample with a thickness such that the total excitation volume is equal for both

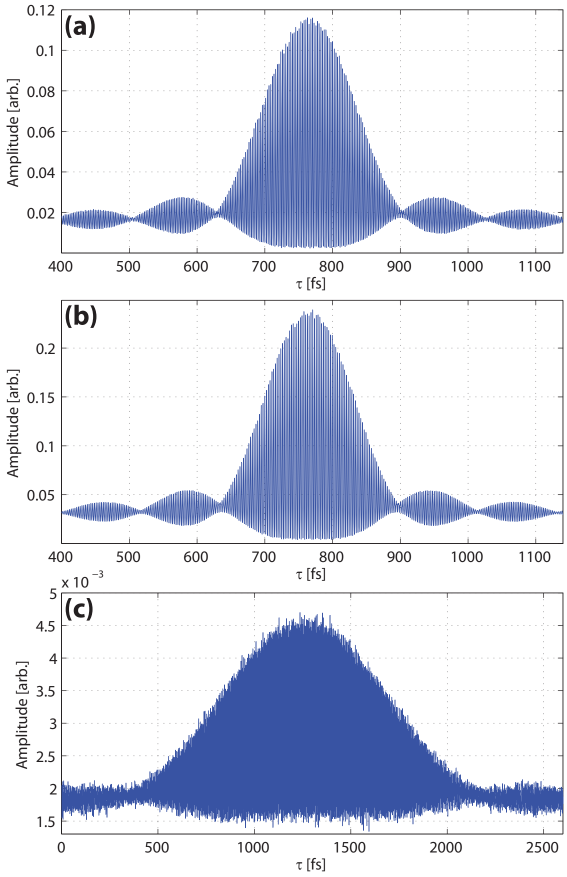

Figure 3.7: Autocorrelation for three pulses in CSRS versus spontaneous Raman measurement. a) Pump pulse, ∼106 fs duration. b) Stokes pulse, ∼113 fs duration. c) Probe pulse, ∼672 fs duration.

Raman techniques.

To accomplish this, two 1 mm thick fused silica slides are placed together with two small squares of 18 μm thick aluminum foil sandwiched between them. The foil squares are placed at two corners on the same end of the slides. When the slides are sealed together, they form an empty wedge-shaped cell with variable width from 0 μm to 18 μm, corresponding to the end without foil and the end with foil, respectively. The cell is then filled with pure 2-propanol and placed at the focus, where its position can be adjusted perpendicular to the z-direction. This allows us to calculate the true thickness of the sample by measuring the signal dependence as a function of sample position. The thickness of the sample in this case is calculated to be $10\mu m \pm 1\mu m$.

Figure 3.8 shows the Raman spectrum of 2-propanol. For these measurements in solution, we are exciting the 820 cm^{-1} Raman vibrational mode corresponding to the dominant C-C stretching mode, giving us a detection wavelength of 901 nm. Figure 3.9 shows the signal strength of each method as a function of total excitation power. For CSRS, the power of all three beams combined is considered the total excitation power. For spontaneous Raman, the pump and Stokes beams are blocked and the probe power is considered to be the total excitation power. Due to the limited spectral density profile of the Ti:sapph oscillator, the maximum time-averaged power that could be achieved in the probe beam is $\sim$ 1.3 mW. For this reason, the achievable power in the spontaneous Raman setup cannot approach the much higher levels of excitation power in the CSRS setup, as shown in Figure 3.9. CSRS data is plotted as maroon dots, and the data is fitted to a cubic function (red dotted line) because the signal power dependence is proportional to the product of the three excitation power levels ($P_{CSRS} \propto P_p P_S P_{pr}$). Spontaneous Raman data is plotted as dark blue dots, and the data is fitted to a linear function for the same reason ($P_{Raman} \propto P_{pr}$). In both cases, the cubic and linear dependencies are shown to hold extremely well, with the norm of residuals being 45.4 for the CSRS fit and 22.4 for the spontaneous

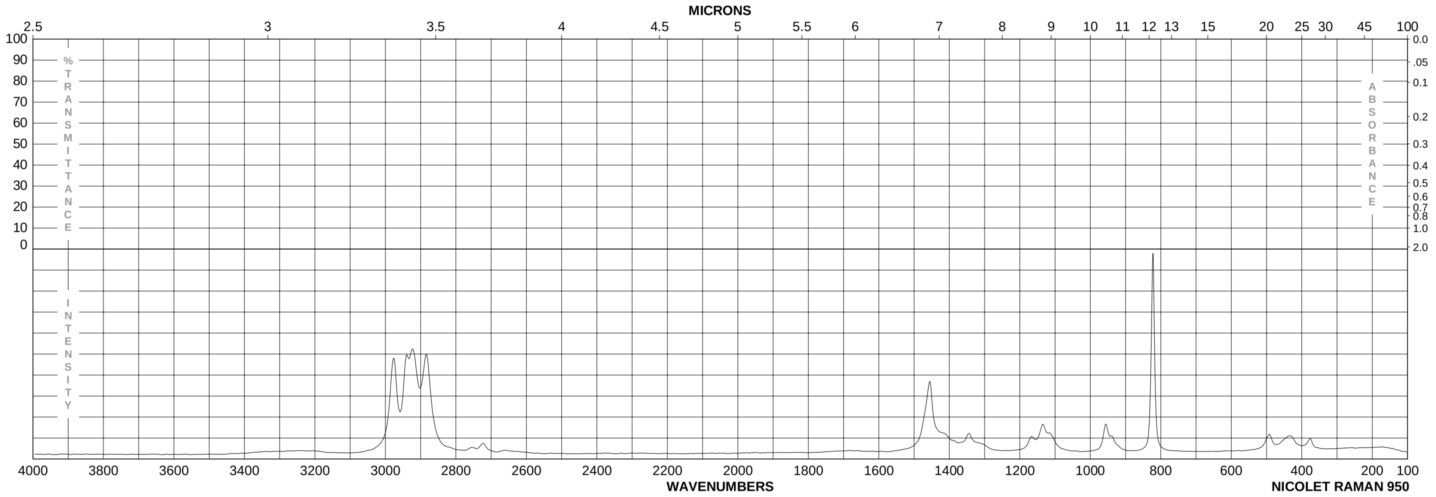

Figure 3.8: Spontaneous Raman spectrum for 2-propanol [28].

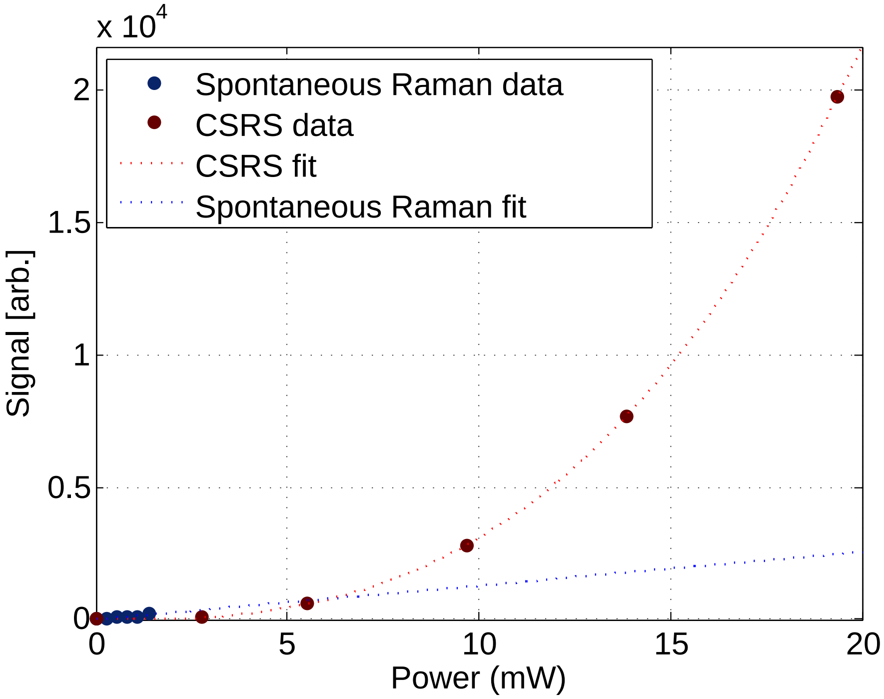

Figure 3.9: CSRS versus spontaneous Raman data and fits in solution of 2-propanol. Curve fitting is done with linear (spontaneous Raman) and cubic (CSRS) functions.

Raman fit.

Figure 3.10 shows the same comparison zoomed in on the low-power region of interest. It can be seen that, based on the extrapolated fit of the spontaneous Raman data, there is a critical power at which coherent Raman methods give higher signal levels than spontaneous Raman methods. Below this power, spontaneous Raman scattering proves to give higher signal. For our experimental conditions, this critical power is ~ 6.2 mW. Because the shape of the Ti:sapph spectral envelope is transferred to the individual pulse amplitudes (ultimately limiting the maximum power available in each beam), the CSRS excitation does not use the most efficient excitation power ratio (1:1:1). If the beams can be individually controlled such that the power is equal in each of them, the CSRS signal can be amplified by a factor of ~ 3.5, leading to a reduction in critical power to ~ 3.3 mW. In cases of very low excitation power, spontaneous Raman signal from the CSRS probe will be the dominant source of signal

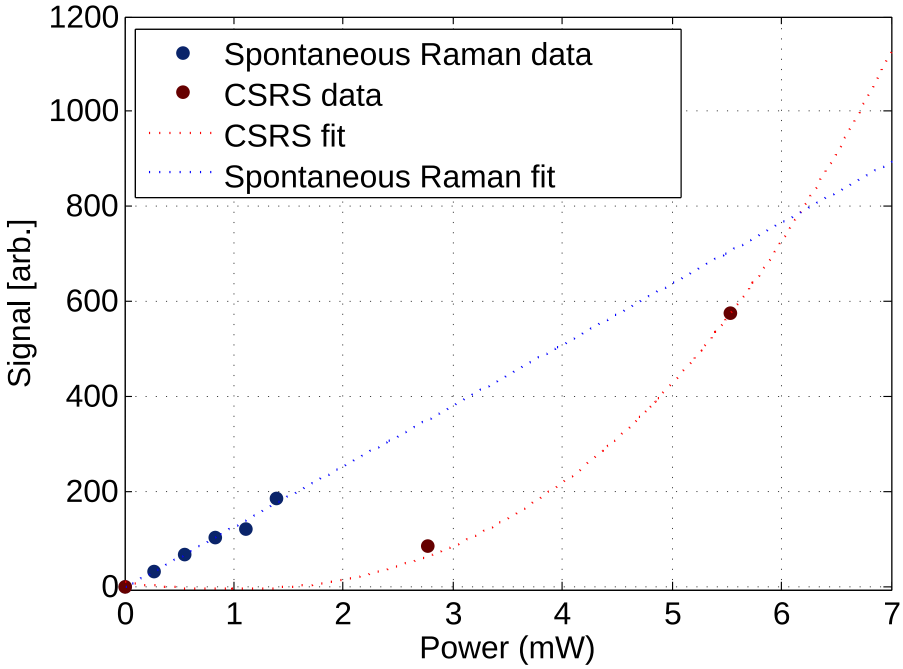

Figure 3.10: Critical power of solution of 2-propanol for CSRS and Raman. CSRS and spontaneous Raman give equal signal levels at ∼ 6.2 mW of total power.

in the CSRS experiment. If a (1:1:1) power ratio is used for the excitation beams, the lower limit for the amount of Raman signal in the CSRS setup should be equal to one third of that in the spontaneous Raman setup. This corresponds to no coherent contribution to the signal.

3.5 Imaging polystyrene beads

The time-delay CSRS scheme was used to image polystyrene beads dried onto a glass coverslide. Image contrast is achieved by taking the difference between the spectral intensity at 1000 cm^{-1} (on resonance) and 950 cm^{-1} (off resonance). Figure 3.11a shows a CSRS image of 7.3μm beads taken with 4 mW total combined power of the three excitation beams, using a dwell time of 40 ms/pixel. The image has a total scan range of 30μm × 30μm. A time delay of 800 fs is used between the

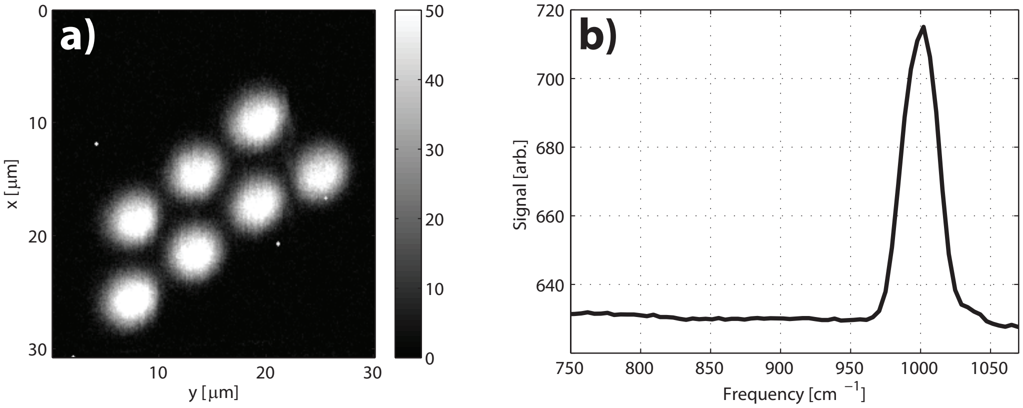

Figure 3.11: a) CSRS image of 7.3 μm diameter polystyrene beads. Total power used for excitation is 4 mW. Each pixel has a dwell time of 50 ms/pixel. b) Averaged spectrum taken inside beads shown in (a). Polystyrene Raman mode seen at 1000 cm^{-1}.

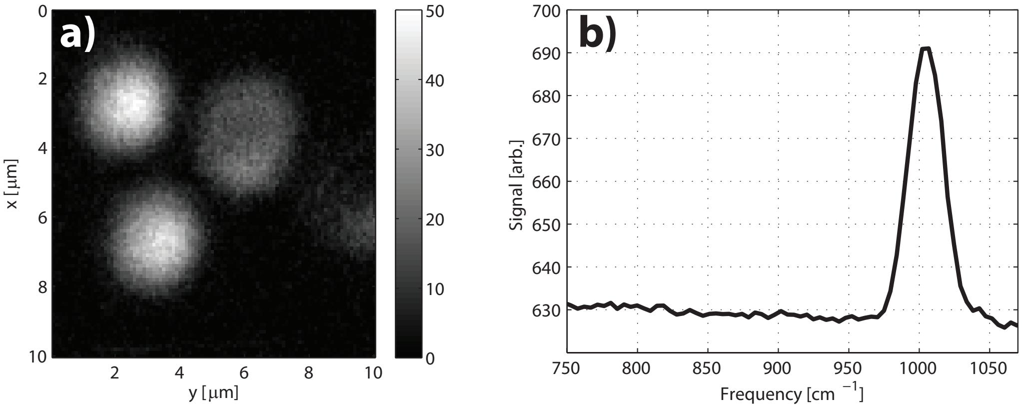

Figure 3.12: a) CSRS image of 4.3 μm diameter polystyrene beads. Total power used for excitation is 4 mW. Each pixel has a dwell time of 50 ms/pixel. b) Averaged spectrum taken inside beads shown in (a). Polystyrene Raman mode seen at 1000 cm^{-1}.

pump/Stokes and probe fields to suppress nonresonant background. Figure 3.11b shows the averaged spectrum taken from pixels inside the polystyrene beads shown in Fig. 3.11a. As can be seen, the narrow polystyrene peak at 1000 cm^{-1} is prominent without the presence of a nonresonant background. The linewidth of the 1000 cm^{-1} peak in Fig. 3.11b is determined by the bandwidth of our probe pulse to be $\sim$ 40 cm^{-1}. Figure 3.12a shows similar images taken with 4.3 μm beads. The total range of this scan is $10\mu m \times 10\mu m$, and 4 mW of total excitation power is again used. The dwell time for this image is 50 ms/pixel. The averaged spectrum from the centers of the beads is shown in Fig. 3.12b.

Figure 3.13 shows a comparison between CSRS and spontaneous Raman imaging in $7\mu m$ polystyrene beads. Figure 3.13a shows CSRS images taken on beads with 1.3 mW of power (0.29 mW pump, 0.93 mW Stokes, and 0.08 mW probe). Figure 3.13b shows the same image taken with spontaneous Raman (i.e. the pump and Stokes pulses are blocked, and the average power of the probe pulse only is increased to 1.3 mW). Spontaneous Raman shows slightly higher (but comparable) image intensity in the polystyrene bead. The beads appear larger in the spontaneous Raman images because the signal has linear dependence on the interaction length, rather than the quadratic dependence as in CSRS. Thus, the relative contribution from the edges of the beads where the interaction length is thin will be larger in the case of spontaneous Raman than in CSRS, making them more visible in the images. Figure 3.13c shows spectra taken from the centers of the beads in Figures 3.13a and 3.13b. It can be seen that the peak heights are nearly equal for the two methods for 1.3 mW excitation, with a very small ($\sim$ 3 CCD counts) offset between the background levels of the two methods.

Figure 3.14 shows a similar comparison done with 4 μm beads. Images shown are $10\mu m \times 10\mu m$. For these images, 1.3 mW of average power is again used with a 200 ms/pixel dwell time. Fig. 3.14a shows the CSRS image (0.29 mW pump, 0.93

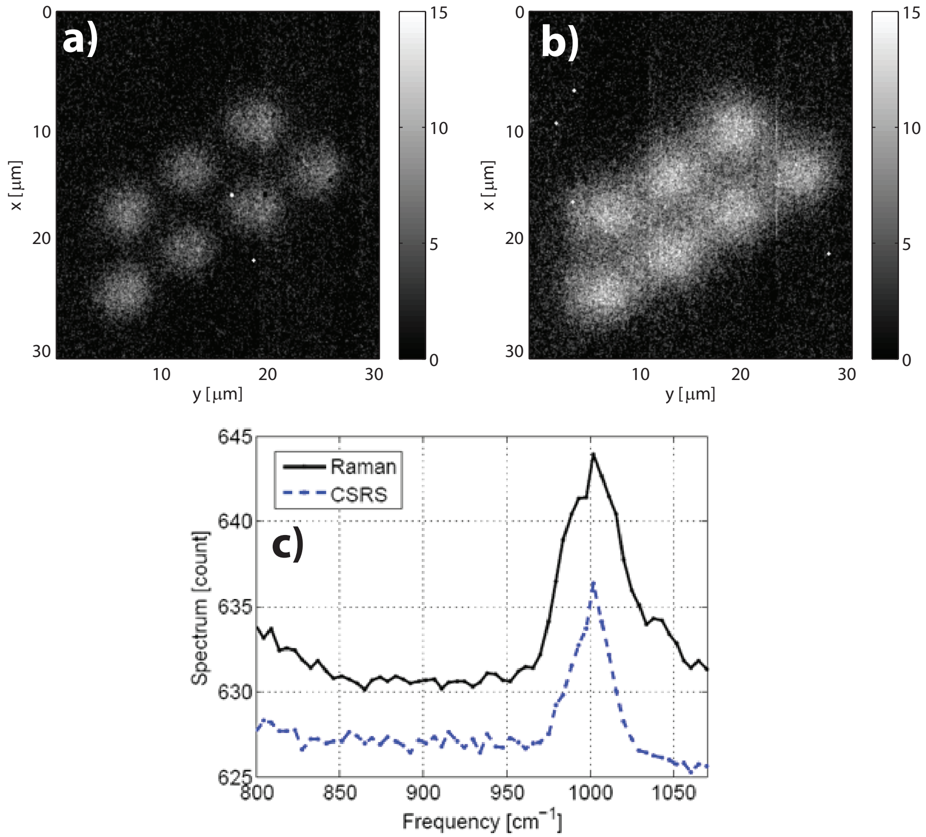

Figure 3.13: a) CSRS image of 7.3 μm diameter polystyrene beads using 0.29 mW pump, 0.93 mW Stokes, and 0.08 mW probe power with 100 ms/pixel dwell time. b) Spontaneous Raman image with 1.3 mW total power and 100 ms/pixel dwell time. c) Averaged spectra from the centers of the beads in (a) and (b).

mW Stokes, and 0.08 mW probe), and Fig. 3.14b shows the spontaneous Raman image of the polystyrene beads. Figure 3.14c shows the comparison of spectra taken at the center of the beads. The 1000 cm^{-1} peak has nearly identical strength for both methods from the pixels at the center of the beads. It can be clearly seen, however, that the pixels at the edge of the beads show more 1000 cm^{-1} intensity for the spontaneous Raman images because of the linear interaction length dependence. From these spectra, it is clear that the critical power at which the two methods give equal signal strength takes place at $\sim$ 1.3 mW for this sample. If the optimized power ratio between the three excitation pulses (1 : 1 : 1) is used for CSRS, the signal can be increased by a factor of $\sim$ 3.5, reducing the critical power by a factor of $\sim$ 2 to $\sim$ 0.7 mW.

In both cases, the signal collected using spontaneous Raman is highly dependent on the collection optics. While CSRS signal is emitted directionally in the forward and backwards direction, spontaneous Raman is emitted in all directions, filling the full 4π solid angle around the sample. Thus, spontaneous signal collection efficiency can be directly increased or decreased based on the effective numerical aperture of the collection optics. In our case, we use a 0.8 NA condenser to collect the signal, which is reduced to an effective NA of $\sim$ 0.6 due to the size mismatch of the optics following the condenser. In real imaging applications, it is difficult to get a significantly higher collection efficiency, although high NA objectives can be used to provide some improvement. Any further improvements afforded by increasing collection efficiency will increase the spontaneous Raman signal relative to the CSRS signal.

3.6 Calculation

To make an estimate on the relative signal strengths of CSRS and spontaneous Raman expected in our experiment, we perform a calculation based on the derivation of Tolles et al. [6]. From the Tolles review paper, we use equations (4), (5), (19),

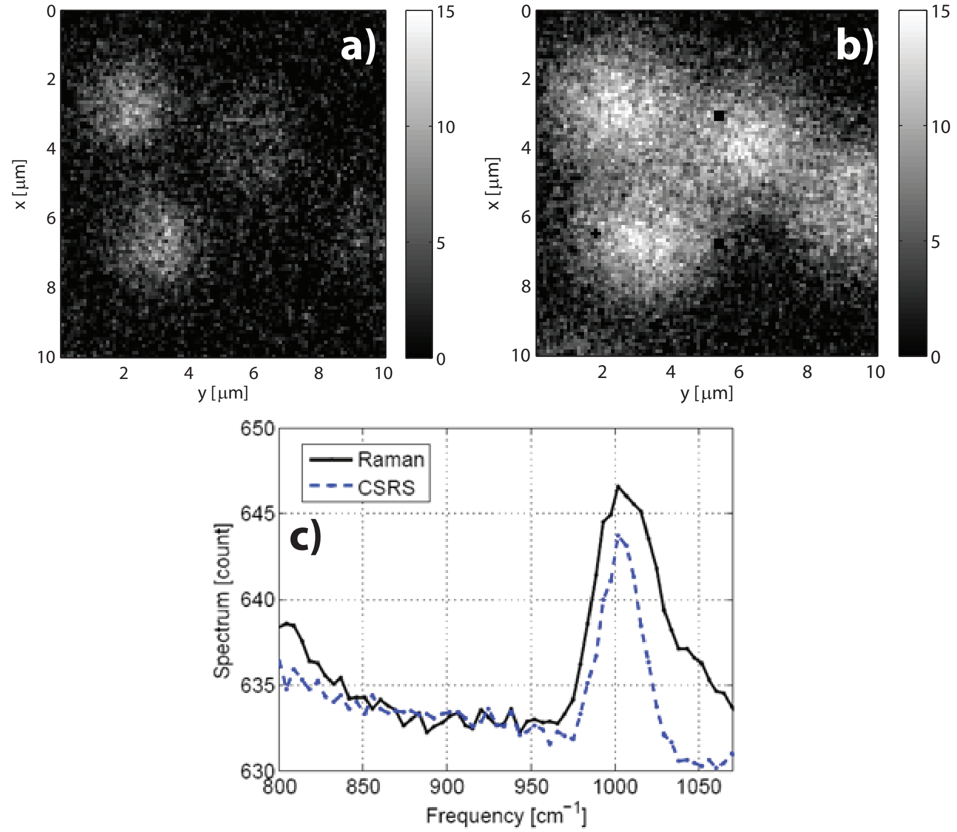

Figure 3.14: a) CSRS image of 4.3 μm diameter polystyrene beads using 0.29 mW pump, 0.93 mW Stokes, and 0.08 mW probe power with 100 ms/pixel dwell time. b) Spontaneous Raman image with 1.3 mW total power and 100 ms/pixel dwell time. c) Averaged spectra from the centers of the beads in (a) and (b).

and (27) to calculate the expected signal for both techniques. The signal strength for spontaneous Raman can be written:

$$P_{Raman} = \left(\frac{c}{8\pi}\right)|E_{pr}|^2 ALN\frac{d\sigma}{d\Omega}\Omega_{coll} \tag{3.2}$$

while the signal strength for CSRS can be written:

$$P_{CSRS} = \int_0^\infty \left(\frac{2\pi\omega_{sig}^2}{cn_S^2}\right) L^2 A \left[\frac{3}{8}\int_0^\infty \chi^{(3)} B(\Delta) \times E_{pr}(\omega+\Delta)d\Delta\right]^2 d\omega \tag{3.3}$$

where (in cgs units), E_{pr} is the electric field of the probe, L is the interaction length of the sample, A is the cross-sectional area of the excitation region, N is the number density of molecules, $d\sigma/d\omega$ is the differential Raman scattering cross section, and Ω_{coll} is the total solid angle of collection for the spontaneous Raman measurement.

In Equation 3.3, n_S is the index of refraction of the sample at the CSRS signal wavelength, ω_{sig} is the frequency of the emitted CSRS radiation, and $\chi^{(3)}$ is given by:

$$\chi^{(3)} = \frac{\omega_{vib}\Lambda}{3(\omega_{vib}^2 - \Delta^2 - i\Gamma\Delta)} \tag{3.4}$$

where $\Delta = (\omega_p - \omega_S)$, ω_{vib} is the frequency of the Raman vibrational mode, and Γ is a damping constant related to the full-width at half-max of the linewidth γ by the relation:

$$\Gamma = \frac{2\pi\gamma}{\sqrt{3}} \tag{3.5}$$

The constant Λ is given by:

$$\Lambda = \frac{2Nc^4}{\hbar\omega_{sig}^4}\left(\frac{d\sigma}{d\Omega}\right) \tag{3.6}$$

and the term $B(\Delta)$ is given by:

$$B(\Delta) = \int_0^\infty E_1(\omega' + \Delta)E_2^*(\omega')d\omega \tag{3.7}$$

From these equations, we can calculate our expected signal power based on our experimental conditions. Using Equations 3.2 and 3.3, we input the following experimental parameters: 1) CSRS excitation power of $P_p = 0.29$ mW, $P_S = 0.93$ mW, and $P_{pr} = 0.08$ mW. 2) Spontaneous Raman equivalent total excitation power of $P_{pr} = 1.3$ mW. When set up to perform CSRS, there will be a spontaneous Raman contribution from the probe pulse only. We estimate this contribution to be $\sim 6\%$ of the total CSRS signal. Other experimental parameters used in the calculation are focal diameter $= (1.4 \pm 0.1)\mu m$, confocal parameter $= (8.0 \pm 0.4)\mu m$, polystyrene bead density $= 1.05 g/cm^3$, $L = (4.3 \pm 0.1)\mu m$, $n_S = 1.55$, and $\Omega_{coll} = (1.45 \pm 0.4)$ steradians. A solid angle correction factor of $1/n_S$ is not appropriate to use in our case because of our spherical sample geometry [29].

To get an appropriate value for the Raman cross section of the 1000 cm^{-1} mode of polystyrene (i.e. the dominant ring-breathing mode), we compared signal levels between polystyrene and pyridine [30] using Fourier transform CARS measurements [31]. Using these measurements, we find that the differential Raman cross section is $d\sigma/d\omega = (2.4\times10^{-30} \pm 0.6\times10^{-30}) cm^2/sr/molecule$ with a linewidth of $\gamma = 8 \pm 2 cm^{-1}$. This value takes into account the difference in detection wavelength between the pyridine measurements (513 nm) and our measurements (911 nm). It also takes into account the difference in excitation wavelength (ω_{pr}) for our sample. Using these values, we estimate a signal ratio between the two methods of:

$$\frac{P_{CSRS}}{P_{Raman}} = 6 \pm 3 \tag{3.8}$$

Given our experimental conditions, we calculate an estimated ratio of CSRS/Raman power of 6 ± 3, which is reasonably consistent with our experimental results presented in section 3.5.

3.7 Discussion

Biological imaging often involves samples with very low concentrations, down to or below the millimolar range, depending on the particular molecular vibration being probed. The experiments done here were done with dense solid polystyrene samples with concentrations of ~ 10 M. At low biological imaging concentrations, the critical power at which coherent and spontaneous Raman will provide comparable signal levels will be higher, resulting from the quadratic dependence on N for coherent methods versus the linear dependence on N for spontaneous methods. Decreasing the concentration of the sample will decrease the signal more quickly with coherent methods than spontaneous methods, so the excitation power must be increased to keep the signal ratio at one when mapping out the critical power.

Figure 3.15 maps out the critical power dependence on sample concentration and excitation power, using the experimental results of this study as a guideline. The polystyrene measurements done here are shown as a red star in Fig. 3.15. Based on this measurement and the signal ratio dependence on excitation power and sample concentration (i.e. $P_{CSRS}/P_{Raman} \propto NP^2$), an equivalence line is drawn (solid black line) from our measured critical power across the full range of concentrations and power levels. This line represents the critical power as a function of experimental concentration and power parameters. Below this line, spontaneous methods give higher signal. Above this line, coherent methods give higher signal levels. The dashed line shows the same equivalence line, adjusted for optimized power ratio $(1:1:1)$ for CSRS and NA 1.2, using an interaction length L of half the confocal parameter.

Indicated by the letters a, b, and c in Fig. 3.15 are photodamage limits for hamster ovary cells obtained from the literature [23, 32]: a) 2-3 mW, 150 fs pulses, 0.35 TW/cm^2 peak intensity; b) 4.5 mW, 240 fs pulses, 0.33 TW/cm^2 peak intensity; c) 7.3 mW, 2.2 ps pulses, 0.058 TW/cm^2 peak intensity. Rat brain tissue photodamage limits established by Hell, et al. of 0.15 TW/cm^2 for 80 fs duration pulses [33] agree with these photodamage limits. Bovine adrenal cell photodamage limits established by Hopt and Neher of 0.11 TW/cm^2 for 190 fs pulses [24] also agree with these limits. The peak intensities used in this experiment are 0.16 TW/cm^2 for the CSRS excitation and 2.8 GW/cm^2 for spontaneous excitation.

In Figure 3.15, the blue shaded region represents the experimental conditions under which coherent Raman methods will provide higher signal, and the unshaded region represents the conditions under which spontaneous Raman methods give higher signal. The dashed box represents the area relevant for standard biological imaging conditions. The dotted box extends this area to include biological samples of particularly high concentration, such as tightly-packed lipid membranes, which can reach oscillator densities as high as ~ 40 M. Figure 3.15 should not change significantly when using picosecond pulses.

3.8 Conclusions

We have performed the first systematic comparison of spontaneous Raman versus coherent Raman signal levels under biological imaging conditions. In contrast with previous work, the excitation power, pulse energy, focusing, and signal collection closely resemble the conditions used for biological imaging [20]. Using previous studies as a guide, we compare our results within the framework of maximum power before photodamage, showing that in many instances, spontaneous Raman imaging can provide even higher signal levels than coherent Raman imaging. Spontaneous Raman also has the advantage of providing high-resolution broadband spectra that are not susceptible to the nonresonant background that plagues CARS and CSRS

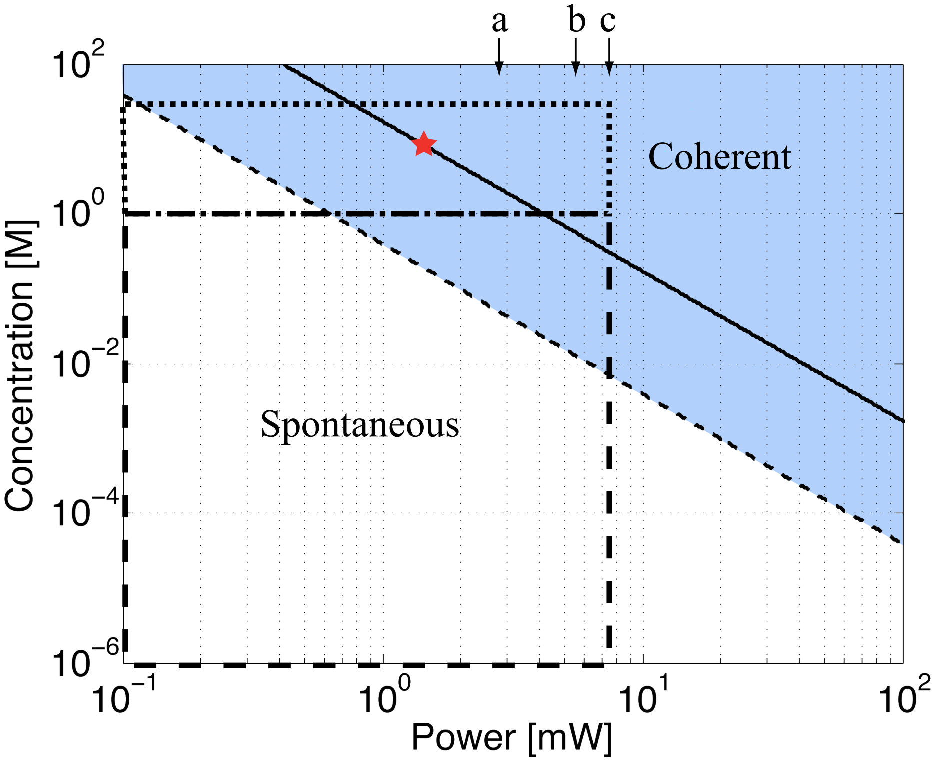

Figure 3.15: CSRS/spontaneous Raman signal strength ratio as a function of excitation power and concentration. The solid line represents the critical power at which the two methods give equal signal as a function of sample concentration. Above the line, coherent methods give higher signal. Below the line, spontaneous methods give higher signal. The red star indicates the measurement performed in our experiment at 10 M concentration and $\sim$ 1.3 mW critical power for the 1000 cm^{-1} mode of polystyrene. The dashed line shows the critical power as a function of sample concentration for the same sample if the optimized pulse power ratio (1:1:1) and NA 1.2 are used. Arrows at the top indicate photodamage limits found in the literature: a) 2-3 mW, 150 fs pulse duration, 80 μs dwell time[23]; b) 4.5 mW, 240 fs pulse duration, 60 μs dwell time[23]; c) 7.3 mW, 2.2 ps pulse duration, 60 μs dwell time[32]. These values are in agreement with those found in rat brain tissue [33]. The dashed box represents the excitation power and concentration values encountered most often for biological imaging, while the dotted box extends beyond these parameters to include the imaging of dense biological samples, such as C-H stretch modes in densely packed lipids.

imaging. If CW lasers are used with spontaneous Raman detection, the experimental setup is greatly simplified, and the peak intensity of the excitation light can be greatly reduced compared to pulsed lasers. On the other hand, coherent methods have the advantage of providing automatic 3D sectioning, although this advantage could be conferred to spontaneous Raman imaging using a confocal geometry. Additionally, CARS can be detected to the blue of the excitation wavelengths, allowing the acquisition of images without detecting red-shifted fluorescence background. For samples that are particularly resistent to photodamage, coherent methods can often provide significantly higher signal levels.

Using the theory developed by Tolles et al., we have estimated the ratio of CSRS to spontaneous Raman power from our sample of polystyrene beads using 1.3 mW of excitation power. This result is in reasonable agreement with our experimental result, showing comparable signal levels for the two methods. For the experimental conditions used here, the critical power is in the 1.3 mW range for polystyrene beads and in the 6.2 mW range for pure 2-propanol solution. Samples with lower concentration will have a higher critical power, indicating spontaneous Raman will provide higher signal levels than CSRS. When designing a biological imaging experiment, care must be taken in deciding whether to use coherent or spontaneous Raman methods based on the relative signal levels, among other considerations. The advantages and disadvantages of each technique will determine which method is more suitable for the imaging application being considered. The surge in publications using CARS imaging [2–4, 8, 14, 15, 18, 27, 34–37] has necessitated a systematic comparison of signal strength of coherent versus spontaneous Raman scattering. Little work has been done comparing the advantages and disadvantages of each methods under biological imaging conditions. While many of these previous studies have taken advantage of the high signal and density of Raman oscillators found in the C-H stretch of lipids, finer chemical specificity can be found in the fingerprint region ($\sim 700 - 1800\ cm^{-1}$), where the Raman oscillator density can be much lower. The work here provides a foundation to quantify the experimental conditions under which each method will provide higher signal levels, showing that spontaneous Raman imaging can in fact offer signal strength advantages in the low-concentration, low-excitation power realm of biological imaging.

References

[1] M. D. Duncan, J. Reintjes, and T. J. Manuccia. Scanning coherent anti-Stokes Raman microscope. *Opt. Lett.*, 7(8):350–352, 1982.

[2] M. Muller and J. M. Schins. Imaging the thermodynamic state of lipid membranes with multiplex CARS microscopy. *Journal of Physical Chemistry B*, 106(14):3715–3723, Apr 2002.

[3] A. Zumbusch, G. R. Holtom, and X. S. Xie. Three-dimensional vibrational imaging by coherent anti-Stokes Raman scattering. *Physical Review Letters*, 82(20):4142–4145, May 17 1999.

[4] J. X. Cheng, A. Volkmer, and X. S. Xie. Theoretical and experimental characterization of coherent anti-Stokes Raman scattering microscopy. *Journal of the Optical Society of America B-Optical Physics*, 19(6):1363–1375, Jun 2002.

[5] J. P. Ogilvie, K. J. Kubarych, A. Alexandrou, and M. Joffre. Fourier transform measurement of two-photon excitation spectra: applications to microscopy and optimal control. *Optics Letters*, 30(8):911–913, Apr 15 2005.

[6] W. M. Tolles, J. W. Nibler, J. R. McDonald, and A. B. Harvey. Review of theory and application of coherent anti-Stokes Raman spectroscopy (CARS). *Applied Spectroscopy*, 31(4):253–271, 1977.

[7] J. X. Cheng and X. S. Xie. Coherent anti-Stokes Raman scattering microscopy: Instrumentation, theory, and applications. *Journal of Physical Chemistry B*, 108:827–840, 2004.

[8] B. von Vacano, L. Meyer, and M. Motzkus. Rapid polymer blend imaging with quantitative broadband multiplex CARS microscopy. *Journal of Raman Spectroscopy*, 38:916–926, 2007.

[9] A. Volkmer. Vibrational imaging and microspectroscopies based on coherent anti-Stokes Raman scattering microscopy. *Journal of Physics D - Applied Physics*, 38:R59–R81, 2005.

[10] T. W. Kee, H. X. Zhao, and M. T. Cicerone. One-laser interferometric broadband coherent anti-Stokes Raman scattering. *Optics Express*, 14:3631–3640, 2006.

[11] H. A. Rinia, M. Bonn, M. Muller, and E. M. Vartiainen. Quantitative CARS spectroscopy using the maximum entropy method: The main lipid phase transition. *ChemPhysChem*, 8:279–287, 2007.

[12] M. Cui, B. Bachler, and J. P. Ogilvie. Comparing coherent and spontaneous Raman scattering under biological imaging conditions. *Optics Letters*, 34:773–775, 2009.

[13] F. M. Kamga and M. G. Skeats. Pulse-sequenced coherent anti-Stokes Raman scattering spectroscopy: a method for suppression of the nonresonant background. *Optics Letters*, 5:126, 1980.

[14] A. Volkmer, L. Book, and X. S. Xie. Time-resolved coherent anti-Stokes Raman scattering microscopy: Imaging based on Raman free induction decay. *Applied Physics Letters*, 80:1505, 2002.

[15] J. X. Cheng, L. D. Book, and X. S. Xie. Polarization coherent anti-Stokes Raman scattering microscopy. *Optics Letters*, 26(17):1341–1343, Sep 1 2001.

[16] A. Volkmer, J. X. Cheng, and X. S. Xie. Vibrational imaging with high sensitivity via epidetected coherent anti-Stokes Raman scattering microscopy. *Phys. Rev. Lett.*, 87:023901, 2001.

[17] O. Burkacky, A. Zumbusch, C. Brackmann, and A. Enejder. Dual-pump coherent anti-Stokes Raman scattering microscopy. *Optics Letters*, 31:3656–3658, 2006.

[18] Y. Yoo, D. Lee, and H. Cho. Differential two-signal picosecond-pulse conherent anti-Stokes Raman scattering imaging microscopy by using a dual-mode optical parametric oscillator. *Optics Letters*, 32:3254–3256, 2007.

[19] E. Potma, C. Evans, and X. S. Xie. Heterodyne coherent anti-Stokes Raman scattering (CARS) imaging. *Optics Letters*, 31:241–243, 2006.

[20] D. Pestov, G. O. Ariunbold, X. Wang, R. K. Murawski, V. A. Sautenkov, A. V. Sokolov, and M. O. Scully. Coherent versus incoherent Raman scattering: molecular coherence excitation and measurement. *Optics Letters*, 32(12):1725–1727, Jun 2007.

[21] G. I. Petrov, R. Arora, V. V. Yakovlev, X. Wang, A. V. Sokolov, and M. O. Scully. Comparison of coherent and spontaneous Raman microspectroscopies for noninvasive detection of single bacterial endospores. *Proceedings of the National Academy of Sciences of the United States of America*, 104(19):7776–7779, May 2007.

[22] G. I. Petrov, R. Arora, A. Saha, R. D. Heathcote, S. Ravula, I. Brener, and V. V. Yakovlev. Raman versus CARS microscopy: when one is better than the other - art. no. 644209. In A. So P. T. C. Periasamy, editor, *Conference on Multiphoton Microscopy in the Biomedical Sciences VII*, pages 44209–44209, San Jose, CA, Jan 21-23 2007.

[23] K. Konig, P. T. C. So, W. W. Mantulin, and E. Gratton. Cellular response to near-infrared femtosecond laser pulses in two-photon microscopes. *Optics Letters*, 22(2):135–136, Jan 1997.

[24] A. Hopt and E. Neher. Highly nonlinear photodamage in two-photon fluorescence microscopy. *Biophysical Journal*, 80:2029–2036, 2001.

[25] P. D. Maker and R. W. Terhune. Study of optical effects due to an induced polarization third order in electric field strength. *Physical Review*, 137:801–819, 1965.

[26] A. Voroshilov. *Polarised coherent Raman and saturation micro-Raman studies of biological macromolecules*. PhD thesis, University of Twente, 1997.

[27] C. Evans, E. Potma, M. Puoris'haag, D. Côte, C. P. Lin, and X. S. Xie. Chemical imaging of tissue in vivo with video-rate coherent anti-Stokes Raman scattering microscopy. *PNAS*, 102:16807–16812, 2005.

[28] Sigma-Aldrich Co. 2-propanol Raman spectrum, 2011.

[29] M. D. Ediger, R. S. Moog, S. G. Boxer, and M. D. Fayer. On the refractive index correction in luminescence spectrocopy. *Chem. Phys. Lett.*, 88:123–127, 1982.

[30] J. G. Skinner and W. G Nilsen. Absolute Raman scattering cross-section measurement of the 992 cm-1 line of benzene. *Journal of the Optical Society of America*, 58(1):113–119, 1968.

[31] J. P. Ogilvie, E. Beaurepaire, A. Aleandrou, and M. Joffre. Fourier-transform coherent anti-Stokes Raman scattering microscopy. *Optics Letters*, 31:480–482, 2006.

[32] K. Konig, T. W. Becker, P. Fischer, I. Riemann, and K. J. Halbhuber. Pulse-length dependence of cellular response to intense near-infrared laser pulses in multiphoton microscopes. *Optics Letters*, 24(2):113–115, Jan 1999.

[33] H. J. Koester, D. Baur, R. Uhl, and S. W. Hell. Ca^{2+} fluorescence imaging with pico- and femtosecond two-photon excitation: signal and photodamage. *Biophysical Journal*, 77:2226–2236, 1999.

[34] N. Dudovich, D. Oron, and Y. Silberberg. Single-pulse coherently controlled nonlinear Raman spectroscopy and microscopy. *Nature*, 418:512–514, 2002.

[35] D. L. Marks, C. Vinegoni, J. S. Bredfeldt, and S. A. Boppart. Interferometric differentiation between resonant and coherent anti-Stokes Raman scattering and nonresonant four-wave mixing processes. *Applied Physics Letters*, 85:5787–5789, 2004.

[36] T. W. Kee and M. T. Cicerone. Simple approach to one-laser, broadband coherent anti-Stokes Raman scattering microscopy. *Optics Letters*, 29:2701–2703, 2004.

[37] B. C. Chen and S. H. Lim. Optimal laser pulse shaping for interferometric multiplex coherent anti-Stokes Raman scattering microscopy. *Journal of Physical Chemistry B*, 112:3653–3661, 2008.

CHAPTER IV

Multiplexed Raman-induced Kerr Effect Microscopy

In this chapter, the experimental methods and setup used in obtaining Raman-induced Kerr Effect spectra and images are described in detail.

4.1 Introduction

The rapid growth of CARS as a modality for spectroscopy and microscopy brought with it the exploration of a number of other coherent Raman techniques, each with its own set of advantages and disadvantages. Coherent anti-stokes Raman ellipsometry (CARE) is a variation on the CARS technique designed to suppress the nonresonant background introduced in section 1.3 by virtue of careful polarization alignment. Nonresonant background is suppressed by linearly polarizing pump and probe fields at specific angles and analyzing the signal field at frequency ω_3 with another polarizer [1]. The primary advantages of this method are the retrieval of Lorentzian lineshapes free from interference with a nonresonant background as in CARS and the suppression of laser power fluctuations that cause a fluctuating background signal [2]. However, CARE is slightly more complicated to implement experimentally than CARS [3]. Another method of suppressing the electronic nonresonant background of

CARS was demonstrated by Kamga and Sceats in 1980 [4]. This technique, called Pulse-sequenced coherent anti-Stokes Raman scattering spectroscopy (PUSCARS), takes advantage of the different temporal responses of the nonresonant and resonant signal in CARS. By delaying the excitation pulses relative to each other (similar to the work presented in chapter III), one can reduce the nonresonant background significantly while preserving most of the resonant signal, narrowing the lineshapes of the detected signal to more closely match the spontaneous Raman spectrum. In microscopy, the time-delay approach has been used by a number of groups [5–7].

Another coherent technique to suppress noise related to the CARS nonresonant background was developed in 1976 by Song et al. [8]. This technique, called ASTERISK, uses three independent fields with frequencies ω_1, ω_2, and ω_3 polarized at specific orientations relative to each other. Careful polarization alignment can result in the cancellation of nonresonant background terms. This gives a pure Lorentzian lineshape without complications from nonresonant background. The disadvantage to ASTERISK is that the phase-matching condition must be maintained, preventing the use of a collinear geometry and thus making it unsuitable for microscopy applications.

One of the more promising coherent Raman techniques gaining popularity recently is stimulated Raman scattering (SRS). One of the most appealing aspects of stimulated Raman scattering for microscopy is that the phase-matching condition is automatically fulfilled, allowing collinear alignment of the excitation beams [9]. For this reason, SRS has been rapidly growing as a tool for microscopy [10–17]. Recently, Saar et al. demonstrated stimulated Raman scattering microscopy at video-rate [18]. SRS is performed using two collinear excitation beams as the pump and Stokes fields at frequencies ω_p and ω_S, respectively. If the frequency difference $\Delta\omega \equiv \omega_p - \omega_S$ is equal to a Raman active vibrational mode (Ω_{vib}) in the sample, the pump field will see an intensity loss and the Stokes field will see an intensity gain as a result of stimulated Raman scattering. To detect the small changes in intensity ($\delta I/I < 10^{-4}$)

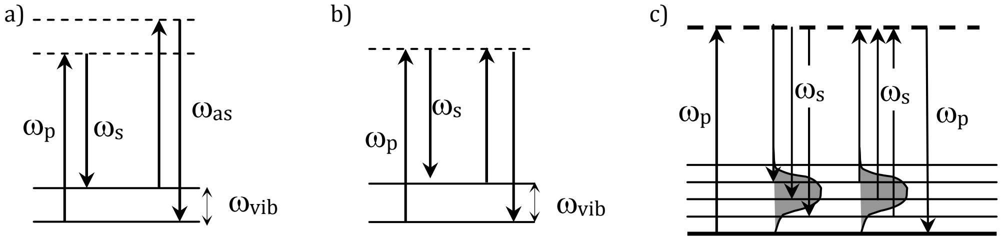

Figure 4.1: a)Energy level diagram for CARS, b)Energy level diagram for RIKES/SRS, and c) Energy level diagram for multiplex RIKES/FSRS.

in either the pump beam or the Stokes beam, a modulation scheme with lock-in detection is often needed. This allows effective imaging at high rates of speed for single mode microscopy. For multiplex microscopy, the implementation of this SRS scheme would require a lock-in CCD, with essentially a lock-in detector at every pixel on the CCD. In recent years, such detectors have become available [19], but they are not currently used for microscopy purposes. To date, only one experiment has demonstrated multiplex SRS [10], using a diode array for detection.

Recently, one more coherent Raman modality has been revisited for microscopy applications. The Raman-induced Kerr effect (RIKES) is a four-wave mixing process in which no new frequencies are generated. In this way, it is more analogous to SRS than CARS. An energy level diagram of all three processes is shown in Figure 4.1. In CARS (Fig. 4.1a), a new frequency is generated at ω_{as}, making it easy to spectrally isolate the signal from the excitation fields. In SRS (Fig. 4.1b), the Raman signal is generated at the same frequency as the excitation fields, so a modulation scheme must be implemented to extract the signal. RIKES (Fig. 4.1b), while sharing a similar energy level diagram, arises from anisotropic changes in the index of refraction of a medium upon interaction with the excitation fields. These interactions exhibit resonances when the frequency difference between the excitation fields matches a Raman active vibrational mode of the medium ($\omega_p - \omega_S = \omega_{vib}$), giving rise to an induced birefringence that can change the polarization state of the Stokes field ω_S. One particularly appealing aspect of RIKES is that it does not require lock-in detection to measure signal contrast, making multiplex detection extremely easy relative to stimulated Raman [20]. RIKES was recently demonstrated as a chemical contrast mechanism for microscopy [21]. This experiment was based on a lock-in technique capable of imaging only a single Raman mode. There is yet to be a demonstration of multiplex Raman-induced Kerr effect microscopy. This is the focus of the work presented in this chapter.

4.2 History

The Raman-induced Kerr effect was first demonstrated in 1976 by Levenson et al. as a coherent technique to recover the Raman spectrum of a sample with low background levels [22]. As described in section 1.3, a nonresonant background signal exists with CARS that spectrally overlaps the resonant signal of interest, decreasing chemical contrast unless background suppression techniques are used [3, 4, 8]. These techniques necessarily throw away some of the resonant signal as well, decreasing the total signal that can be detected and thus the sensitivity of the method. Because the Raman-induced Kerr effect is free of this nonresonant background, it is a particularly appealing technique to reproduce the spontaneous Raman spectrum of a material with high sensitivity.

Figure 4.2 shows the original experimental setup for Raman-induced Kerr effect spectroscopy by Levenson et al. [22]. It consists of a strong narrowband pump laser polarized linearly and then sent through a quarter wave plate to induce circular polarization. A broadband probe pulse is linearly polarized and is overlapped with the pump beam at the sample to provide the nonlinear interaction. A crossed polarizer after the sample (P3 in Fig. 4.2) suppresses the probe field, allowing the transmission of the RIKES field into the spectrometer and camera.

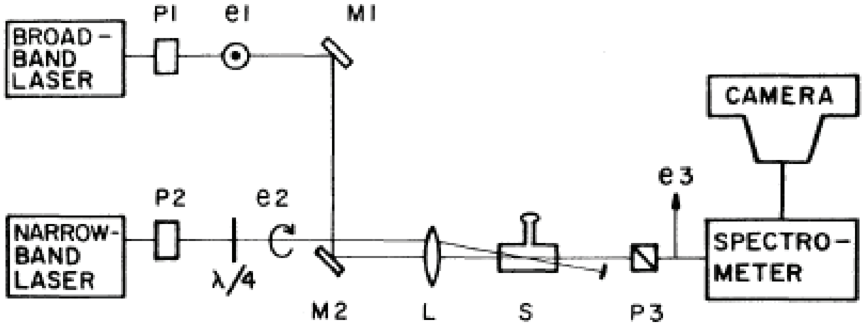

Figure 4.2: Experimental setup of the original Raman-induced Kerr effect spectroscopy experiment by Levenson. [22]

Recently, this technique has been expanded for use in microscopy by Freudiger, et al. [21]. Their setup utilizes a narrowband pump beam (1064 nm $Nd : YVO_4$) and narrowband Stokes beam (tunable optical parametric oscillator) to adjust the excitation frequency of the microscopy to a desired Raman vibrational mode. The Stokes beam is modulated with a home-built Pockels cell driven at 10 MHz to match the internal clock of a lock-in amplifier, providing fast imaging speeds. The beams are arranged in a collinear geometry into a laser scanning microscope. The Stokes beam is spectrally filtered out after the sample, and the probe beam is filtered out with a crossed polarizer. The signal is detected as a modulation transfer to the pump beam incident on a photodiode. While this experiment demonstrates RIKES microscopy at fast rates, it is limited by its ability to only image a single Raman band at once, making it less suitable for imaging samples with complicated Raman band structure or for imaging samples with unknown chemical composition.

4.3 Birefringent background

As discussed in section 2.4.1, the largest source of background in a Raman-induced Kerr Effect experiment is a birefringent background caused by the depolarization of the probe pulse. Because the suppression of the background probe field is dependent

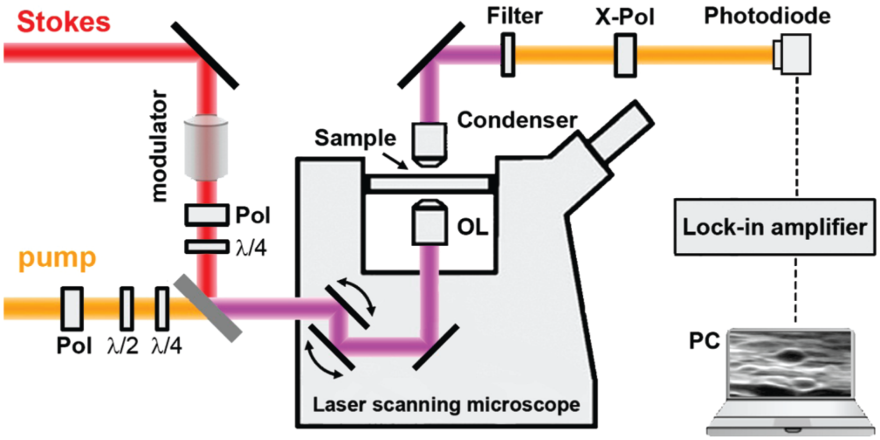

Figure 4.3: Experimental setup of single band Raman-induced Kerr effect microscopy by Freudiger, et al. [21]

on having nearly perfect linear polarization (to better than one part in 10^4), any birefringence in the optical path between the initial linear polarizer and the analyzer will give rise to unwanted background transmission at the same wavelength as the RIKES signal [2].

The total intensity on the detector I_D can be written as [23]:

$$I_D(\omega_2) = \frac{cn_2\epsilon_0}{2}\left|E_x(\omega_2) + E_B(\omega_2)\right|^2 = I_x(\omega_2) + I_B(\omega_2) \tag{4.1}$$

where $I_x(\omega_2)$ is the Raman-induced Kerr Effect signal intensity and $I_B(\omega_2)$ is the intensity of the birefringent background. Because the birefringent background field E_B is defined as spatially orthogonal to the Raman fields, cross terms of the type

$$2Re\left\{E_x(\omega_2)E_B^*(\omega_2)\right\} \tag{4.2}$$

do not exist. A discussion of this effect is given by Eesley [2], who explains it in the context of mode conversion. A small portion of the $TEM_{0,0}$ Gaussian probe field is converted to higher order Hermite-Gaussian modes due to the strain birefringence in the optics. Because the effective power of the cross-term given in Eqn. 4.2 is given by the integral over the active area A of the detector, the total detected power on the detector can be written as:

$$2Re\left\{E_x(\omega_2)E_B^*(\omega_2)\right\} \Rightarrow 2Re\left\{\int_A E_x(\omega_2,r,z)E_B^*(\omega_2,r,z)dA\right\} \tag{4.3}$$

Due to the orthogonality of Hermite polynomials, the cross-term contribution to the integral over the detector area is identically zero, resulting in no detected signal for interferometric terms. As a result, the birefringent background due to static strain in the intervening optics can be considered incoherent with the Raman signal.

It is important to note that unlike the nonresonant background of CARS, the birefringent background of RIKES is linearly dependent on the Stokes field intensity and independent of the pump field intensity. The electronic nonresonant background of CARS, on the other hand, is a four-wave mixing process that has quadratic power dependence on the pump and linear power dependence on the probe. As discussed in section 2.4.1, shot noise and classical noise on this birefringent background is ultimately the limiting source of noise for RIKES [2].

4.4 Experimental Setup

In RIKES, the phase matching condition is satisfied automatically, so our experiment is set up with completely collinear alignment [22]. Our experimental setup is shown in Fig. 4.4 [24]. The excitation source is a fiber laser provided by Ann Arbor, MI based IMRA, Inc. (FCPA μJewel D-400). It provides a pulse train of 2 μJ pulses at 200 kHz. The center wavelength is 1042 nm, and the pulse duration is < 350 fs. A beamsplitter is used to pick off 10% of the beam to seed a nonlinear photonic crystal fiber [25]. The continuum generated in the fiber is used as the broadband Stokes pulse. Its spectrum spans from the 1042 nm fundamental wavelength down to 750 nm, giving us more than 3000 cm^{-1} of available bandwidth for Raman excita-

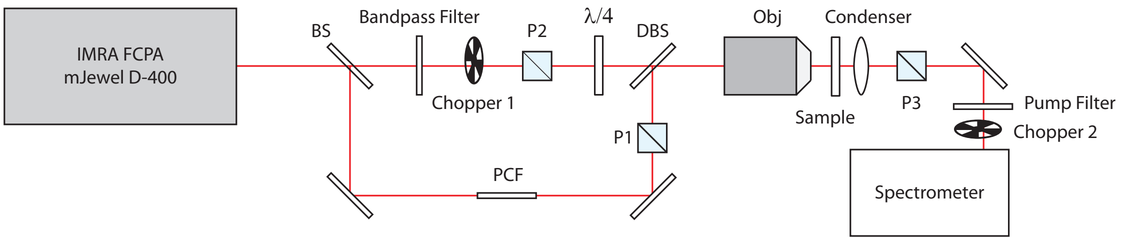

Figure 4.4: Experimental setup of our RIKES microscopy experiment. BS: 90/10 beamsplitter; PCF: photonic crystal fiber; P1: Glan polarizer 1; DBS: dichroic beamsplitter; P2: Glan polarizer 2; P3: Glan polarizer 3.

tion. Because there are few interesting Raman modes beyond ∼3000 cm^{-1}, no further bandwidth is required on the Stokes pulse. The maximum average power delivered by the photonic crystal fiber varied daily based on the condition of the fiber and precise alignment, but it generally stayed between 0.5 mW and 1.0 mW. This approach for broadband Stokes generation with a single laser has been previously used for multiplex CARS applications by Cicerone et al. [26]. The remaining 90% of the fiber laser output is spectrally narrowed using two narrow bandpass filters (CVI XLL-1064 nm) angle-tuned to provide ∼10 cm^{-1} pulses centered at 1042 nm. Both pump and Stokes beams are sent through high quality Glan polarizers (Precision Micro Optics PGLP-04302) with polarization purity $< 1 : 10^{-5}$ to achieve a high degree of linear polarization in each of them. The pump beam is then sent through a quarter wave plate (CVI QWPO-1047-05-4-R10) to provide circular polarization.

Polarization purity proved to be a major problem due to the substantial degree of strain birefringence in most optics. A standard air objective (NA 0.4, Olympus LM plan IR, 20×) was initially used to focus the beam onto the sample, but the depolarization of the linear probe proved to be extremely large. The best polarization purity achievable with this objective was $1 : 300$, which is substantially worse than the $1 : 10^4$ required for a birefringent background low enough to perform RIKES. After replacing the standard air objective with a high polarization purity objective

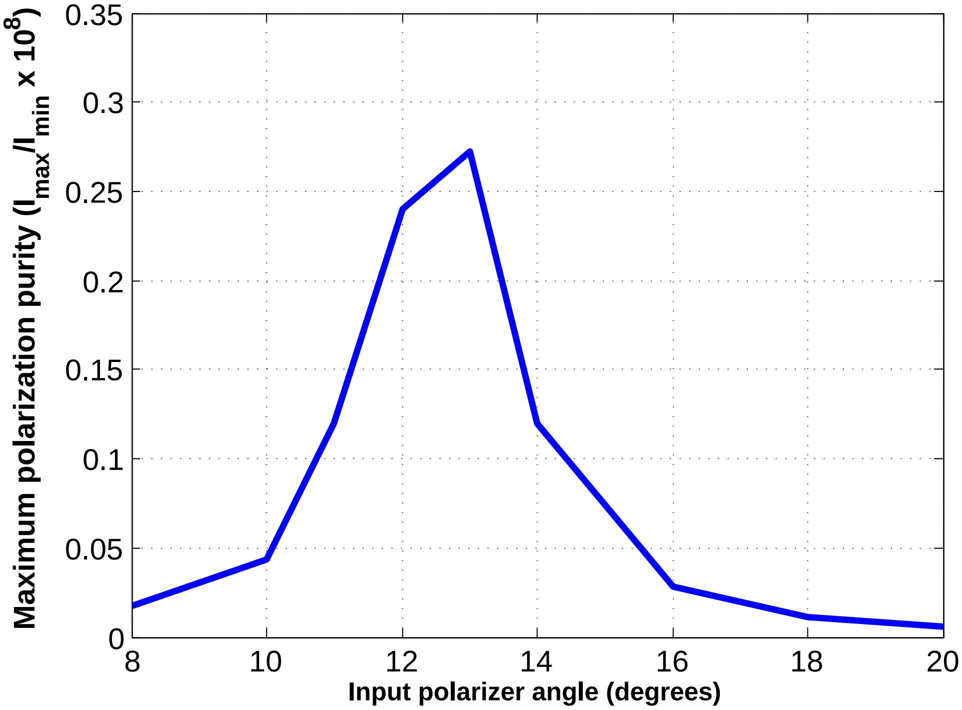

Figure 4.5: Polarization purity of beamsplitter as a function of linear polarization orientation of Stokes beam. As the orientation moves away from perfect p-polarization (13°), the polarization purity drops rapidly.

(NA 0.5, Olympus UPLFLN20XP, 20×), the polarization purity improved drastically to $\sim 1:10^{-5}$. Additionally, the recombining dichroic beamsplitter (DBS in Fig. 4.4) proved to significantly alter the polarization purity of the Stokes beam based on the precise polarization state upon incidence. As shown in Figure 4.5, if the Stokes beam was not perfectly p-polarized, the beamsplitter caused considerable depolarization of the linear probe, resulting in transmission through the analyzer. The depolarization effects of both the standard air objective and imperfect alignment onto the dichroic beamsplitter were enough to saturate the detector. Once all depolarization effects are accounted for and corrected, the total polarization purity of the imaging system is better than $1:10^{-4}$, which is suitable for performing RIKES.

After the pump and Stokes beams are recombined collinearly at the dichroic beamsplitter, they are focused onto the sample by the aforementioned high polarization purity objective. The sample is mounted on an x-y scanning piezo stage (PI P612.2SL) with a total scan range of $100\mu m \times 100\mu m$, which is raster-scanned to form images. The signal is then collected in a transmission geometry and collected by a condenser (NA 0.8) where it is collimated and analyzed by another high quality Glan polarizer (P3 in Fig. 4.4). The signal is then directed into a spectrometer (Jobin Yvon IHR320) and detected on a CCD (Pixis 100F) at 1 kHz. The chopping scheme seen in Fig. 4.4 was later implemented, for reasons discussed in section 4.5.1. Because the quantum efficiency of the Pixis 100F CCD peaks at ~700 nm with a FWHM bandwidth of ~350 nm, spectra are detected on the anti-Stokes side of the fundamental wavelength of 1042 nm. Detection of 3000 cm^{-1} Raman modes thus occurs near 800 nm, where the quantum efficiency of the CCD is ~0.4, rather than near 1500 nm, where the quantum efficiency drops to 0.

This experimental setup is extremely useful because of the ease with which we can switch between performing multiplex Raman-induced Kerr effect imaging and multiplex stimulated Raman scattering imaging. To switch between the two imaging modalities, the quarter wave plate in the pump arm is rotated such that the optical axis is aligned with the linear polarization axis of the incident pump beam, resulting in no change in the polarization state of the pump after the initial Glan polarizer. Then, the analyzer (P3) is simply removed and replaced with a neutral density filter to avoid detector saturation, and the rest of the setup is left untouched. This allows us to image the same spot on the sample with both RIKES and SRS in succession with no disturbance to the sample, making direct comparison of the two methods straightforward.

4.5 Experimental Results

4.5.1 RIKES Spectroscopy

To demonstrate Raman-induced Kerr effect as a spectroscopy tool, we first performed studies in solution. Because of its Raman signal strength, we start out taking spectra of carbon disulfide (CS_2). Carbon disulfide has an extremely strong Raman peak near 670 cm^{-1}, corresponding to the symmetric stretching vibration of the molecule. A solution of pure carbon disulfide is prepared in a quartz cuvette (1 mm path length) and placed at the focus of the excitation beams. For spectroscopy experiments on CS_2, a Corning Hi980 photonic crystal fiber is used to generate the continuum. We started with this fiber because it provides the highest spectral power density for the sample of interest. The 670 cm^{-1} Raman mode of carbon disulfide puts the signal wavelength at 975 nm, close to the spectral peak of the continuum probe. The full spectrum of the continuum with 40 mW input power is shown in Figure 4.6. The output of the fiber was directed into the spectrometer with a neutral density filter (optical density 6) placed in the beam to prevent detector saturation. Because the maximum bandwidth available for detection is limited by the spectrometer grating to be 50 nm, the grating must be rotated for every 50 nm increment in wavelength. As a result, Figure 4.6 shows spectral discontinuities at increments of 50 nm due to small temporal variations in the continuum spectrum.

Figure 4.7 shows the Raman-induced Kerr effect spectrum of carbon disulfide measured in our experiment. 23.7 mW is used for the circularly-polarized pump field, and 0.7 mW is used for the linearly-polarized continuum. The small secondary peak on the low-frequency side of the primary peak at 670 cm^{-1} can be explained by the structure of the strong pump beam, which has a small secondary peak. This small secondary peak was later spectrally filtered out by slight angle tuning of the bandpass filter shown in Figure 4.4.

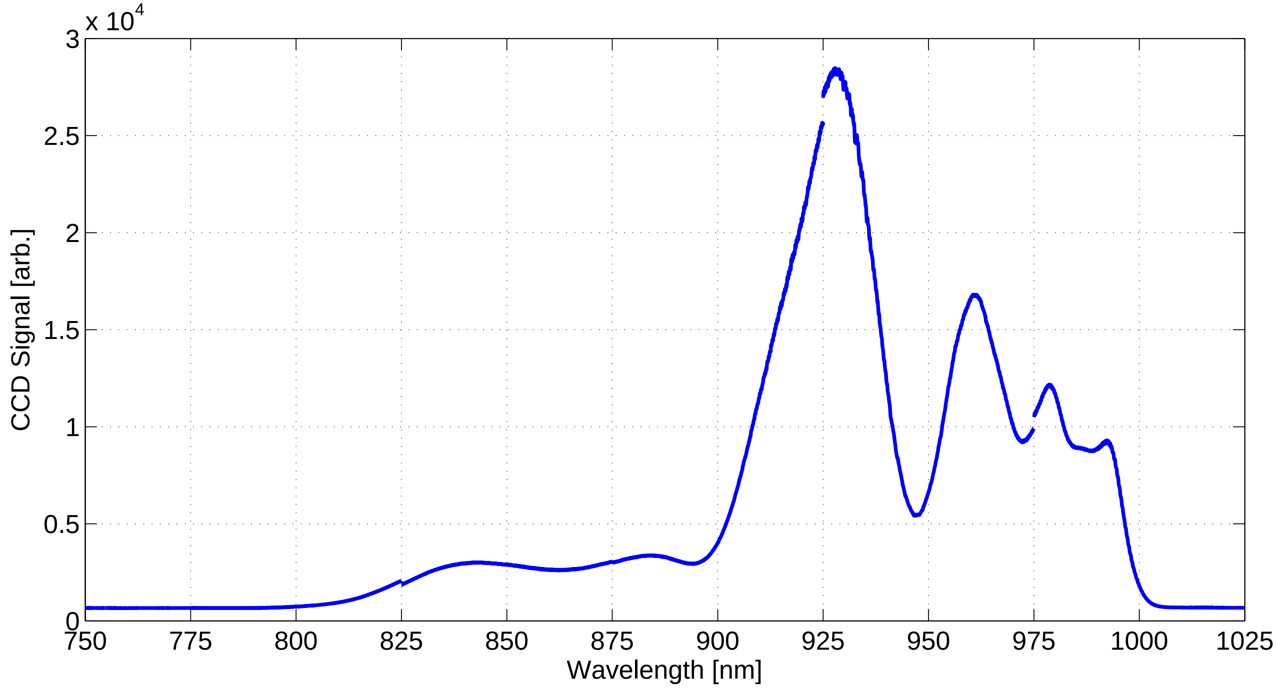

Figure 4.6: Spectrum of continuum generated with Corning Hi980 fiber. Discontinuities originate from rotation of the spectrometer grating.

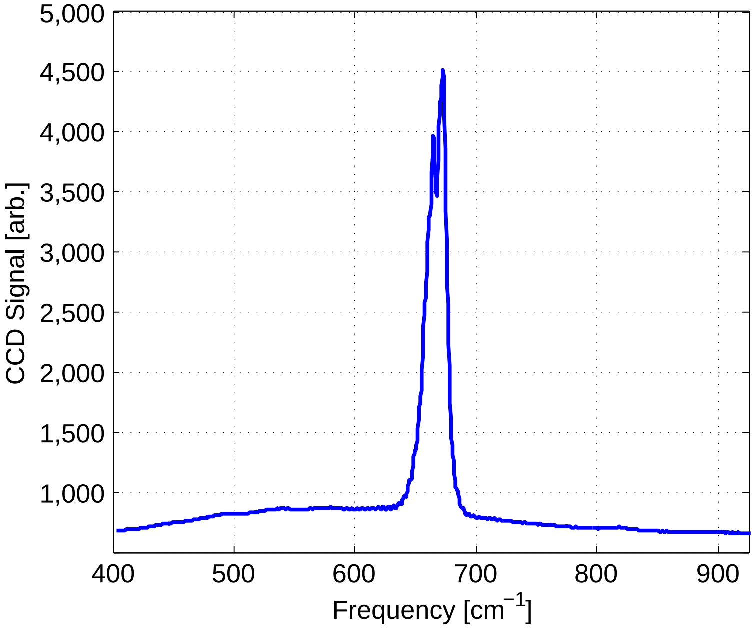

Figure 4.7: Raman-induced Kerr effect spectrum of carbon disulfide. Excitation conditions are 23.7 mW pump and 0.7 mW probe power, with 1 ms integration time. Shown is the average of 2000 spectra. CS_2 Raman peak appears at 670 cm^{-1}.

Using the straightforward method of switching between RIKES and FSRS described in section 4.4, we also compared the relative signal strengths of RIKES and FSRS for spectroscopy. To take FSRS data, we took consecutive spectra with the pump off and on, with the difference between the two providing the measured spectrum. Shown in Figure 4.8, FSRS spectra are much noisier than RIKES spectra, with lower signal strength. Fig. 4.8a and 4.8b show the relative signal strengths at 10 mW input power. At this excitation power, FSRS provides only 10-20 CCD counts of signal, whereas RIKES produces a much larger signal ($\sim$3000 counts). The slowly varying envelopes of the FSRS spectra are due to small changes in the spectral shape of the continuum between the pump on and pump off spectra. Also, it is important to point out the nonzero spectral baseline of the RIKES spectrum, which is caused by the existence of the birefringent background discussed in section 4.3. Spectra taken at 0.5 mW of pump power (Fig. 4.8c and 4.8d) show similar results, with the FSRS signal nearly indistinguishable above background and RIKES performing significantly better with signal levels several times above the background level.

For biological samples, most Raman imaging is performed near 3000 cm^{-1} because of the abundance of C-H stretches in biological samples [27–31]. A frequency difference of 3000 cm^{-1} on the anti-Stokes (blue) side of our 1042 nm pump pulse puts the required probe wavelength at 794 nm. The spectral power density of our current probe (Fig. 4.6), however, is essentially zero near 800 nm. To reach higher frequency Raman modes near 3000 cm^{-1}, we replaced the Corning Hi980 fiber with a broadband photonic crystal fiber described by Fu et al. [25]. The relevant portion of the continuum generated with this fiber is shown in Figure 4.9. The maximum spectrally integrated average power in this fiber is significantly lower than the Corning fiber ($\sim$0.2 mW and $\sim$1.2 mW, respectively), but the spectra power density is much higher at the wavelengths relevant for 3000 cm^{-1} detection. The spectral power density in this case peaks around 800 nm and is very high over the full wavelength

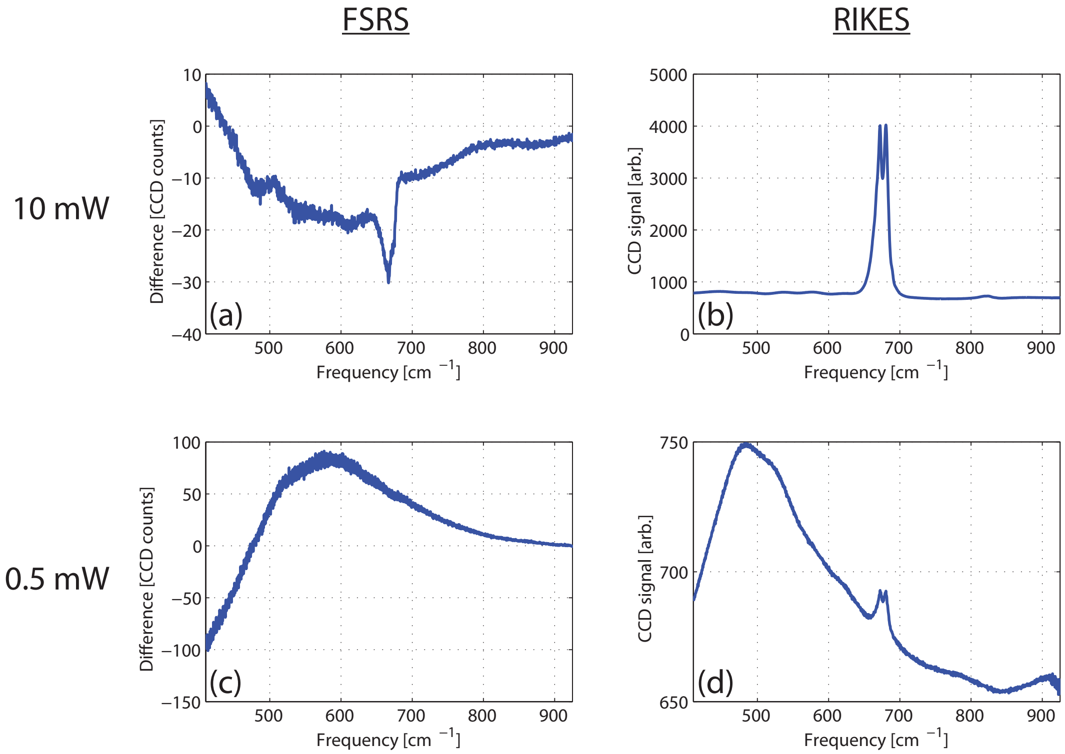

Figure 4.8: FSRS versus RIKES for CS_2. Spectra taken with 1.1 mW probe power with 1 ms exposure. Pump power is indicated at left. Shown in each panel is the average of 2000 spectra. Raman peaks for CS_2 appear at 670 cm^{-1}.

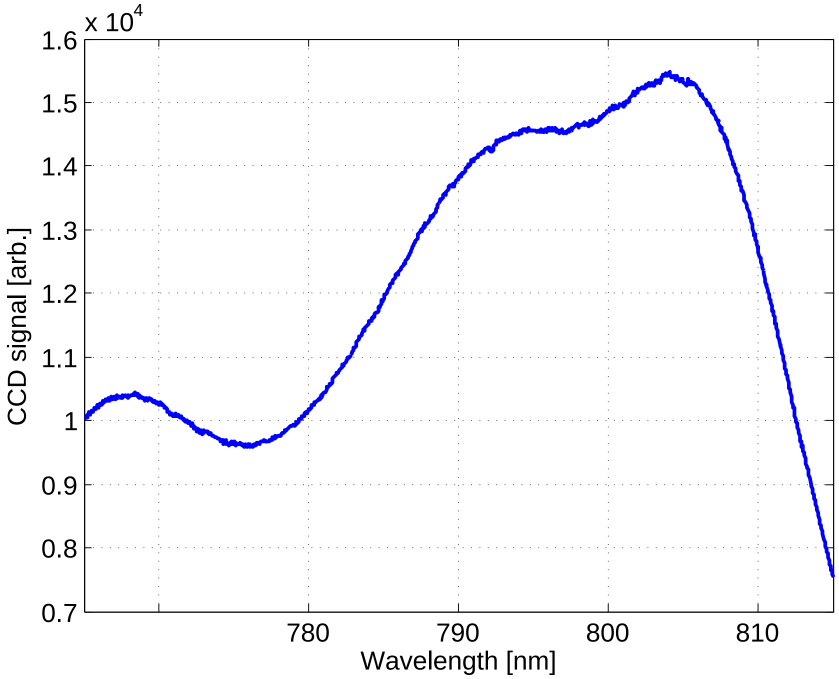

Figure 4.9: Spectrum of continuum generated with broadband fiber [25]. Primary Raman vibrational modes of interest are probed between 785 nm and 805 nm.

range of interest.

To test our ability to detect higher frequency Raman modes near 3000 cm^{-1}, we performed a similar study on solutions of toluene. The spontaneous Raman spectrum of toluene is shown in Figure 4.10 [32]. Shown in Figure 4.11 is our comparison of FSRS and RIKES signal strengths at different excitation power levels for toluene. Toluene has two strong Raman modes near 3000 cm^{-1}, one at 2920 cm^{-1} and the other at 3040 cm^{-1}, corresponding to the methyl symmetric stretch ($CH_3 - SS$) and the aromatic C-H stretching mode, respectively [33]. At 10 mW, the Raman-induced Kerr effect spectrum (Fig. 4.11b) is much cleaner with a higher signal to noise level than the corresponding stimulated Raman spectrum (Fig. 4.11a). Total counts above background are ~20 for FSRS and ~1000 for RIKES. When the excitation power is cut in half (Figures 4.11c and 4.11d), the stimulated Raman signal is nearly indistinguishable from the background. RIKES, however, still shows two distinct peaks at 2920 cm^{-1} and 3040 cm^{-1}.

While the Raman-induced Kerr effect spectra look much better with higher signal to noise than FSRS spectra, there is still a bothersome birefringent background that appears in all of the RIKES spectra. This background makes it difficult to quantify signal levels and determine lineshapes from the measured spectra. To help eliminate the effect of birefringent background on our spectra, we take advantage of the fact that it is caused by only leakage of the probe light and is independent of the pump. The RIKES signal, however, disappears if either beam is blocked. Accordingly, we can remove the birefringent background by applying a chopping scheme to the pump pulse. When the pump pulse is blocked, only the birefringent background remains. When the pump pulse is on, the RIKES signal + birefringent background is measured on the detector. The difference between these two reproduces the RIKES spectrum with minimal contributions from birefringent background.

As shown in Figure 4.4, the chopper (chopper 1) is placed in the pump beam between the bandpass filter and Glan polarizer. Because the chopping is performed at 100 Hz, changes in the probe continuum spectrum are minimal, and the birefringent background is nearly completely removed. Figure 4.12 shows the effectiveness of the scheme. Figure 4.12a shows the RIKES spectrum of toluene without chopping. The birefringent background can be seen to be very large on the low frequency end of the spectrum, and still nearly equal in magnitude to the RIKES signal itself near 3000 cm^{-1}. When the chopping scheme is applied (Figure 4.12b), the difference is clear. The birefringent background nearly disappears entirely and the Raman lineshapes are much cleaner and more closely represent the spontaneous Raman spectrum. Additionally, a second chopper (chopper 2 in Fig. 4.4) is placed immediately before the spectrometer to block the CCD during readout to prevent spurious signal.

The spectroscopic studies performed in solution show that Raman-induced Kerr

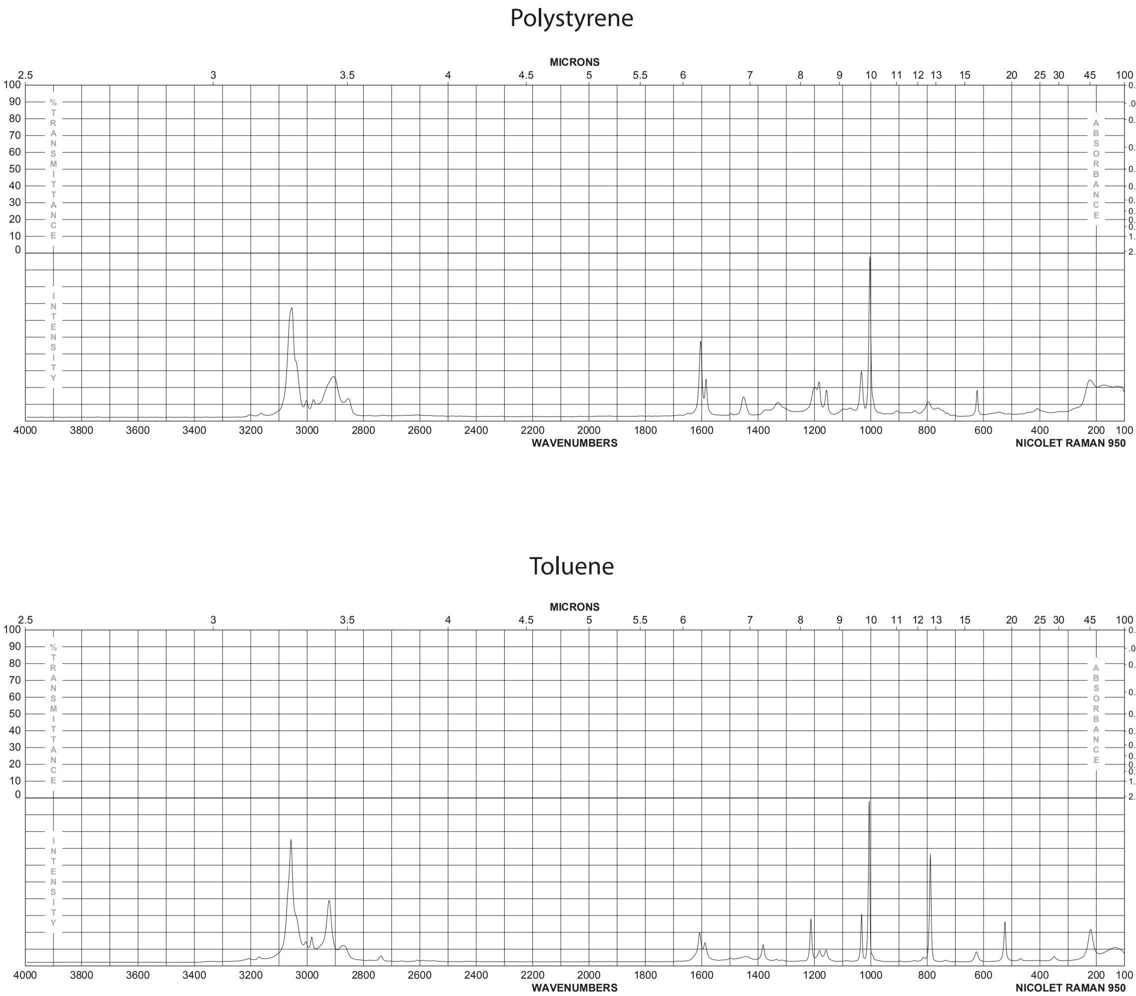

Figure 4.10: Spontaneous Raman spectra for polystyrene and toluene [32, 34].

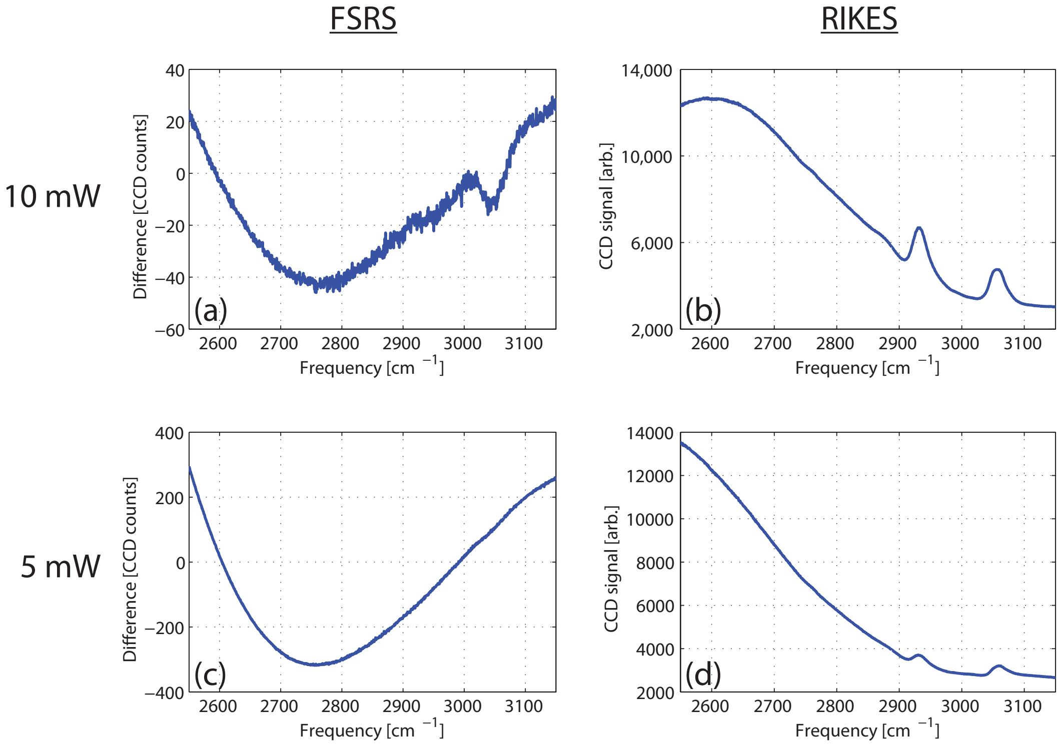

Figure 4.11: FSRS versus RIKES for toluene. Spectra taken with 0.17 mW probe power, with 10 ms exposure. Pump power is indicated at left. Shown in each panel is the average of 2000 spectra. Raman peaks for toluene appear at 2920 cm^{-1} and 3040 cm^{-1}

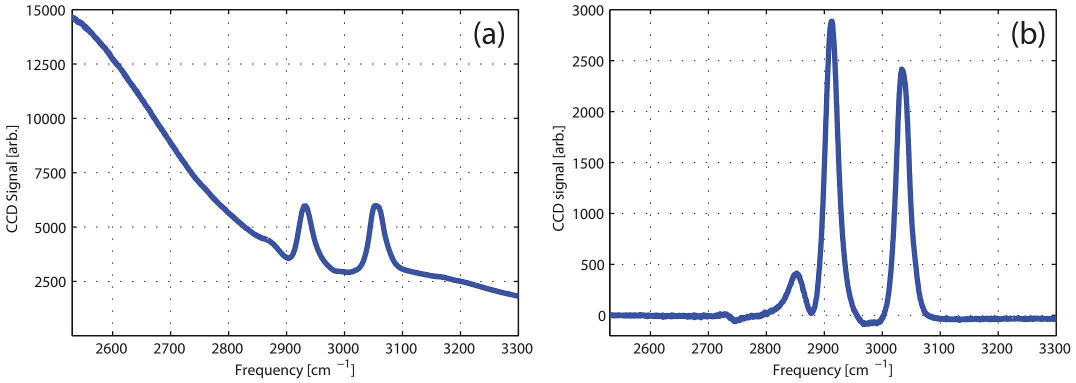

Figure 4.12: a) Unchopped versus b) chopped spectra of toluene. Both spectra taken with 15 mW pump excitation and 0.1 mW probe excitation.

effect spectroscopy produces higher signal to noise spectra than femtosecond stimulated Raman spectroscopy under the same excitation conditions. The addition of a chopping scheme improves the RIKES spectra dramatically by removing the birefringent background that plagues RIKES spectra. The next section will show that this setup is particularly suitable for Raman microscopy applications.

4.5.2 RIKES Microscopy

To demonstrate imaging using the Raman-induced Kerr effect, we replaced the cuvette of solution with an x-y piezo stage (position labeled "sample" in Figure 4.4) to raster scan solid samples. We first attempt imaging in the absence of a chopping scheme to judge our performance. Using the Corning Hi980 fiber, we perform imaging of 10 μm diameter polystyrene beads in Cytoseal-60 (Richard-Allan Scientific), a toluene-based sealant. The toluene-based sealant is used to minimize the index of refraction change between the polystyrene beads and surrounding medium to reduce scatter. The spontaneous Raman spectra of polystyrene and toluene are shown in Figure 4.10 [32, 34]. Figure 4.13 shows a $90\mu m \times 90\mu m$ image of polystyrene beads in toluene sealant. The intensity at 800 cm^{-1} (Fig. 4.13a) should trace out the toluene concentration, as toluene has a strong 800 cm^{-1} peak, while polystyrene has no peak at 800 cm^{-1}. As expected, the 800 cm^{-1} signal is lowest in the beads, while it is much higher in the surrounding toluene sealant. Because both polystyrene and toluene have strong peaks at 1000 cm^{-1}, they look similar in intensity in images taken at this frequency (Fig. 4.13b). Using the ratio of the two peaks as a mode of chemical contrast, Fig. 4.13c shows polystyrene beads with distinct contrast from the surrounding toluene. However, the nonuniform features of the beads in all images hint that the chemical contrast may not be genuine when observing only the intensity at the Raman peak wavelengths. Indeed, as seen in Figure 4.13d, the birefringent background jumps significantly when the beam focus passes over polystyrene beads,

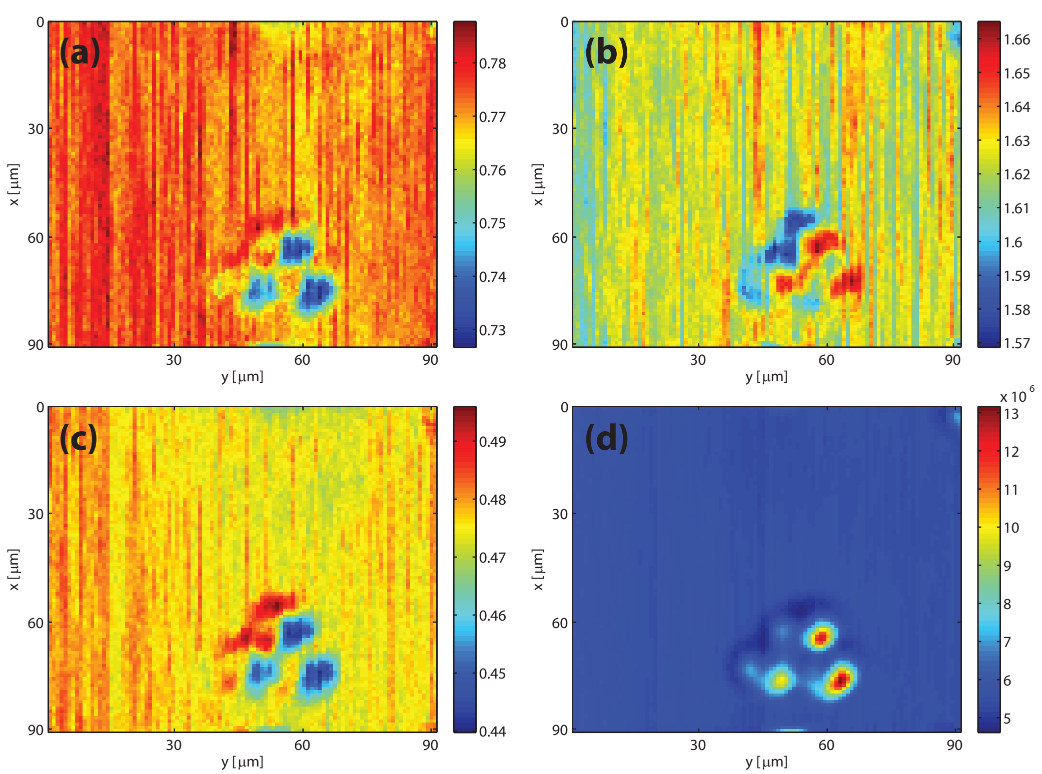

Figure 4.13: RIKES imaging of 10 μm polystyrene beads without chopping scheme as a function of frequency. a) 800 cm^{-1}, b) 1000 cm^{-1}, c) Ratio of 800 cm^{-1}, d) Integrated birefringent background intensity.

indicating that the intensities seen in Fig. 4.13a-c may be mapping out the intensity changes of the birefringent background at Raman peak wavelengths, rather than the intensity of the Raman peaks themselves. This is caused by the increased scattering of the probe beam at the interface of the polystyrene beads, resulting in increased depolarization of the probe and consequently a jump in birefringent background intensity. From this, we concluded imaging without chopping is not feasible, as it leads to spurious signal due to changes in birefringent background over the course of a sample scan.

To counteract this, we added the chopping scheme previously used for solution studies (section 4.5.1). For imaging, the implementation of the scheme is straightforward. For every pixel, rather than taking a single spectrum, we take two spectra –

one with the pump on and the other with the pump blocked. The difference between the two spectra provide spectra free of birefringent background, similar to Fig. 4.12b. Figure 4.14 shows the effect of chopping the pump for imaging. For these images, we switch back to the broadband photonic crystal fiber for imaging near 3000 cm^{-1} [25]. Fig. 4.14a shows a $30\mu m \times 30\mu m$ image of $10\mu m$ diameter polystyrene beads in toluene sealant taken without chopping. Similar to Fig. 4.13, there are clear artifacts (dark rings) at the edges of the beads and reduced overall contrast due to probe scattering and resulting depolarization. After the chopping scheme is implemented (Fig. 4.14b), the image contrast is improved drastically, and the artifacts near the edges disappear completely. The effect of chopping on the individual spectra themselves is shown in Figure 4.14c. Shown in green is the raw data inside a polystyrene bead (42 pixels are averaged for clarity). The birefringent background corresponding to the same pixels is plotted in black. In red is the resulting spectrum after removal of the birefringent background. The corresponding toluene chopped spectrum is plotted in blue. With the subtraction of the birefringent background, contrast between the two Raman peaks at 3040 cm^{-1} and 2920 cm^{-1} is not lost.

To test the effect of pump power on RIKES imaging contrast, we took images of the sample from Fig. 4.14 at several different levels of excitation power. Figures 4.15a-f show the loss of contrast in RIKES imaging as pump power is lowered from 12 mW to 2 mW in increments of 2 mW per image. Because the image contrast is given by the intensity ratio of 3040 cm^{-1}/2920 cm^{-1} peaks, rather than lower overall intensity, the degradation occurs in signal to noise ratio. At pump excitation of 2 mW, polystyrene beads are difficult to distinguish above the noise.

The imaging scheme with chopping was next used to do a comparison of imaging performance between femtosecond stimulated Raman spectoscopy and Raman-induced Kerr effect spectroscopy. Figure 4.16 shows a comparison of FSRS and RIKES imaging for 10 μm diameter polystyrene beads. Figures 4.16a and b show images of

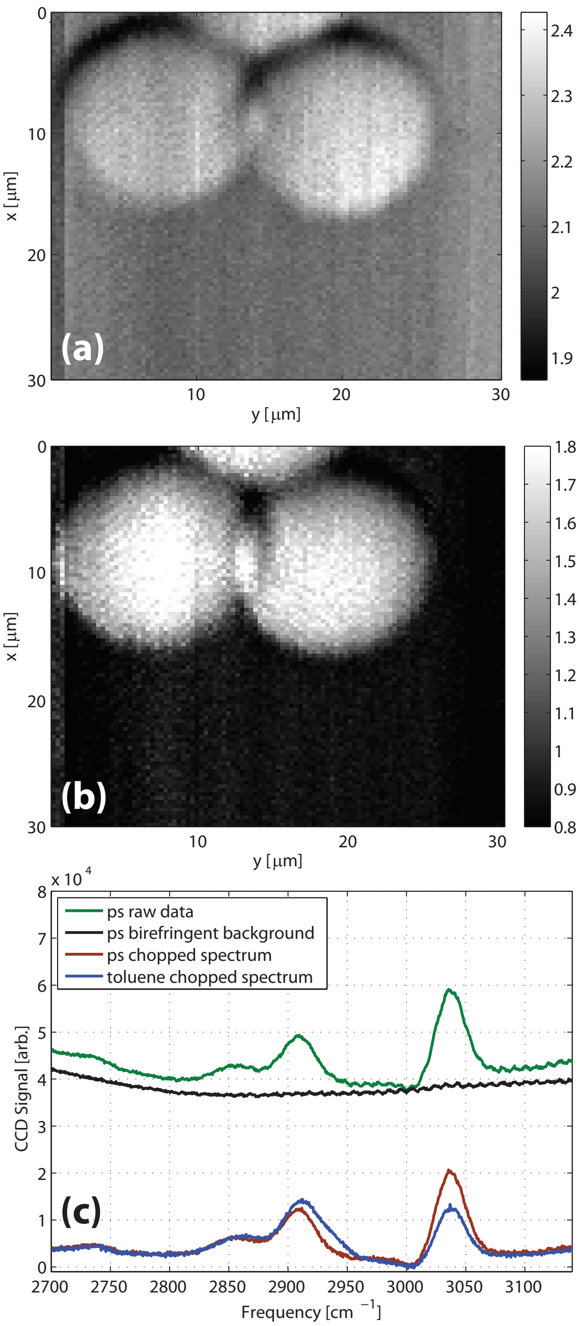

Figure 4.14: RIKES imaging of 10 μm diameter polystyrene beads a) with and b) without chopping scheme. Plotted is the intensity ratio of 3040 cm^{-1} to 2920 cm^{-1} peaks. c) Average of 42 spectra taken inside polystyrene beads and toluene sealant. Raw data, birefringent background, and chopped spectrum for polystyrene is shown, along with the chopped spectrum in toluene sealant. Excitation conditions are 12 mW pump and 0.05 mW probe power.

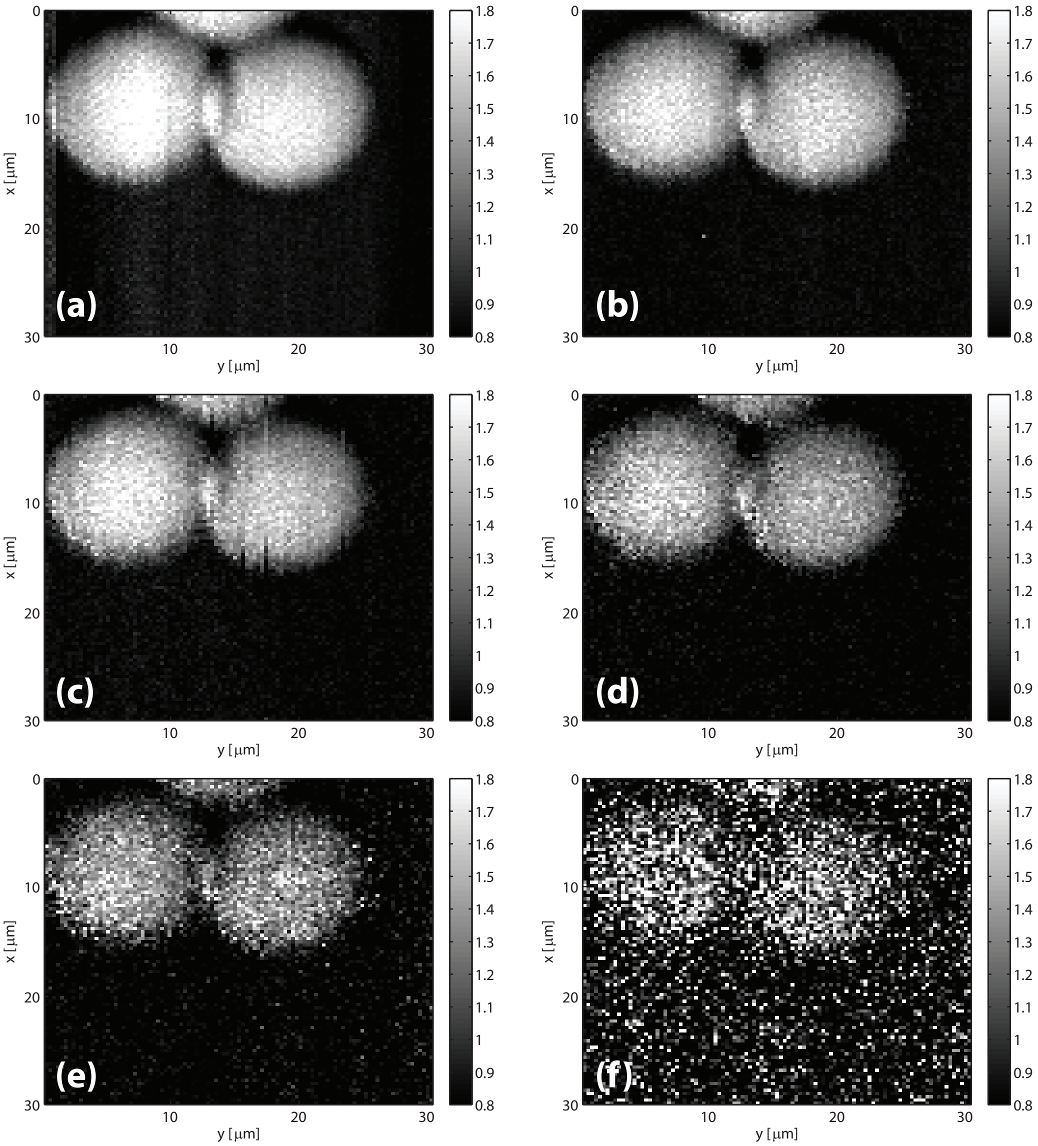

Figure 4.15: RIKES imaging of 10 μm diameter polystyrene beads in cytoseal as a function of excitation power. Plotted is the intensity ratio of 3040 cm^{-1} to 2920 cm^{-1} peaks. Pump power levels of a) 12 mW, b) 10 mW, c) 8 mW, d) 6 mW, e) 4 mW, and f) 2 mW are used. All images taken with 0.05 mW probe power. Image contrast decreases as pump excitation power decreases.

the beads in toluene sealant at 2920 cm^{-1}. Because polystyrene and toluene have similar signal strengths at this Raman mode, contrast is low in FSRS. In RIKES, signal strength is similar in the center of the beads to the surrounding toluene sealant. At the edges of the beads, there is a sharp drop in signal that provides contrast and may be attributed to scattering causing less overall light into the detector. This effect is consistent at all frequencies and cancels out when looking at peak ratios (Fig. 4.16f). Figures 4.16c and d show the same images at 3040 cm^{-1}. The signal strength of polystyrene is larger than that of toluene at this Raman mode, giving the images chemical contrast. However, the FSRS image (Fig. 4.16a) shows much less contrast due to a lower signal to noise ratio than RIKES (Fig. 4.16d). The ratio of the two Raman mode strengths gives the best polystyrene/toluene chemical contrast and is shown using each technique in Figures 4.16e and f. Here, the contrast is low with high noise in FSRS, while RIKES produces beautiful images with high contrast. The higher signal to noise ratio of RIKES relative to FSRS is shown clearly when looking at the full spectra of the two chemical species (Figures 4.16g and h). For clarity, 42 spectra are averaged for each technique. FSRS shows significantly lower signal to noise given equal excitation conditions, showing the advantages RIKES can offer in both spectroscopy and microscopy applications.

To demonstrate RIKES microscopy on biological samples, we took images of onion cells affixed to a glass coverslide. Figure 4.17 shows images of onion cells on- and off-resonance. Fig. 4.17a shows an off-resonance image taken at 2750 cm^{-1}. There is no visible contrast in the image due to the lack of Raman active modes in the sample. Fig. 4.17b shows an image taken at 2940 cm^{-1}, on-resonance with antisymmetric CH_2 stretching modes in the onion cell cytoplasm [35]. Structure is clear in the on-resonance image, despite onion cells generally being larger than the available $90\mu m \times 90\mu m$ scanning range. Green areas of large signal map out the distribution of cytoplasm within the cell. Figure 4.17c shows the average of 42 spectra taken within

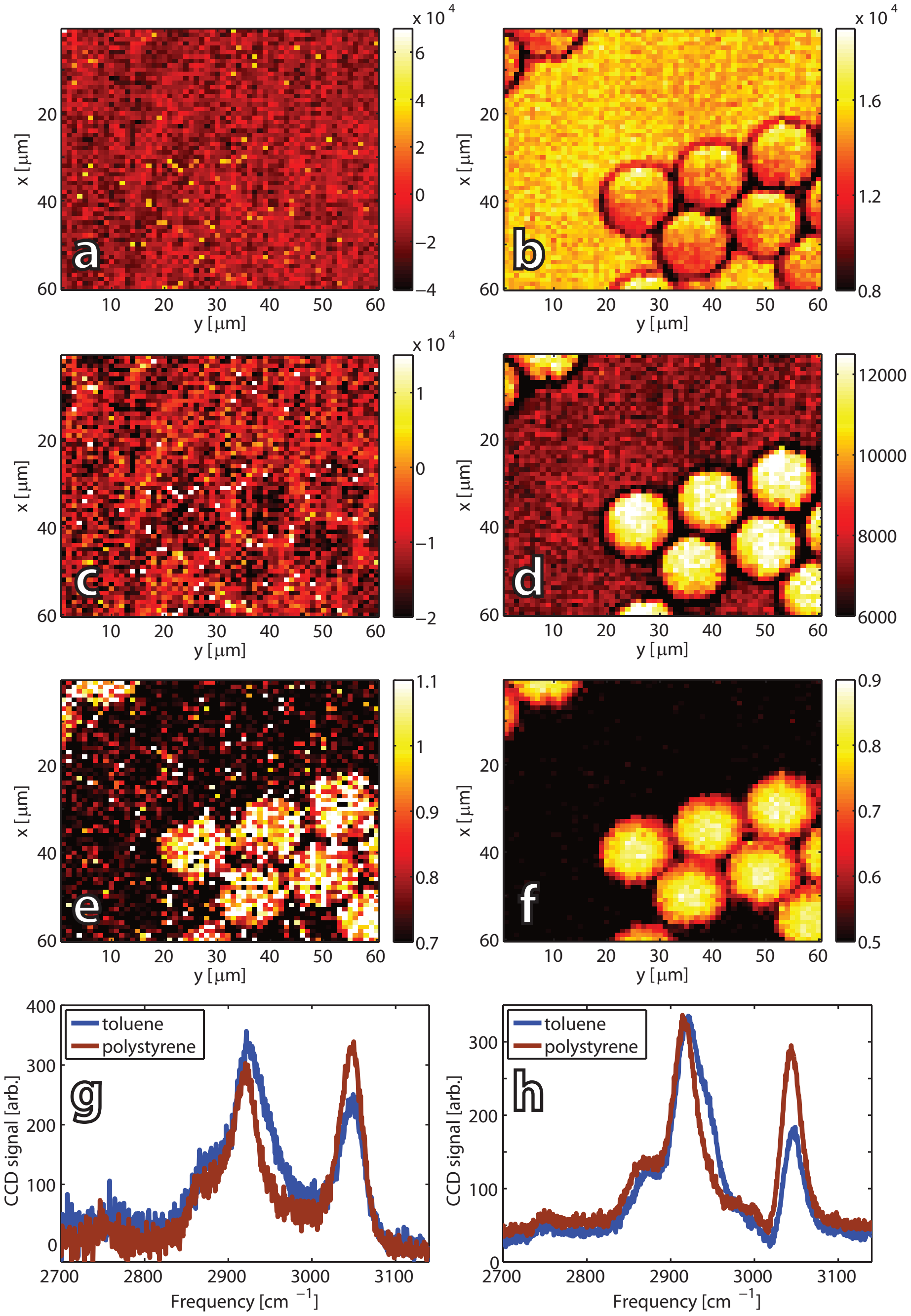

Figure 4.16: FSRS versus RIKES imaging of polystyrene beads. a,b) Images at 2920 cm^{-1}. c,d) Images at 3040 cm^{-1}. e,f) Images of 3040 cm^{-1}/2920 cm^{-1} peak ratio. g,h) Average of 42 spectra taken in polystyrene beads and toluene with FSRS and RIKES, respectively. Excitation conditions are 12 mW pump and 0.05 mW Stokes power, and all scans are $60\mu m \times 60\mu m$.

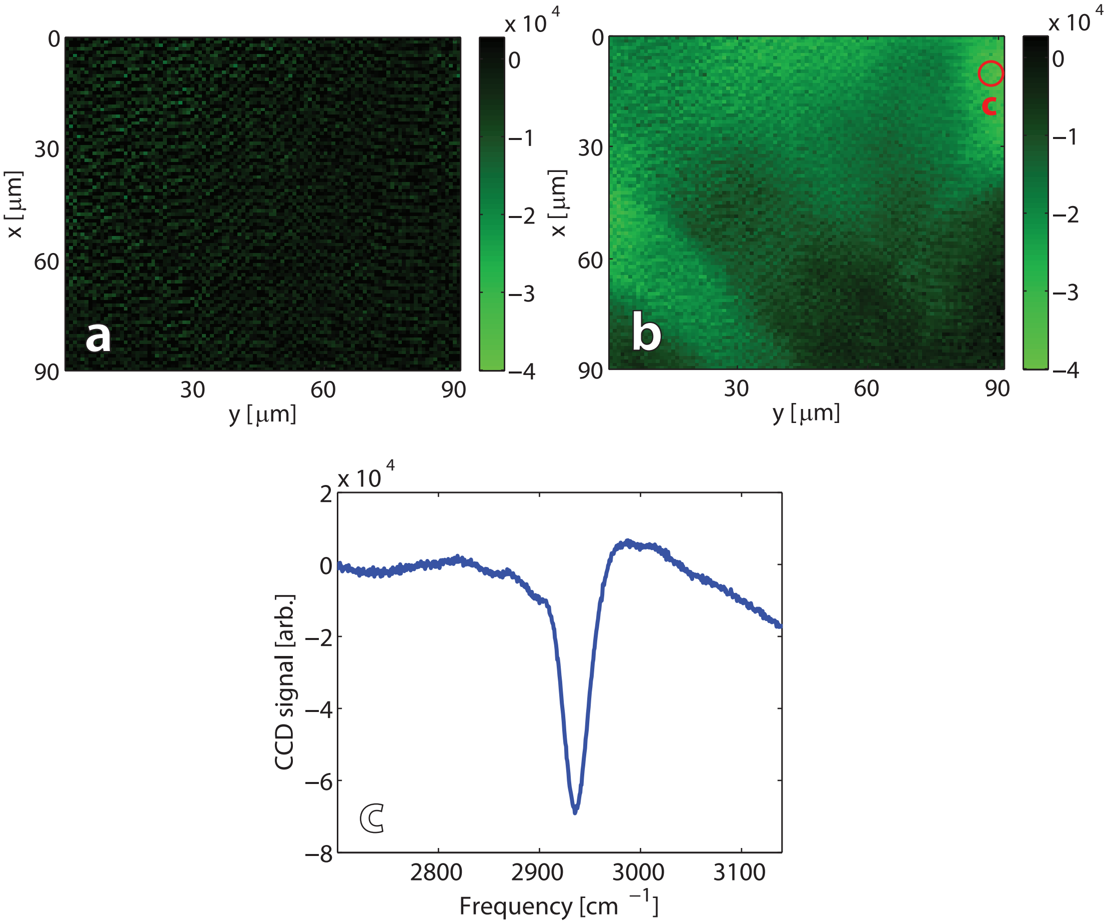

Figure 4.17: Raman-induced Kerr effect images of onion cells. Images taken at a) 2750 cm^{-1} (off-resonance) and b) 2940 cm^{-1} (on-resonance). c) Average of 42 Raman spectra taken from circle indicated in (b).

the red circle indicated in (b). These spectra show a large Lorentzian peak centered at $\sim$ 2940 cm^{-1} with a very high signal to noise ratio.

Figure 4.18 shows an unexpected effect that arose during the imaging of onion samples. Over the course of a scan, the signal peak (i.e. Raman spectrum in Fig. 4.17c) significantly changes shape and even flips sign. An instance of this effect is shown in Figure 4.18a. In the top right corner of the image, the cell wall cuts through the image along the diagonal. Figures 4.18b and c show the single pixel spectra associated with the circles shown in (a). At different areas near the cell wall, the RIKES peak changes magnitude and flips sign. This sign-flipping behavior can be

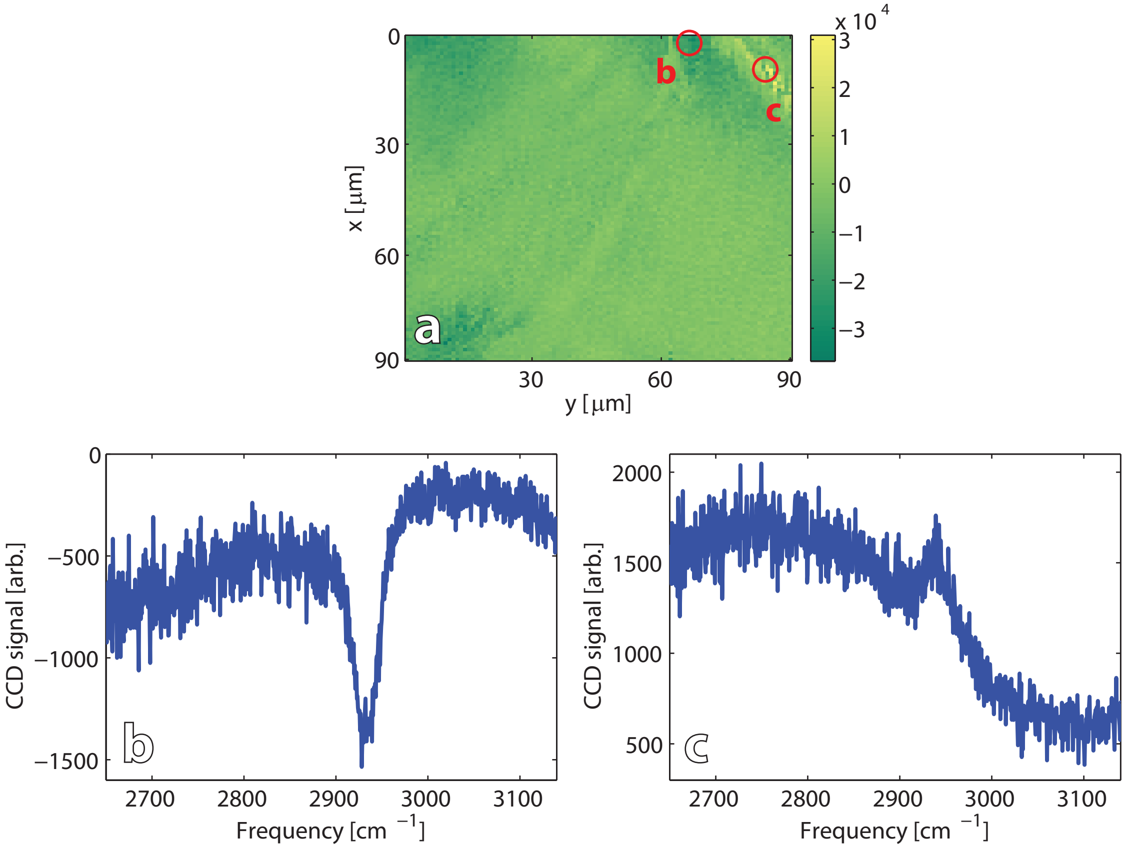

Figure 4.18: Sign flipping phenomenon in RIKES onion images.

attributed to spatial variations in birefringence over the cell scan, and particularly near the cell membrane. As shown by Shin et al. [36], the birefringence of an onion cell is known to vary significantly between the cytoplasm and membrane. The difference in birefringence between the cell membrane and cytoplasm is largest immediately after samples are prepared and declines over a timescale of ∼30 hours. All of the samples shown in this work were imaged within one hour of sample preparation, lending to large birefringence effects near the cell wall.

As a result of the varying birefringence over the scan area, the pump and probe pulses fail to maintain their precise polarization state. Polarization ellipticities in the probe pulse manifest themselves as contributions to the birefringent background discussed in section 4.3. Polarization changes in the pump, however, have a strong effect on the lineshape of the signal. The effect of an arbitrary elliptical pump polarization on the lineshape and magnitude of the RIKES signal is discussed by Levenson and Song [37]. RIKES with perfectly circular pump polarization give rise to Lorentzian lineshapes that are characteristic to standard Raman peaks. As the polarization of the pump deviates from perfectly circular polarization, dispersive elements are added to the lineshape as constructive and destructive interference occurs between Raman and frequency-independent contributions to the signal. Figures 4.18b and c show how this effect can manifest itself across areas of a sample scan with large changes in birefringence.

4.6 Discussion

One of the major benefits that FSRS and RIKES promise for microscopy over CARS is the absence of a nonresonant background. This background arises entirely from electronic contributions to the signal, offering no chemical specificity and distorting the Raman lineshape. A primary goal of CARS spectroscopy and microscopy has been to reduce or eliminate entirely this nonresonant background while preserving the signal. Polarization CARS has been demonstrated to take advantage of the different polarization state of the nonresonant background relative to the resonant signal [3]. Pulse shaping approaches have been used for the same purpose [38, 39]. Time-domain methods have also been employed to utilize the longer-lived timescale of the resonant response relative to the nonresonant response [5, 6, 40, 41], similar to the method we applied in comparing coherent and spontaneous Raman scattering in chapter III. However, all of these methods have the drawback of losing some amount of signal along with the nonresonant background. With time-delay CARS, approximately 80% of the resonant signal remains after using time-delay nonresonant background suppression [6], while eliminating nearly all of the nonresonant background.

FSRS, on the other hand, has no nonresonant signal to combat. The signal occurs at stimulated Raman loss (SRL) or stimulated Raman gain (SRG) in the pump or probe fields, respectively. Because the signal is coherent and in-phase with the excitation fields, the fields themselves act as a local oscillator for heterodyne detection of the signal, albeit with no control over the strength of the local oscillator. As a result, for situations in which laser noise is dominant, increasing local oscillator can have a negative effect on signal to noise ratio [2]. High frequency detection can be performed for single mode SRS imaging when combined with lock-in detection [11]. This allows the detection to occur at frequencies in the MHz range, where laser sources generally have low noise, rather than in the Hz-kHz range, where lasers have significantly higher noise. For multiplex detection with photonic crystal fiber generating a continuum to act as the probe, noise levels at these frequencies can be much more significant, with any laser noise on the fiber input being amplified along with other noise sources that are introduced in the fiber itself [42]. As a result, increasing the strength of the local oscillator field can actually decrease the signal to noise level, and more precise control than allowed with FSRS is needed to avoid this.

The Raman-induced Kerr effect successfully avoids these pitfalls. There is no frequency-independent nonresonant background as in CARS. The primary limitation of RIKES involves the incoherent background introduced by strain birefringence in the optics between the initial polarizers and the analyzer. As shown in section 4.5.2, this can include birefringence introduced by the sample as well. The implications of this are very important when considering the possible advantages to doing RIKES instead of FSRS. We studied primarily polymer bead and onion cell samples, and both of these samples introduced significant birefringence that results in the depolarization of the probe beam. In particularly highly-scattering samples, care must be taken to not saturate the detector with the depolarized probe. To mitigate the effects of the birefringent background, we introduced a chopping scheme to isolate the resonant signal with a great degree of success. Birefringent background is mostly eliminated without losing any corresponding resonant signal. Unless samples are highly homogeneous and low-scattering, it is doubtful that RIKES detection will offer a significant advantage of FSRS without the implementation of such a chopping scheme. In onion samples, we observed both birefringence in the linear probe and in the circular pump, introducing a pump ellipticity that distorts the lineshape of the signal, further complicating detection and chemical identification.

One method often used to increase the sensitivity of RIKES measurements is to use heterodyne detection for Optical Heterodyne-Detected RIKES (OHD-RIKES). If one wants to perform optical heterodyne-detected RIKES, any local oscillator introduced can be precisely controlled by the careful rotation of polarizers [2, 9, 23] – the simple adjustment of the output polarizer allows a local oscillator to combine coherently with the RIKES signal in a highly controllable manner. Unfortunately, this method is not possible with the detector used in this experiment. Over the course of a raster scan, the birefringent background often reaches a level near detector saturation. While this disappears in the processed images because of the chopping scheme background subtraction, during data collection the background is measured on CCD. Thus, introducing any additional local oscillator field to the detection would saturate the detector and prevent imaging.

4.7 Conclusions

We have for the first time successfully demonstrated multiplex Raman-induced Kerr effect microscopy [24]. The experiment is based on a single laser source using continuum generation in a photonic crystal fiber as a probe. Using minor adjustments to the same setup, we were able to perform multiplex RIKES spectroscopy as well as femtosecond stimulated Raman scattering spectroscopy and microscopy. Comparison measurements were made with no disturbance to the sample, allowing the same image to be produced independently with both methods. With the implementation of a chopping scheme to eliminate birefringent background, RIKES offers a significantly higher signal to noise ratio than FSRS for spectroscopy and imaging using the same excitation conditions. For samples with large birefringence, the advantages conferred by RIKES are reduced, limiting its application in real-world imaging. With the recent use of lock-in cameras [19], fast modulation schemes could greatly enhance the sensitivity and reliability of RIKES for imaging.

References

[1] S. A. Akhmanov, A. F. Bunkin, S. G. Ivanov, and N. I. Koroteev. Coherent ellipsometry of Raman-scattering of light. *JETP Letters*, 25:416–420, 1977.

[2] G. L. Eesley. *Coherent Raman Spectroscopy.* Elsevier, Oxford, 1981.

[3] J. X. Cheng, L. D. Book, and X. S. Xie. Polarization coherent anti-Stokes Raman scattering microscopy. *Optics Letters*, 26(17):1341–1343, Sep 1 2001.

[4] F. M. Kamga and M. G. Skeats. Pulse-sequenced coherent anti-Stokes Raman scattering spectroscopy: a method for suppression of the nonresonant background. *Optics Letters*, 5:126, 1980.

[5] A. Volkmer, L. D. Book, and X. S. Xie. Time-resolved coherent anti-Stokes Raman scattering microscopy: Imaging based on Raman free induction decay. *Applied Physics Letters*, 80(9):1505–1507, Mar 4 2002.

[6] M. Cui, B. Bachler, and J. P. Ogilvie. Comparing coherent and spontaneous Raman scattering under biological imaging conditions. *Optics Letters*, 34:773–775, 2009.

[7] D. Pestov, G. O. Ariunbold, X. Wang, R. K. Murawski, V. A. Sautenkov, A. V. Sokolov, and M. O. Scully. Coherent versus incoherent Raman scattering: molecular coherence excitation and measurement. *Optics Letters*, 32(12):1725–1727, Jun 2007.

[8] J. J. Song, G. L. Eesley, and M. D. Levenson. Background suppression in coherent Raman spectroscopy. *Applied Physics Letters*, 29:9, 1976.

[9] M. D. Levenson and S. S. Kano. *Introduction to Nonlinear Laser Spectroscopy.* Academic Press, Inc., 1988.

[10] E. Ploetz, S. Laimgruber, S. Berner, W. Zinth, and P. Gilch. Femtosecond stimulated Raman microscopy. *Applied Physics B-Lasers and Optics*, 87(3):389–393, May 2007.

[11] C. W. Freudiger, W. Min, B. G. Saar, S. Lu, G. R. Holtom, C. W. He, J. C. Tsai, J. X. Kang, and X. S. Xie. Label-Free Biomedical Imaging with High Sensitivity by Stimulated Raman Scattering Microscopy. *Science*, 322(5909):1857–1861, Dec 2008.

[12] P. Nandakumar, A. Kovalev, and A. Volkmer. Vibrational imaging based on stimulated Raman scattering microscopy. *New Journal of Physics*, 11, Mar 2009.

[13] D. Zhang, M. N. Sipchenko, and J. X. Cheng. Highly Sensitive Vibrational Imaging by Femtosecond Pulse Stimulated Raman Loss. *Journal of Physical Chemistry Letters*, 2(11):1248–1253, Jun 2011.

[14] C. W. Freudiger, W. Min, G. R. Holtom, B. W. Xu, M. Dantus, and X. S. Xie. Highly specific label-free molecular imaging with spectrally tailored excitation-stimulated Raman scattering (STE-SRS) microscopy. *Nature Photonics*, 5(2):103–109, Feb 2011.

[15] E. R. Andresen, P. Berto, and H. Rigneault. Stimulated Raman scattering microscopy by spectral focusing and fiber-generated soliton as Stokes pulse. *Optics Letters*, 36(13):2387–2389, Jul 2011.

[16] H. T. Beier, G. D. Noojin, and B. A. Rockwell. Stimulated Raman scattering using a single femtosecond oscillator with flexibility for imaging and spectral applications. *Optics Express*, 19(20):18885–18892, 2011.

[17] Y. Ozeki, Y. Kitagawa, K. Sumimura, N. Nishizawa, W. Umemura, S. Kajiyama, K. Fukui, and K. Itoh. Stimulated Raman scattering microscope with shot noise limited sensitivity using subharmonically synchronized laser pulses. *Optics Express*, 18(13):13708–13719, Jun 2010.

[18] B. G. Saar, C. W. Freudiger, J. Reichman, C. M. Stanley, G. R. Holtom, and X. S. Xie. Video-Rate Molecular Imaging in Vivo with Stimulated Raman Scattering. *Science*, 330(6009):1368–1370, Dec 2010.

[19] S. Bourquin, R. P. Prasankumar, F. X. Kartner, J. G. Fujimoto, T. Lasser, and R. P. Salathe. High-speed femtosecond pump-probe spectroscopy with a smart pixel detector array. *Optics Letters*, 28(17):1588–1590, Sep 2003.

[20] S. Shim and R. A. Mathies. Femtosecond Raman-induced Kerr effect spectroscopy. *Journal of Raman Spectroscopy*, 39(11):1526–1530, 2008.

[21] C. W. Freudiger, M. B. J. Roeffaers, X. Zhang, B. G. Saar, W. Min, and X. S. Xie. Optical heterodyne-detected Raman-induced Kerr effect (OHD-RIKE) microscopy. *The Journal of Physical Chemistry B*, 5(ASAP):103–109, 2011.

[22] M. D. Levenson and J. J. Song. Raman-induced Kerr Effect. *Physical Review Letters*, 36:189–192, 1976.

[23] G. L. Eesley. Coherent Raman Spectroscopy. *Journal of Quantitative Spectroscopy & Radiative Transfer*, 22(6):507–576, 1979.

[24] B. R. Bachler, M. E. Fermann, and J. P. Ogilvie. Multiplex Raman induced Kerr effect microscopy. *Optics Express*, (in revision), 2011.

[25] L. Fu, B. K. Thomas, and L. Dong. Efficient supercontinuum generations in silica suspended core fibers. *Optics Express*, 16(24):19629–19642, 2008.

[26] T. W. Kee and M. T. Cicerone. Simple approach to one-laser, broadband coherent anti-Stokes Raman scattering microscopy. *Optics Letters*, 29(23):2701–2703, Dec 2004.

[27] C. L. Evans and X. S. Xie. Coherent Anti-Stokes Raman Scattering Microscopy: Chemical Imaging for Biology and Medicine. *Annual Review of Analytical Chemistry*, 1:883–909, 2008.

[28] J. X. Cheng and X. S. Xie. Coherent anti-Stokes Raman scattering microscopy: Instrumentation, theory, and applications. *Journal of Physical Chemistry B*, 108(3):827–840, Jan 22 2004.

[29] A. Zumbusch, G. R. Holtom, and X. S. Xie. Three-dimensional vibrational imaging by coherent anti-Stokes Raman scattering. *Physical Review Letters*, 82(20):4142–4145, May 17 1999.

[30] A. Volkmer. Vibrational imaging and microspectroscopies based on coherent anti-Stokes Raman scattering microscopy. *Journal of Physics D-Applied Physics*, 38(5):R59–R81, Mar 2005.

[31] J. P. R. Day, K. F. Domke, G. Rago, H. Kano, H. O. Hamaguchi, E. M. Vartiainen, and M. Bonn. Quantitative Coherent Anti-Stokes Raman Scattering (CARS) Microscopy. *Journal of Physical Chemistry B*, 115(24):7713–7725, Jun 2011.

[32] Sigma-Aldrich Co. Toluene Raman spectrum, 2011.

[33] E. L. Hommel and H. C. Allen. The air-liquid interface of benzene, toluene, m-xylene, and mesitylene: a sum frequency, Raman, and infrared spectroscopic study. *The Analyst*, 128:750–755, 2003.

[34] Sigma-Aldrich Co. Polystyrene Raman spectrum, 2011.

[35] John Blackwell. *Infrared and Raman Spectroscopy of Cellulose*, chapter 15, pages 206–218. 1977.

[36] I. H. Shin, J. Y. Lee, S. Lee, D. J. Lee, and D. Y. Kim. Measurement of relative phase distribution of onion epidermal cells by using the polarization microscope - art. no. 644317. In J. A. Conchello, C. J. Cogswell, and T. Wilson, editors, *Three-Dimensional and Multidimensional Microscopy: Image Acquisition and Processing XIV*, volume 6443 of *Proceedings of the Society of Photo-Optical Instrumentation Engineers (SPIE)*, pages 44317–44317. 2007.

[37] M. D. Levenson and J. J. Song. Raman-induced Kerr effect with elliptical polarization. *Journal of the Optical Society of America*, 66(7):641–643, 1976.

[38] N. Dudovich, D. Oron, and Y. Silberberg. Single-pulse coherently controlled nonlinear Raman spectroscopy and microscopy. *Nature*, 418(6897):512–514, Aug 1 2002.

[39] S. H. Lim, A. G. Caster, O. Nicolet, and S. R. Leone. Chemical imaging by single pulse interferometric coherent anti-Stokes Raman scattering microscopy. *Journal Of Physical Chemistry B*, 110(11):5196–5204, Mar 23 2006.

[40] M. Cui, M. Joffre, J. Skodack, and J. P. Ogilvie. Interferometric Fourier transform coherent anti-Stokes Raman scattering. *Optics Express*, 14(18):8448–8458, Sep 2006.

[41] J. P. Ogilvie, E. Beaurepaire, A. Alexandrou, and M. Joffre. Fourier-transform coherent anti-Stokes Raman scattering microscopy. *Opt. Lett.*, 31(4):480–482, 2006.

[42] K. L. Corwin, N. R. Newbury, J. M. Dudley, S. Coen, S. A. Diddams, B. R. Washburn, K. Weber, and R. S. Windeler. Fundamental amplitude noise limitations to supercontinuum spectra generated in a microstructured fiber. *Applied Physics B-Lasers and Optics*, 77(2-3):269–277, Sep 2003.

CHAPTER V

Surface-enhanced Raman Spectroscopy

5.1 Introduction

Surface-enhanced Raman scattering (SERS) is a Raman technique that utilizes rough metallic surfaces to achieve large enhancements of Raman signals for molecules adsorbed to the surface. The enhancement factor has been observed to be as high as $10^{10} - 10^{13}$ [1–3], with detection limits down to the single molecule level having been demonstrated [4, 5]. The ability to manipulate this enhancement factor and utilize it in a controlled manner for drastically increasing the sensitivity of Raman measurements is one of the areas of research that has exploded over the past thirty years, with over five thousand research articles, one hundred review articles, and several books having been written on the topic of SERS in that time [6].

The mechanism behind the million-fold signal enhancement in SERS is still not fully understood, with multiple effects hypothesized to contribute to the enhancement. Generally, the enhancement effect is considered to be the product of two contributions: 1) an electromagnetic enhancement mechanism, and 2) a chemical enhancement mechanism. The electromagnetic mechanism is thought to provide the bulk of the enhancement, with a factor of 10^4 enhancement. It was first proposed by Gersten [7–10], Nitzan [7, 10], and McCall et al. [11, 12] in 1980. The theory was further expanded upon by Kerker et al. [13–17]. When an electromagnetic field interacts with a metal surface, the local field at the surface of the metal may be greatly enhanced by the excitation of localized surface plasmons on the metal substrate [6]. The size of the field enhancement is owed to a double-enhancement effect near the surface of the metal nanostructure. As a result of the excitation of the localized surface plasmon resonance (LSPR), the local excitation field is enhanced by a factor of $\sim 10^2$. This enhanced field then gives rise to a Raman signal, which itself is then magnified by the same $\sim 10^2$ factor, leading to an overall electromagnetic enhancement factor of $\sim 10^4$. It should be noted that the enhancement is wavelength-dependent, with Stokes radiation closest to the excitation frequency allowing largest enhancement [18]. Some of the highest enhancements have been recorded with configurations such as surface-enhanced hyper-Raman scattering [3].

A second enhancement effect, a chemical enhancement, is strongly suggested by experimental evidence. With an enhancement factor (EF) of $\sim 10^2$, this effect is weaker than (and completely independent of) the electromagnetic enhancement. If electromagnetic enhancement were the only effect contributing to the signal magnification, all molecules adsorbed on a SERS substrate should experience roughly the same enhancement. However, the SERS intensities of CO and N_2 under the same experimental conditions differ by a factor of 200 [18]. This result is very difficult to explain by invoking only an electromagnetic enhancement. Orientational differences upon adsorption are insufficient to explain such a large difference in signal, and the polarizabilities of the molecules are nearly identical. A second line of evidence pointing to the existence of a chemical enhancement factor can be found in potential-dependent electrochemical experiments. If either the potential or laser frequency is scanned with the other being fixed, broad resonances are observed. The hypothesis that best explains this effect is that new electronic states arising from chemisorption serve as resonant intermediate states in Raman scattering [18]. Here, charge-transfer excitations from metal→molecule or molecule→metal can take place at about half the energy of the absorbate's intrinsic intramolecular excitations.

Because of the nonlinear dependence of coherent anti-Stokes Raman scattering (CARS), it can be reasonably inferred that surface-enhanced effects could achieve extremely high enhancement. This scheme, called surface-enhanced coherent anti-Stokes Raman scattering (SECARS), was predicted by Shen et al. in 1979 [19]. They demonstrated that the nonlinear mixing of four surface plasmons on a silver substrate can enhance the coherent anti-Stokes Raman scattering signal from benzene at the surface of the substrate. However, this result was obtained using 30 nanosecond pulse duration. For picosecond excitation, it could be assumed that surface-enhanced CARS could be performed with submonolayer detection sensitivity at the surface of the substrate. Under these conditions, however, $\chi^{(3)}$ from the metal may dominate $\chi^{(3)}$ from the molecule. This will induce a large non-chemically specific background that plagues spectroscopic detection of the CARS signal [20].

5.2 History

Surface-enhanced Raman spectroscopy was first observed by Fleischmann, Hendra, and McQuillan in 1974 [21]. The experiment consisted of Raman detection of pyridine adsorbed onto an electrochemically-roughened silver electrode. Fleischmann et al. observed a significant increase in Raman intensity, which at the time they attributed to the increased surface area of the roughened electrode. Figure 5.1 shows the experimental configuration that produced the observation. Three years later in 1977, van Duyne and Jeanmaire recognized that the increased surface roughness of the substrate was insufficient to account for the large increase in Raman signal levels detected [22]. They postulated an electric field enhancement effect at the roughened surface of the substrate. The same year, Albrecht and Crighton made the same observation, citing possible surface effects that increase the molecular Raman scattering cross section for species (in their case, pyridine) adsorbed onto the surface of the

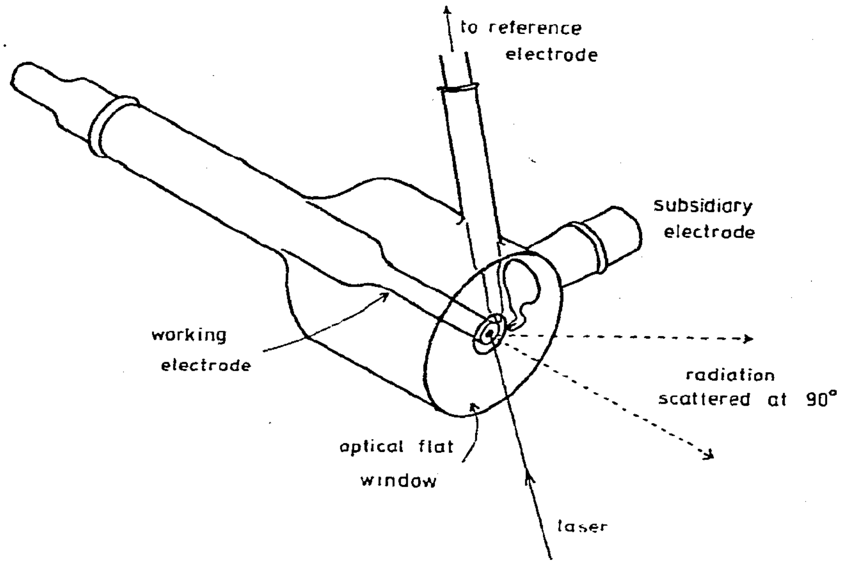

Figure 5.1: Experimental configuration for original surface-enhanced Raman observation by Fleischmann [21].

substrate [23]. As discussed in section 5.1, the total enhancement factor is currently believed to contain contributions from both effects.

The idea of applying this surface-enhanced technique to coherent Raman methods was first put into effect by Shen et al. in 1979 [19]. In the case of surface-enhanced CARS, two surface-plasmon waves at ω_1 and ω_2 propagate on the plane boundary surface between a metal (i.e. silver) and a dielectric medium with wave vectors $(\vec{k}_1)_\parallel$ and $(\vec{k}_2)_\parallel$, respectively. These waves travel parallel to the surface and interact on the surface via the third-order nonlinearity in the medium to generate a third-order nonlinear polarization at $\omega_a = 2\omega_1 - \omega_2$. This nonlinearity will in turn generate a surface anti-Stokes plasmon wave at ω_a. If the frequency difference $\omega_1 - \omega_2$ is near a resonant frequency of an excitation in the medium, the anti-Stokes plasmon wave will be resonantly enhanced. Thus, like CARS, surface-enhanced CARS (SECARS) can be used to spectroscopically study Raman vibrational modes of a medium with high sensitivity. The experimental geometry used by Shen et al. is shown in Figure 5.2 [19]. It is important to note that the anti-Stokes signal wave vector $(\vec{k}_a)$ is spa-

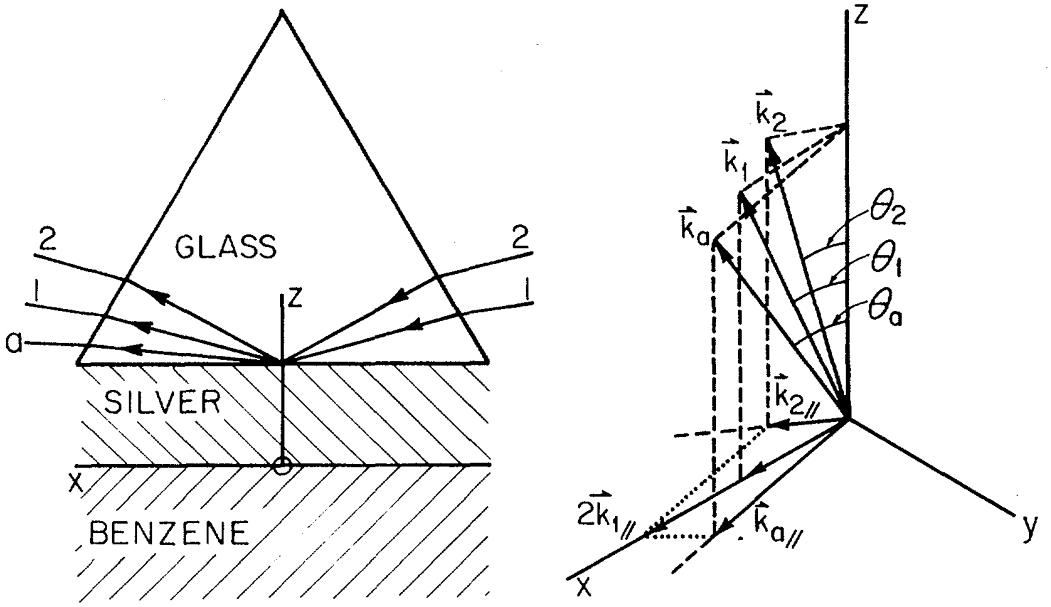

Figure 5.2: Experimental configuration for surface-enhanced coherent anti-Stokes Raman scattering (SECARS) measurement by Shen et al. [19]

tially separated from the excitation beams at an angle θ_a, allowing convenient signal extraction. Only a few other SECARS studies have been performed to date [24–27], but most of them have studied the effects on gold and silver colloids. During the writing of this dissertation, the first study of SECARS on a commercial SERS substrate has been reported [28]. This study cites an enhancement over standard CARS measurements of 10^5.

Work in surface-enhanced Raman scattering remained fairly uneventful until being revived again by Kneipp et al. [5, 29–33] and Nie et al. [4, 34–37] in the late 90s. Their claims of single-molecule detection invigorated the field, promising unprecedented sensitivity with what would otherwise be considered a low-sensitivity technique. The initial single-molecule observation by Kneipp et al. measured spectra from a single crystal violet molecule in an aqueous colloidal silver solution using a one second collection time [29]. These results have paved the way for many of the recent studies involving biological samples.

5.3 Introduction to Surface Plasmons

The primary driver of the physics of surface-enhanced effects in nanostructured metal surfaces is the localized surface plasmon resonance (LSPR). The localized surface plasmon resonance occurs when the frequency of incident light is resonant with a collective oscillation of valence electrons in a metal substrate. These oscillations occur at the surface of the metal and can propagate as a surface charge density wave, commonly referred to as a "surface plasmon". It is instructive to consider the case of localized transverse magnetic (TM) surface plasmon waves at a plane interface between two semi-infinite isotropic media a and b [20]. In this case, the surface wave propagating parallel to the surface interface in the $\hat{x}$ direction can be written as:

$$\begin{aligned} \vec{\mathbf{E}} &= \left(\hat{x}E_{ax} + \hat{z}E_{az}\right)e^{iKx-\alpha_a z-i\omega t} \qquad \text{for } z > 0 \\ \vec{\mathbf{E}} &= \left(\hat{x}E_{bx} + \hat{z}E_{bz}\right)e^{iKx+\alpha_b z-i\omega t} \qquad \text{for } z < 0 \end{aligned} \tag{5.1}$$

where, in order to satisfy the wave equation, the constants K and α must be related by the following [20]:

$$\begin{aligned} K^2 - \alpha_a^2 &= \left(\tfrac{\omega}{c}\right)^2 \varepsilon_a \qquad \text{in medium a } (z > 0) \\ K^2 - \alpha_b^2 &= \left(\tfrac{\omega}{c}\right)^2 \varepsilon_b \qquad \text{in medium b } (z < 0) \end{aligned} \tag{5.2}$$

$z = 0$ represents the physical location of the boundary between the two media a and b. Here, the surface wave must be equal for both cases $(z > 0)$ and $(z < 0)$, leading to the following boundary conditions:

$$\begin{aligned} E_{ax} &= E_{bx} \\ \varepsilon_a E_{az} &= \varepsilon_b E_{bz} \end{aligned} \tag{5.3}$$

From Maxwell's equations in a source-free medium, we know $\nabla \cdot \vec{\mathbf{E}} = 0$. This allows us to retrieve relations between E_{ax} and E_{az} and their counterparts in medium b:

$$\nabla \cdot \vec{\mathbf{E}} = \frac{\partial}{\partial x} E_x + \frac{\partial}{\partial y} E_y + \frac{\partial}{\partial z} E_z = 0 \tag{5.4}$$

$$\begin{array}{rcl|rcl}
\multicolumn{3}{c}{\text{for } z > 0} & \multicolumn{3}{c}{\text{for } z < 0} \\
\hline
0 & = & (iKE_{ax} - \alpha_a E_{az}) & 0 & = & (iKE_{bx} + \alpha_b E_{bz}) \\
 & & \times e^{iKx - \alpha_a - i\omega t} & & & \times e^{iKx + \alpha_b - i\omega t} \\
0 & = & (iKE_{ax} - \alpha_a E_{az}) & 0 & = & (iKE_{bx} + \alpha_b E_{bz}) \\
iKE_{ax} & = & \alpha_a E_{az} & iKE_{bx} & = & -\alpha_b E_{bz} \\
\hline
E_{az} & = & \left(\frac{iK}{\alpha_a}\right) E & E_{bz} & = & \left(-\frac{iK}{\alpha_b}\right) E_{bx} \\
\hline
\end{array} \tag{5.5}$$

These relationships allow the boundary conditions in equation 5.3 to be written:

$$\begin{gathered} E_{ax} = E_{bx} \\ \varepsilon_a \left(\frac{iK}{\alpha_a}\right) E_{ax} = \varepsilon_b \left(\frac{-iK}{\alpha_b}\right) E_{bx} \end{gathered} \tag{5.6}$$

This is a set of coupled differential equations whose determinant should vanish for the case $E_{ax}, E_{bx} \neq 0$, leading to [20]:

$$\varepsilon_a \alpha_b + \varepsilon_b \alpha_a = 0 \tag{5.7}$$

Substituting this relationship back into equation 5.2, we can retrieve the dispersion relation for the surface plasmon wave:

$$K^2 = \left(\frac{\omega}{c}\right)^2 \frac{\varepsilon_a \varepsilon_b}{\varepsilon_a + \varepsilon_b} \tag{5.8}$$

The constants α_a and α_b must be positive and real for the surface wave to be able to propagate, implying (from equation 5.2) that $K^2 > (\omega/c)^2 \varepsilon_a$ and $K^2 > (\omega/c)^2 \varepsilon_b$.

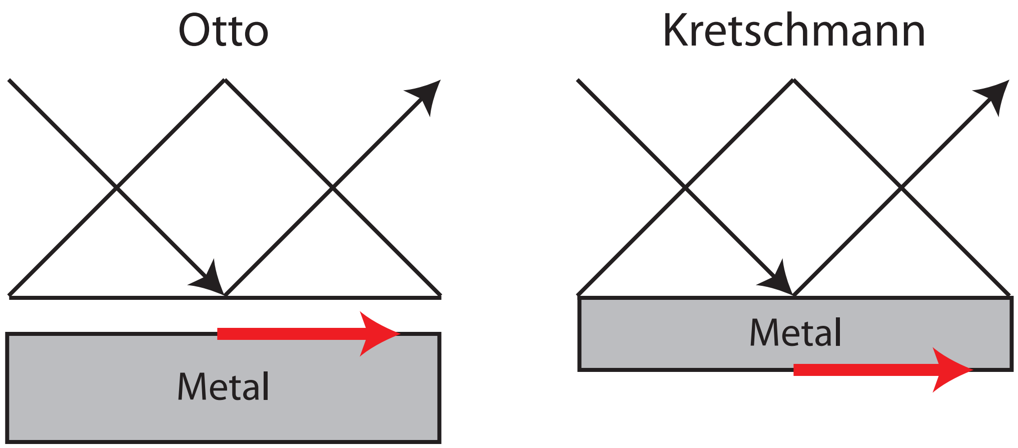

Figure 5.3: Diagrams of the Otto configuration and Kretschmann configuration for the excitation of surface plasmon waves. Shown in red is the surface plasmon wave generated by the incident radiation.

This is only true for $\varepsilon_a < 0$ and $|\varepsilon_a| > \varepsilon_b$, or $\varepsilon_b < 0$ and $|\varepsilon_b| > \varepsilon_a$, implying that one of the two media must have a negative dielectric constant. The most common materials with this property are metals excited below the plasma frequency [20]. The electromagnetic waves generated at the metal surface are always TM in nature, and they are generally referred to as surface plasmon waves.

Two primary configurations have been proposed to excite surface plasmon waves. The first configuration is known as the Otto configuration [38], shown in Figure 5.3. In this configuration, an excitation beam is incident on a glass prism, where it is refracted and generates an evanescent wave at the glass-air interface. This wave propagates to the metal substrate below and excites a surface plasmon wave (shown as a red arrow) at the top surface of the metal. In this case, there is a thin layer of air separating the glass and metal interfaces. In 1971, a more stable configuration was proposed by Kretschmann, also shown in Figure 5.3 [39]. In the Kretschmann configuration, the metal and glass surfaces are in direct contact, allowing the metal substrate material to be located between the air and glass interface. For this configuration, the evanescent wave propagates through the metal and excites a surface plasmon wave (shown in red) on the bottom side of the metal. The Kretschmann configuration is generally regarded as more stable and easier to implement experimentally. At the right incidence angle, the incident wave can be strongly coupled into surface plasmon waves, which will in turn generate an intensity enhancement. In general, this enhancement factor is much higher for rough nanoscale structures on the surface of the metal [40].

5.4 Experimental Setup and Previous Results

To attempt to perform surface-enhanced Raman measurements in our lab, we employ a recently developed commercial nanostructured metal substrate. The substrate used in our experiment is called Klarite® from D3 technologies. This commercial substrate offers high reproducibility and stability compared to home-grown nanostructures, making it particularly appealing for our measurements. Figure 5.4 shows scanning electron microscope (SEM) images of the nanostructured substrate [41]. The structure of the substrate surface consists of inverted gold (Au) pyramid structures arranged in a square grid. The sharp edges of the pyramids offer the necessary field enhancement for high magnification (quoted at 10^6 [42]) of Raman signals. Figure 5.4a shows a top-down view of the metal surface, where the grid-like arrangement of inverted pyramids can be seen. Figure 5.4b shows an angled-down view, where the depth of the pyramidal wells can be seen. A picture of the Klarite® substrate mounted on a standard glass slide is shown in Figure 5.5.

Figure 5.6 shows simulations of the location and relative strength of the plamon resonances on the substrate based on a 2D finite-difference time-domain (FDTD) model [41]. The image is based on a well depth of $1.25\mu m$ and an excitation wavelength of 785 nm, with normal incidence of excitation. The structure and arrangement of the inverted pyramids on the substrate are specifically designed to provide high stability and reproducibility of these plasmon resonances. Figure 5.7 shows a reflection spectrum of the Klarite® surface as a function of wavelength for gold coated (yellow)

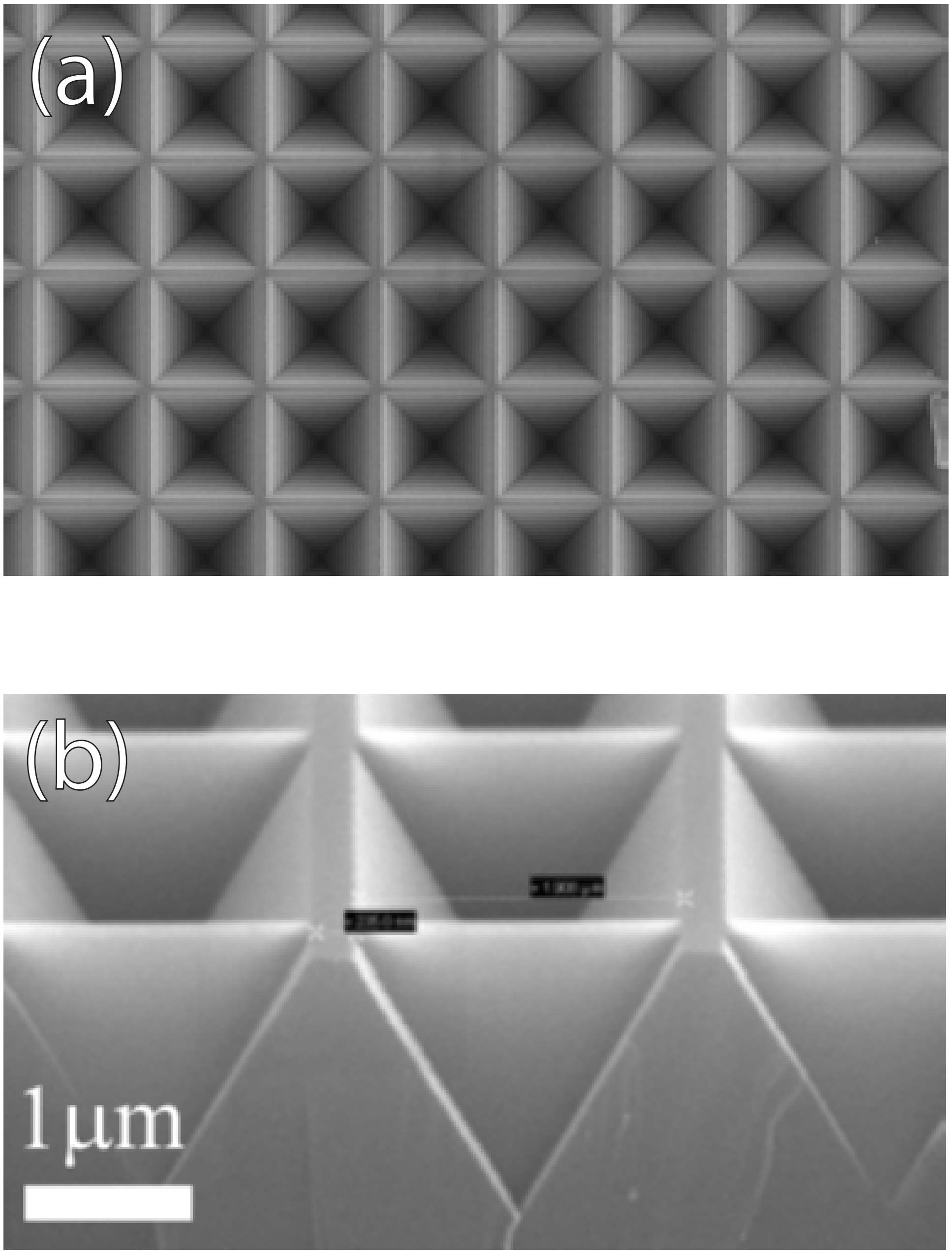

Figure 5.4: SEM images of the nanostructured metal substrate. a) Top-down view and b) angled view of the inverted nano-pyramids on the metal surface [41].

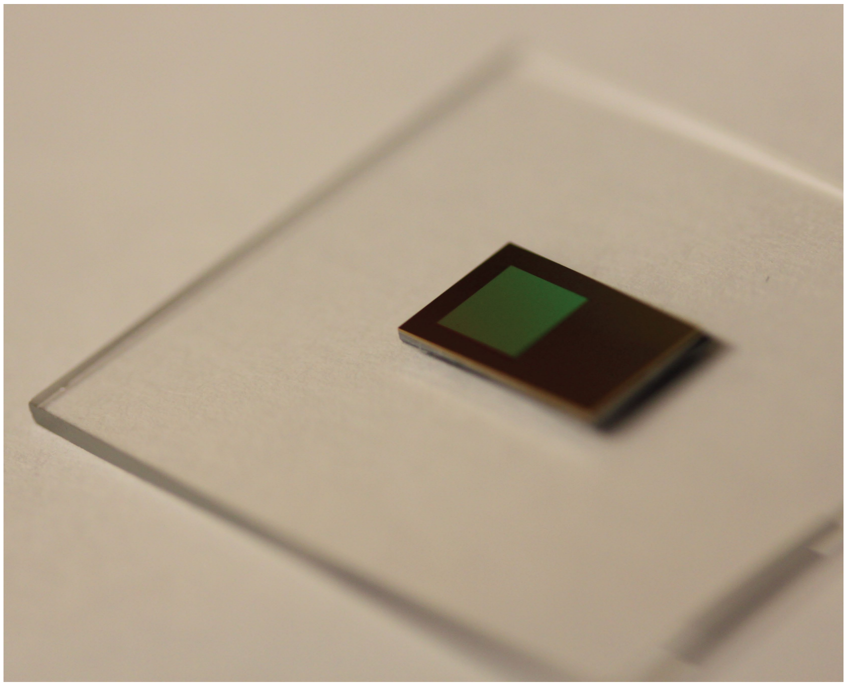

Figure 5.5: Picture of Klarite® substrate mounted on glass slide.

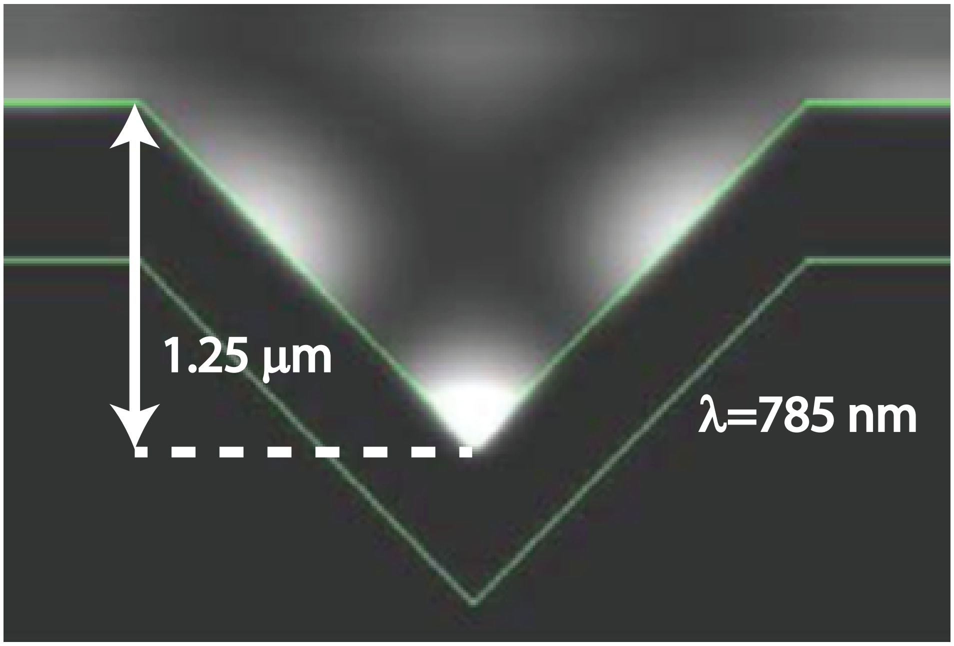

Figure 5.6: Diagram of simulated plasmon resonance strengths in metal substrate using 785 nm wavelength excitation. The depth of the well is $1.25\mu m$ [41].

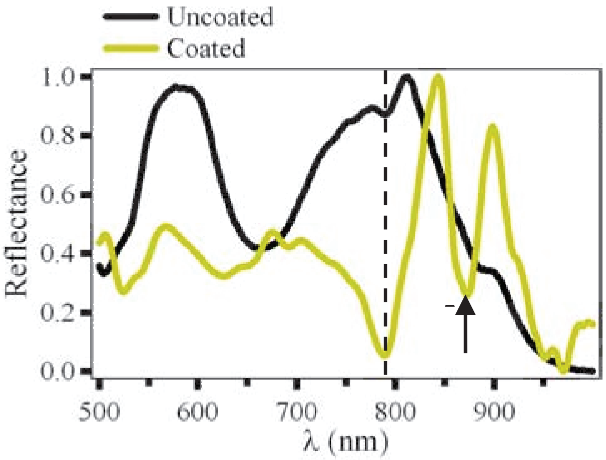

Figure 5.7: Reflection spectra of Klarite® surface as a function of wavelength for coated (yellow) and uncoated (black) substrate. Reflectance dips (shown with arrow) correspond to plasmon resonances [41].

and uncoated (black) substrate [41]. The dips in the spectrum correspond to plasmon resonances. The wavelengths in the 800 nm range are chosen in our experiment to overlap these broad plasmon resonances.

It has been shown that gold nanostructured surfaces can undergo irreversible loss of signal due to overheating of the substrate [43]. The enhanced field at the nanostructures on gold substrates can induce annealing, causing permanent morphological change in the structured substrate. Substrate heating was shown to cause loss of enhancement due to degradation of the "hot" site from annealing processes, and the resulting surface diffusion of the adsorbates caused the loss of signal to be irreversible. These results were confirmed in our lab on Klarite® substrates using a 75 MHz Ti:sapphire oscillator.

To solve the problem of excessive substrate heating for our Raman measurements, we have employed a commercial pulse picker to reduce the repetition rate of our laser system, much like the implementation used by Ichimura et al. for tip-enhanced CARS excitation with a Ti:sapph oscillator [44]. This allows us to be able to reduce the average power on the sample to prevent substrate damage while maintaining the high peak intensity of the individual laser pulses for nonlinear excitation. The pulse picker is a commercial electro-optic modulator (EOM) from Conoptics (Model 25D) that rotates the polarization of desired pulses by 90°, allowing the undesired pulses to be rejected by a polarizer crossed perpendicular to a polarizer at the input of the pulse picker. This allows a fully-adjustable repetition rate electronically, without having to change the alignment of any optics. The downside to using the pulse picker is the high amount of group delay dispersion of the 16 cm long KDP crystal used for the electro-optic modulator. The total dispersion induced in the full optical system is $\sim 10^4$ fs^2, which is much larger than can be compensated with the available chirped mirrors. To compensate for the large dispersion, we use a 4f pulse shaper with a 640 pixel spatial light modulator (SLM) at the Fourier plane [45]. Using a technique developed by Lozovoy et al. called multiphoton intrapulse interference phase scan (MIIPS) [46, 47], we can fully characterize the spectral phase of our pulses and compensate accordingly, allowing us to achieve nearly transform-limited pulses for arbitrary levels of dispersion.

Figure 5.8 shows the experimental setup used for the surface-enhanced Raman experiment. The experiment is set up in a very similar configuration to the setup of chapter III (i.e. CSRS is used instead of CARS to provide a clean comparison between SECARS and SERS signals. The pump and Stokes pulses can be blocked at the Fourier plane to perform SERS instead of SECARS.). A 75 MHz pulse train is output from a Ti:sapph oscillator (Femtosource Synergy) and feeds into a Conoptics Model 25D pulse picker used to electronically control the repetition rate of the laser source. This is fed into a 4f pulse shaper with a spatial light modulator (SLM) to perform MIIPS. At the entrance slit to the spatial light modulator, an amplitude mask is used to pick out three pulses to be used for CSRS, exactly like the setup used in section 3.3. Again, a glass coverslide is used to provide a delay for the probe pulse for nonresonant background suppression.

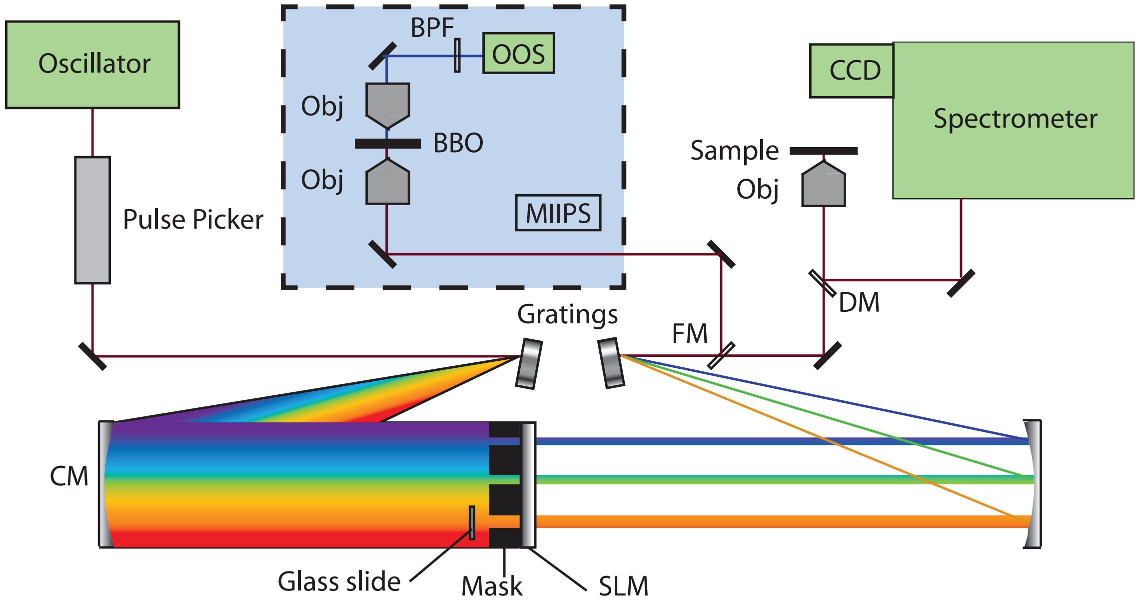

Figure 5.8: Experimental setup diagram for surface-enhanced Raman experiment. CM - curved mirror; SLM - spatial light modulator; Obj - objective lens; BBO - 20 μm thick β-barium borate crystal for second harmonic generation; FM - flipper mirror for switching to/from MIIPS setup; DM - dichroic mirror; BPF - bandpass filter; CCD - charge coupled device.

The output of the 4f pulse shaper is directed along one of two paths via a flipper mirror. First, the mirror is flipped up and the beam is directed into the MIIPS setup (shown in the light blue box in Figure 5.8). Here, the MIIPS program is run and the SLM is adjusted to compensate the material dispersion for the full path. When running MIIPS, we use all of the relevant optics that are used in the actual experiment to set the SLM to compensate exactly the dispersion for the measurement. After the SLM is properly set to compensate for group delay dispersion, the flipper mirror is flipped down and the beam is sent into the objective and onto the sample.

Because the sample is on a metal substrate and is thus optically opaque, we use an epi-detection scheme to collect our signal. After the excitation beam is incident on the Klarite®, the signal is generated at the surface and collected by the same objective (0.4 NA) used for excitation. The signal is then directed to a different path via a dichroic mirror, where it is directed into a spectrometer (Horiba Jobin

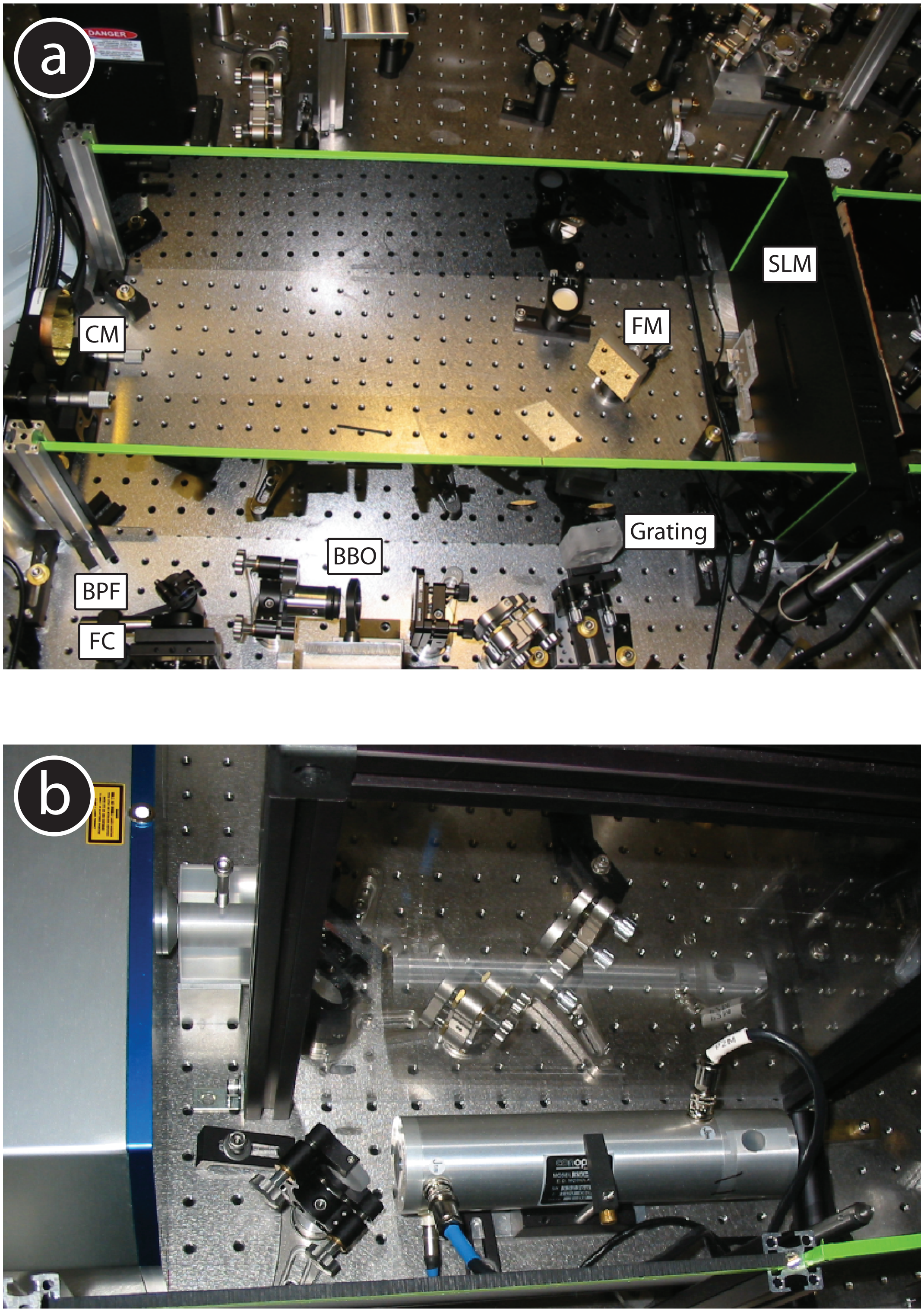

Figure 5.9: Pictures of experimental setup. a) Picture of 4f pulse shaper with MIIPS setup: SLM - spatial light modulator; FM - folding mirror; CM - curved mirror; BBO - 20 μm thick β-barium borate crystal for second harmonic generation; BPF - bandpass filter; FC - fiber coupler to spectrometer. b) Picture of the pulse picker.

Yvon IHR320) and detected using a Pixis 100F CCD. Figure 5.9 shows pictures taken of the setup. Figure 5.9a shows the 4f pulse shaper with MIIPS setup at the bottom of the photograph. Figure 5.9b shows a picture of the pulse picker, with the cube polarizer used to reject unwanted pulses attached on the right end inside the cylindrical enclosure (output port is visible as a circular hole in the cylinder).

The analyte used in our experiment is benzenethiol. Benzenethiol is useful because it has a particularly strong Raman mode within our accessible bandwidth at 997 cm^{-1} (full Raman spectrum shown in Figure 5.10), and the thiol group in benzenethiol bonds strongly with the surface of the gold substrate. The strength of the bond allows the benzenethiol molecules to form self-assembling monolayers on the surface of the substrate [49], making benzenethiol an extremely useful sample for surface-enhanced studies.

Preliminary work was done in our lab on these samples by Meng Cui using Fourier-transform coherent anti-Stokes Raman scattering (FTCARS) [50]. FTCARS is a time-domain Raman technique in which the full bandwidth of the laser is used to generate Raman coherences in the sample (pump pulse), and a time delay τ later a second identical probe pulse probes the coherence. After spectrally selecting the anti-Stokes wavelength component of the signal, a time trace of the signal is collected with a photomultiplier tube (PMT). Figure 5.11a shows the time trace of the anti-Stokes signal as a function of delay time between the pump and probe pulses. When a Fourier transform is applied to this data, the Raman spectrum with bandwidth corresponding to the full oscillator pulse bandwidth is recovered (Figure 5.11b). A large signal at 997 cm^{-1} can be seen in the Raman spectrum, corresponding to the ring-breathing mode of benzenethiol. The same technique was used to measure the Raman spectrum of benzenethiol adsorbed onto the flat gold portion of the Klarite® surface. No signal could be seen, indicating that the measured spectrum in Figure 5.11b may be FTCARS signal strongly enhanced by the nanostructured gold substrate

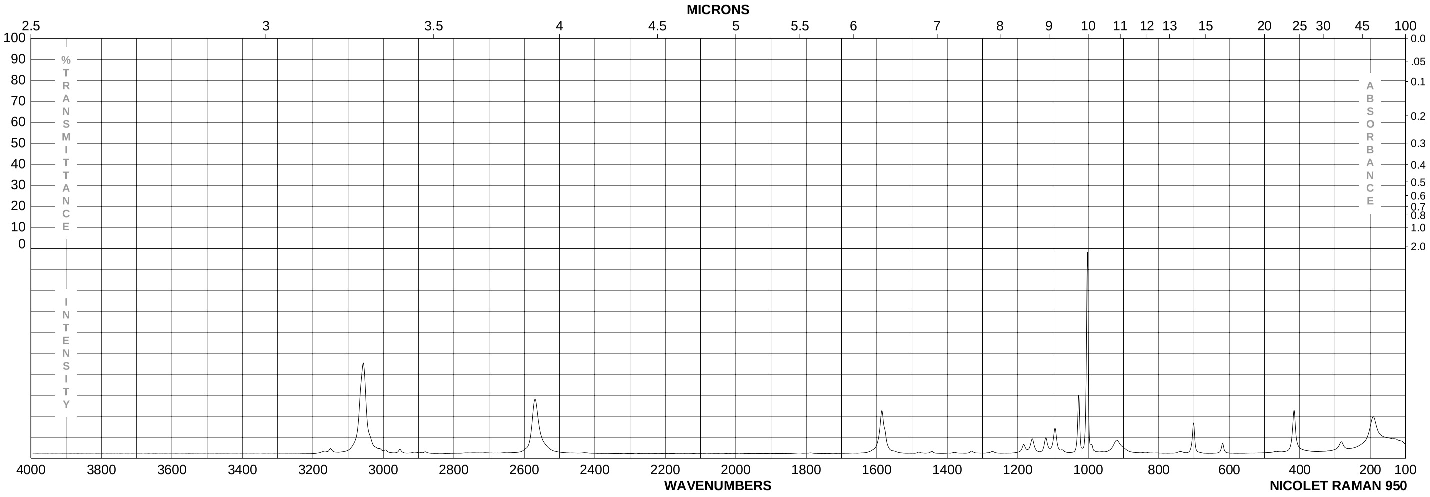

Figure 5.10: Spontaneous Raman spectrum for benzenethiol [48].

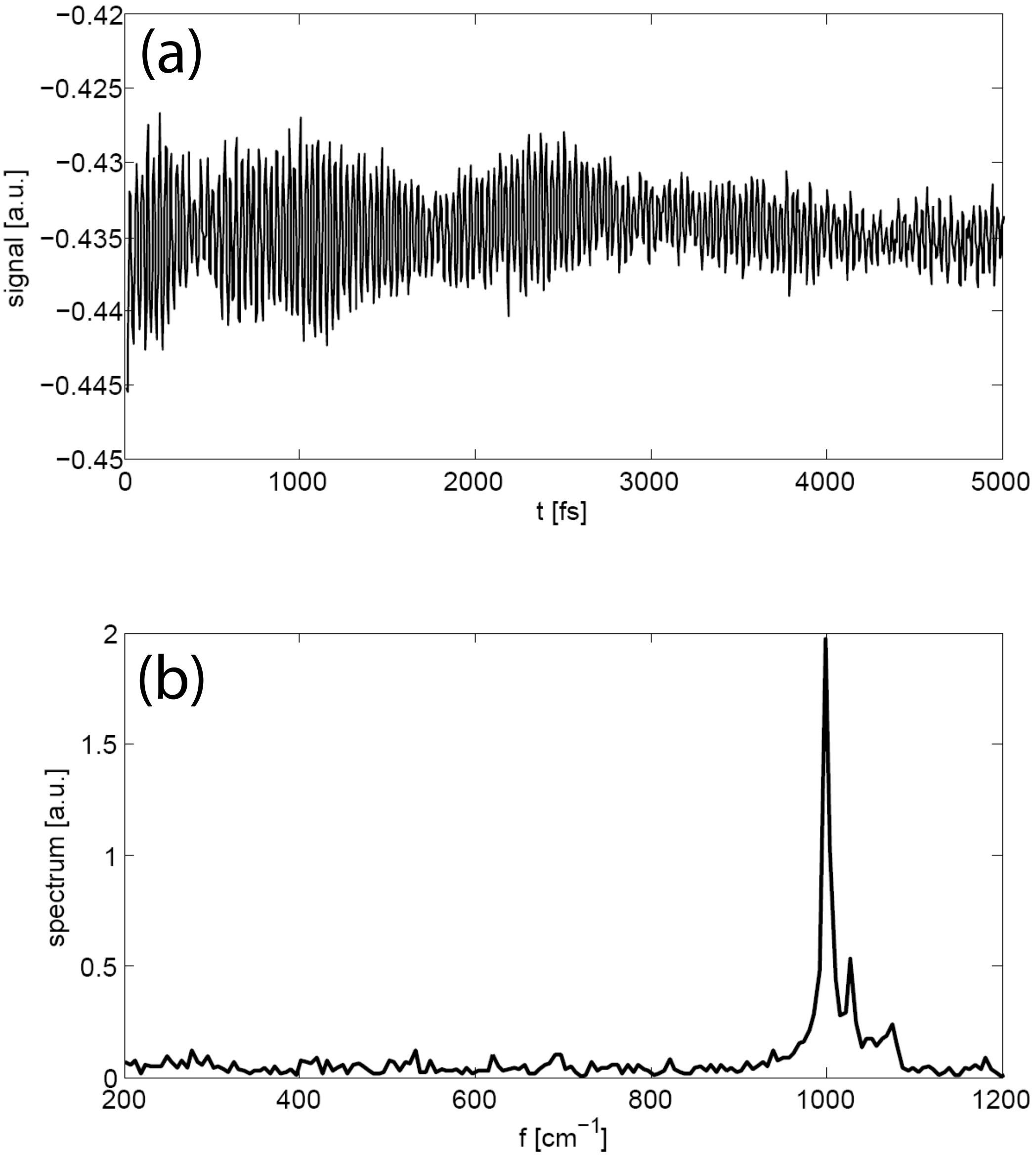

Figure 5.11: FTCARS results for benzenethiol adsorbed on Klarite® substrate. a) Time-domain trace of FTCARS signal. b) Raman spectrum retrieved from Fourier transform of data in (a) [50].

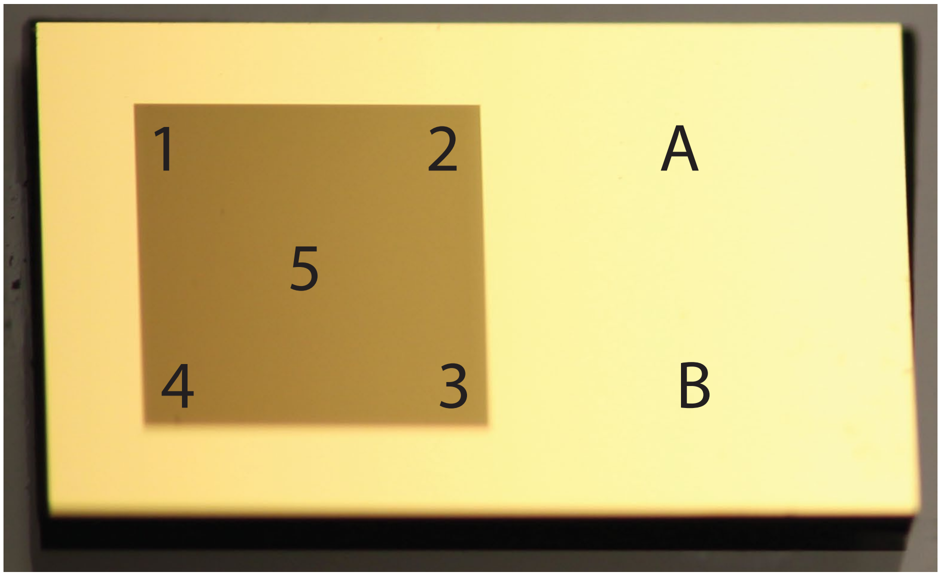

Figure 5.12: Picture of Klarite® used in our experiment, with measurement locations 1-5, A, B indicated.

[50]. Difficulties in reproducibility have made this hypothesis difficult to verify.

5.5 Experimental Results

To test our ability to detect surface-enhanced Raman signal on Klarite®, we first perform standard surface-enhanced Raman spectroscopy using continuous-wave (CW) excitation. To perform these measurements, we use a Raman detection setup in the lab of Professor Michael Morris at the University of Michigan. The system is a Nikon E600 epi-illumination microscope with a 20x/0.75 NA Nikon S Fluor objective. The system uses an excitation wavelength of 785 nm, with 100 mW total excitation power and $\sim 4\ cm^{-1}$ resolution. A 0.3 ND filter is used to reduce excitation power, which can reach 8-11 mW at the sample. The excitation is focused to a line of size $100\mu m \times 10\mu m$ and detected on a 128×1024 pixel CCD. Figure 5.12 shows an image of the Klarite® samples used in these measurements. Five different locations on the patterned substrate (labeled numbers 1-5) are used for measurements to gauge the consistency of SERS measurements. Two locations (A and B) are used for detection

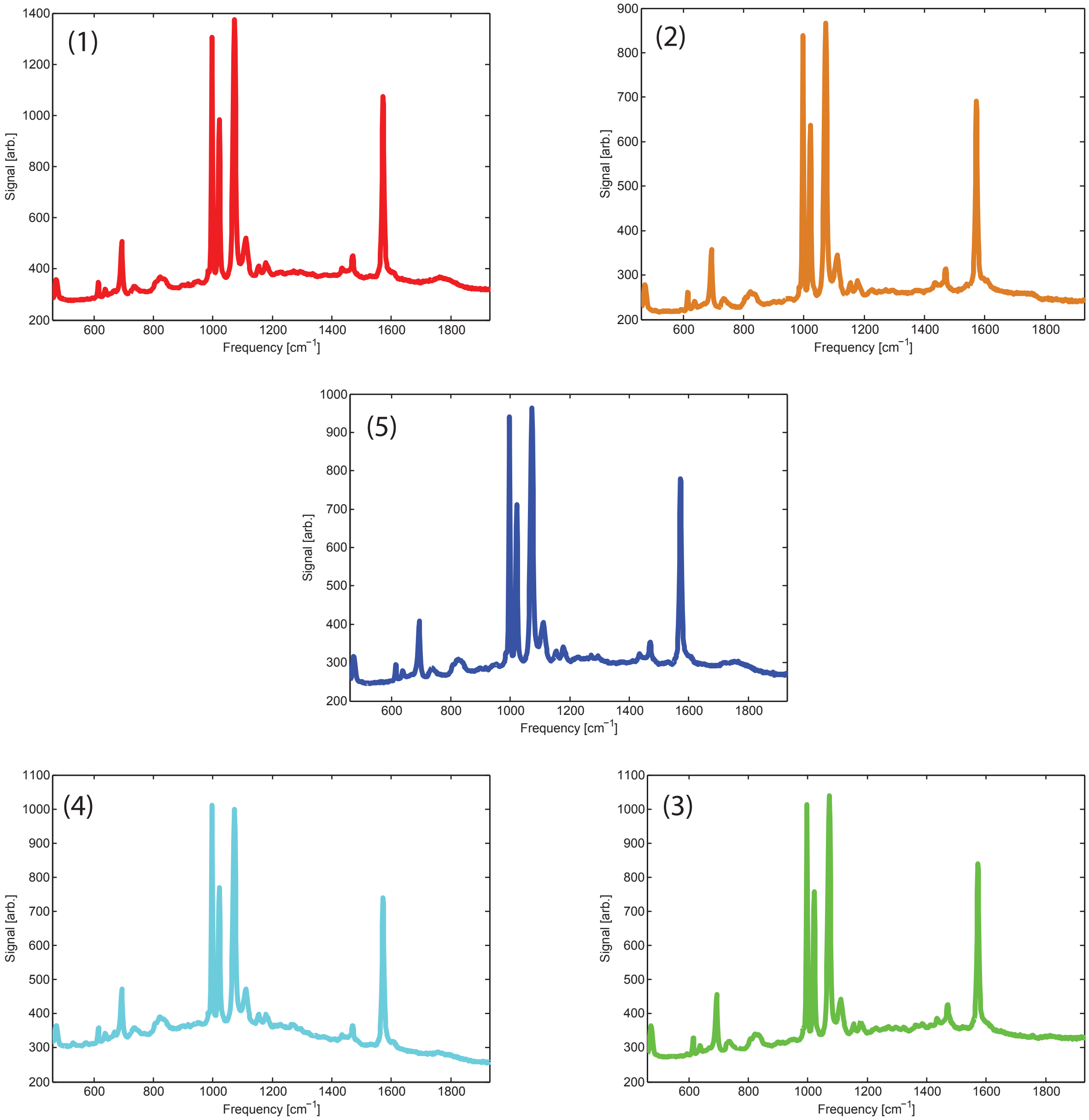

Figure 5.13: Surface-enhanced spontaneous Raman data (taken in Morris lab) for benzenethiol adsorbed on structured portion of Klarite® substrate. Numbers (1-5) represent the location on the substrate surface at which the data was taken.

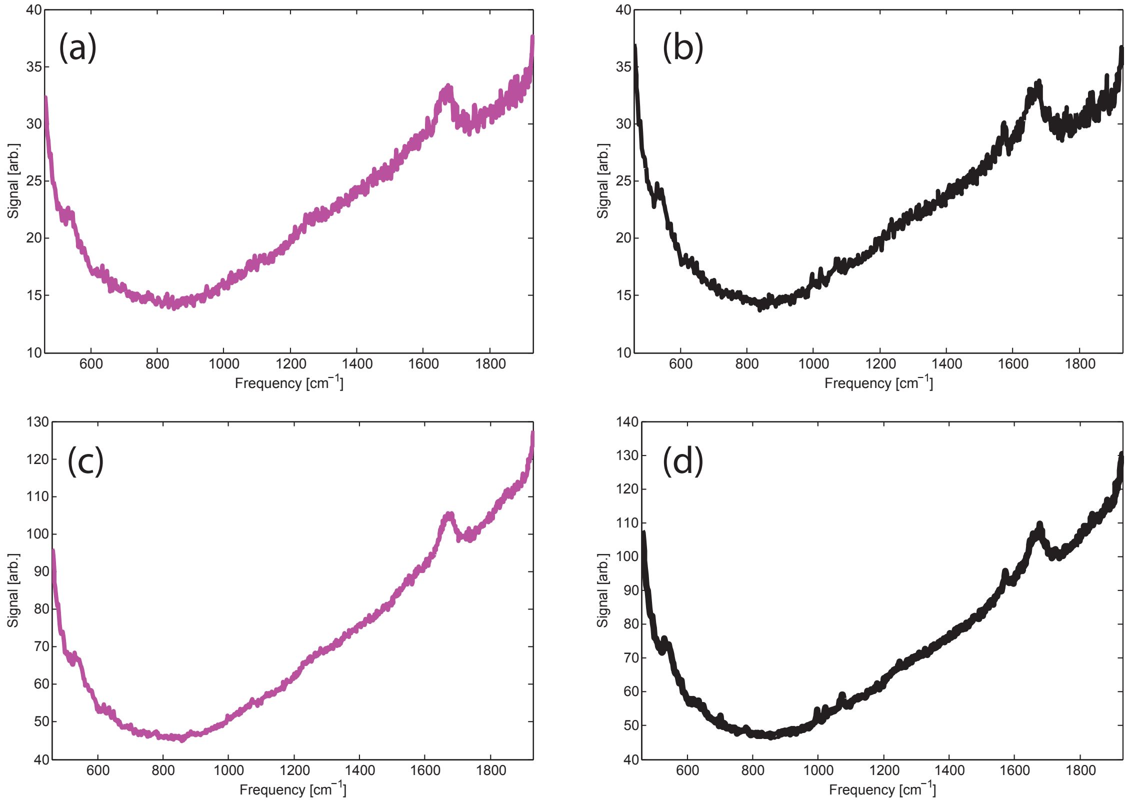

Figure 5.14: Spontaneous Raman data (taken in Morris lab) for benzenethiol adsorbed on flat portion of Klarite® substrate. a) 10 second exposure at spot A. b) 10 second exposure at spot B. c) 30 second exposure at spot A. d) 30 second exposure at spot B.

on the flat gold substrate for comparison.

Figure 5.13 shows surface-enhanced Raman data taken from our sample of benzenethiol adsorbed on Klarite® in the Morris lab. The numbers indicate the locations (1-5) on the Klarite® substrate at which the data is taken. The exposure time for all SERS spectra is 10 seconds. While there are small variations among the Raman signal strengths at the different locations, they are very close overall. To test whether we are seeing enhanced signal based on the structure of the substrate, we repeat the same measurement on the flat gold part of the Klarite® substrate. Figure 5.14 shows the same data taken on a non-structured portion of the gold substrate. Figures 5.14a and 5.14c show data taken at spot A on the Klarite® substrate, with 10 second integration time and 30 second integration time, respectively. Figure 5.14b and 5.14d show the same data taken at spot B, also with 10 second and 30 second integration times, respectively.

Comparing Figure 5.13 and Figure 5.14, it can be seen that a large enhancement factor arises from using the structured substrate. The exact enhancement factor is difficult to quantify, as the Raman modes of interest near 1000 cm^{-1} are essentially buried in noise on the flat gold substrate. Other Raman modes beyond 1600 cm^{-1} appear in the flat gold spectra as much larger than those around 1000 cm^{-1}, while the modes around 1000 cm^{-1} are significantly larger than the 1600 cm^{-1} modes on the nanostructured substrate. This indicates an enhancement factor of at least 100 for the 1600 cm^{-1} modes, with the enhancement factor of the 1000 cm^{-1} modes being much higher. We observe a clear wavelength dependence on enhancement factor, as expected.

Immediately after taking the Raman data in the Morris lab, we brought the samples back to our lab to test with our coherent-Stokes Raman scattering (CSRS) setup described in section 5.4. Figure 5.15 shows the results for different excitation configurations. As in chapter III, we detect the nonresonant CSRS signal using all three

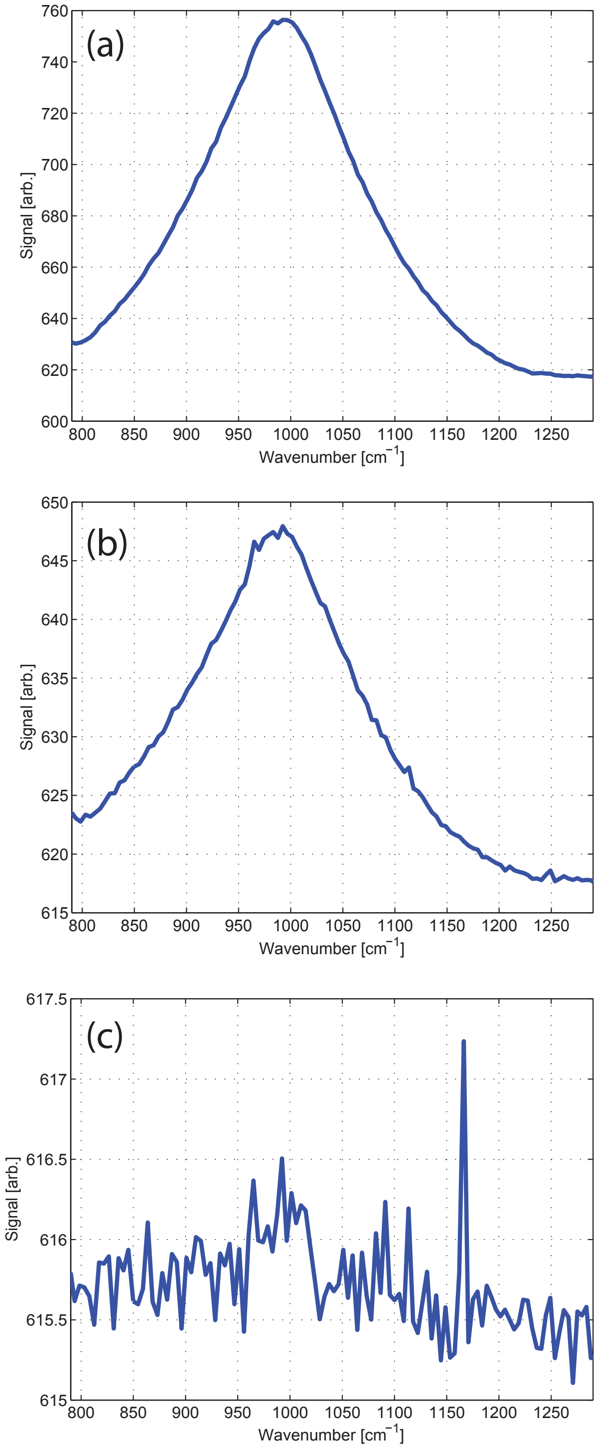

Figure 5.15: Coherent and spontaneous Raman data on nanostructured portion of Klarite®. a) CSRS signal, all three excitation beams coincident in time (nonresonant). Total power: 1.41 mW. b) CSRS signal, probe pulse delayed by 800 fs (resonant). Total power: 1.41 mW. c) Spontaneous Raman signal, probe only. Total power: 0.20 mW.

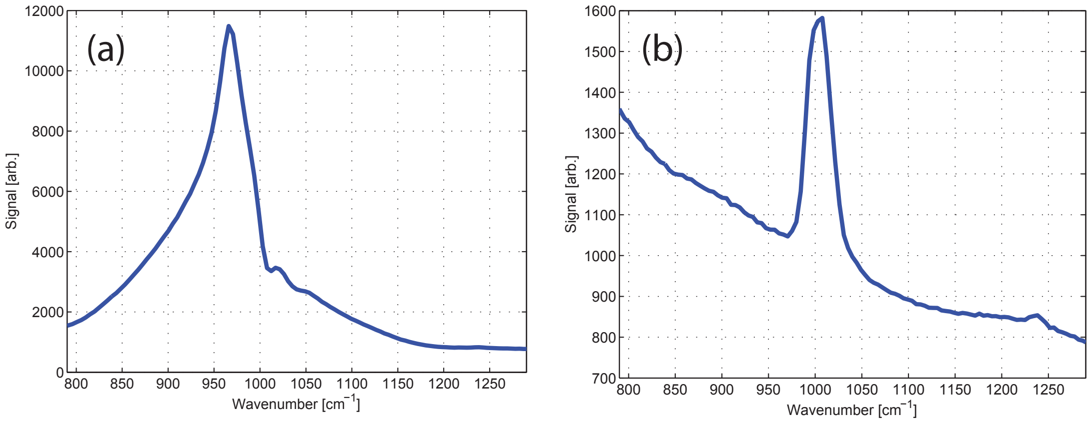

Figure 5.16: a) Nonresonant (no probe delay) and b) resonant (800 fs delay) data in polystyrene, for comparison with data on Klarite®.

excitation beams coincident in time. Figure 5.15a shows the data resulting from this configuration. As expected, the data shows a very broad signal centered at ~ 1000 cm^{-1} corresponding to the ring-breathing mode of benzenethiol. For comparison, Figure 5.16a shows nonresonant signal from pure polystyrene (not on a SERS substrate). On the other hand, adding in an 800 fs delay produces very unexpected results. Figure 5.15b shows the CSRS data for benzenethiol on Klarite® with an 800 fs delay between the pumps and the probe to suppress the nonresonant background. However, the lineshape of the data looks nearly identical to that of the nonresonant signal shown in (a) with a slightly reduced amplitude. For comparison, Figure 5.16b shows the same excitation configuration for pure polystyrene. In the case of polystyrene, the width of the Raman lineshape narrows significantly, matching the linewidth of the probe pulse. The data for benzenethiol on Klarite®, on the other hand, shows no narrowing of the lineshape, indicating fundamentally different dynamics occurring due to the addition of the nano-structured substrate.

Figure 5.15c shows spontaneous Raman data taken with our setup. For this data, the pump pulses were blocked and the probe pulse alone acted as the excitation for spontaneous Raman (i.e. the same scheme used in chapter III). A small bump of Raman signal appears to be barely visible above the noise around 1000 cm^{-1}, although the total signal collected is only (0.4 ± 0.2) counts. The spike at ~ 1170 cm^{-1} is due to an unidentified background that we were unable to suppress, and it is common throughout most of the measurements presented in this section. We can make a rough estimate about the relative signal strengths we should see in our lab compared to the Morris lab based on experimental parameters using the expression for Raman power used in section 3.6 [51]:

$$P_{Raman} = \left(\frac{c}{8\pi}\right) \left|E_{pr}\right|^2 ALN \frac{d\sigma}{d\Omega} \Omega_{coll} \tag{5.9}$$

where E_{pr} is the Raman excitation power (probe power, in this case), L is the interaction length of the sample, A is the cross-sectional area of the excitation region, N is the number density of molecules, $(d\sigma/d\Omega)$ is the differential Raman scattering cross section for the molecule, and Ω_{coll} is the total solid angle angle collected.

The ratio between Raman power measurements in our lab (O) and the Morris lab (M) is thus:

$$\frac{P_{Raman}^{(M)}}{P_{Raman}^{(O)}} = \frac{\left(\frac{c}{8\pi}\right) \left|E_{pr}^{(M)}\right|^2 A^{(M)} L^{(M)} N^{(M)} \frac{d\sigma}{d\Omega}^{(M)} \Omega_{coll}^{(M)}}{\left(\frac{c}{8\pi}\right) \left|E_{pr}^{(O)}\right|^2 A^{(O)} L^{(O)} N^{(O)} \frac{d\sigma}{d\Omega}^{(O)} \Omega_{coll}^{(O)}} \tag{5.10}$$

For both experiments, the interaction length L is identical because the depth is a single monolayer in each case. The consistent density of the self-assembled monolayer also ensures that the number density of molecules N is equal for both setups. The differential Raman scattering cross section $(d\sigma/d\Omega)$ is unique to the analyte, rather than the setup, and will be identical for both experiments. After these terms and the constants in equation 5.10 cancel, we are left with:

$$\frac{P_{Raman}^{(M)}}{P_{Raman}^{(O)}} = \frac{\left|E_{pr}^{(M)}\right|^2 A^{(M)} \Omega_{coll}^{(M)}}{\left|E_{pr}^{(O)}\right|^2 A^{(O)} \Omega_{coll}^{(O)}} \tag{5.11}$$

We can estimate each of these quantities individually for both experimental setups, starting with the excitation intensity $|E_{pr}|^2$:

$$\left|E_{pr}^{(M)}\right|^2 \sim \frac{P}{w \times h} = \frac{2(10.0mW)}{10\mu m \times 100\mu m} = 1.0 \times 10^4 W/cm^2 \tag{5.12}$$

$$\left|E_{pr}^{(O)}\right|^2 \sim \frac{2P}{\pi w^2} = \frac{2(0.2mW)}{\pi(664.5nm)^2} = 2.9 \times 10^4 W/cm^2 \tag{5.13}$$

where the extra factor of 2 in the numerator of $\left|E_{pr}^{(O)}\right|^2$ is based on focusing a Gaussian beam.

Similarly, we can calculate the cross-sectional area excited on Klarite® for each experiment:

$$A^{(M)} = w \times h = 10\mu m \times 100\mu m = 1000\mu m^2 \tag{5.14}$$

$$A^{(O)} = \pi w^2 = \pi(664.5nm)^2 = 1.39\mu m^2 \tag{5.15}$$

The collection factor Ω_{coll} is a term that contains all of the information about the differences between signal collection for the two measurements. Using the relationship $\Omega_{coll}(N.A.) \approx 2\pi \left\{1 - \cos\left[\sin^{-1}(N.A.)\right]\right\}$ where $N.A.$ is the numerical aperture of the collection objective, we can write:

$$\begin{aligned}\Omega_{coll}^{(M)} &= \Omega(N.A. = 0.75) \times T \times SE \times QE \times F \\ &= 2.13 \times 10s \times 0.5 \times 0.6 \times \left(\frac{1}{91}\right) && = 0.070 \qquad (5.16)\\ \Omega_{coll}^{(O)} &= \Omega(N.A. = 0.40) \times T \times SE \times QE \times F \\ &= 0.53 \times 0.1s \times 0.5 \times 0.25 \times 1 && = 0.007 \qquad (5.17)\end{aligned}$$

where Ω is solid angle collected, T is the exposure time in seconds, SE is the transmission efficiency of the spectrometer, QE is the quantum efficiency of the CCD camera, and F is the fraction of pixels CCD pixels used in a spectrum relative to the total number of CCD pixels with Raman signal on them. The CCD in the Morris lab has a total of 91 rows of pixels that are illuminated with Raman signal, while the output spectrum is looking at a single row. To get the total amount of signal generated, this factor accounts for the other 90 rows of pixels that have signal on them. The spectra from our lab have the signal from all rows integrated to provide each single spectrum.

Plugging these numbers back into equation 5.11, we get the expected ratio:

$$\begin{aligned}\frac{P^{(M)}_{Raman}}{P^{(O)}_{Raman}} &= \frac{\left|E^{(M)}_{pr}\right|^2}{\left|E^{(O)}_{pr}\right|^2} \times \frac{A^{(M)}}{A^{(O)}} \times \frac{\Omega^{(M)}_{coll}}{\Omega^{(O)}_{coll}} \\ &= \frac{1.0 \times 10^4 W/cm^2}{2.9 \times 10^4 W/cm^2} \times \frac{1000 \mu m^2}{1.39 \mu m^2} \times \frac{0.070}{0.007} \sim 2,500 \end{aligned} \tag{5.18}$$

Based on this estimate, we could expect approximately 2,500 times larger signal in the spectra from the Morris lab compared to those in our lab. There will be an additional factor due to the enhancement of the difference in excitation efficiency, but this will bias the result further to the advantage of the Morris lab setup. This shows that the signal we will see in our lab for our excitation and collection conditions will likely be difficult to detect above the noise (less than one CCD count per spectrum), as the maximum signal we see in the Morris lab is $\sim$ 1000 CCD counts. In this context, Figure 5.15c is consistent with our expectations.

Because of the unexpected results when attempting time-delay CSRS (Figure 5.15b), we have investigated the nature of the signal in this configuration. Figure 5.17 shows the spectra obtained for various combinations of pump and probe pulses.Figure 5.17a shows the resulting spectrum when all three excitation pulses are used. Similar to what was seen in Figure 5.15a, a broad spectral feature centered at the Stokes frequency (1000 cm^{-1}) is apparent. Figure 5.17b shows the spectrum when only the probe beam is incident on the sample. This corresponds to the case similar to Figure 5.15b of spontaneous Raman excitation. Again, there is little or no detectable signal

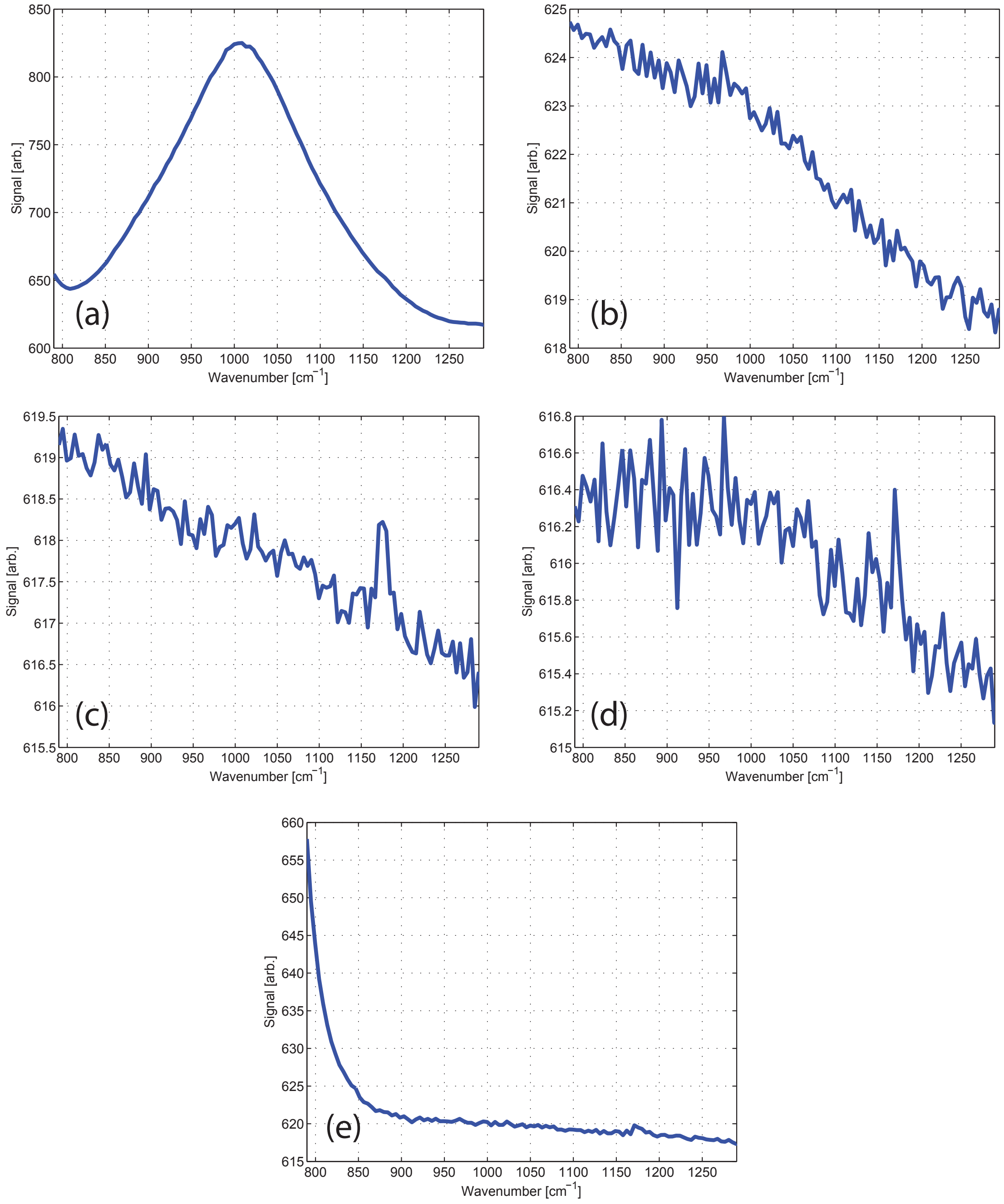

Figure 5.17: Surface-enhanced CSRS data for various combinations of pump and probe beams. a) Both pumps and probe beams. b) Probe beam only. c) Both pump beams, no probe. d) Blue pump and probe only. e) Red pump and probe only.

above background, as predicted by the preceding calculation. Figure 5.17c shows the case with both pump beams incident, with the probe beam blocked. The only peak is around 1170 cm^{-1}, corresponding to the background peak discussed previously. No Raman signal is detected. A similar result is seen in Figure 5.17d, in which the red pump is blocked. With the blue pump blocked (Figure 5.17e), no 1000 cm^{-1} signal is seen, with the only spectral features being the background peak at 1170 cm^{-1} and some low-frequency leakage ($\lesssim$ 850 cm^{-1}) due to the background transmitted beyond the spectral edge of the long-pass filter.

The data from Figure 5.17 suggests that the signal peak we are seeing is indeed a four-wave mixing peak. The only combination of excitation beams that produces the signal at 1000 cm^{-1} is both pumps and probe. However, the data from Figure 5.15 suggests that the four-wave mixing signal is different in nature than the CSRS signal we observe in pure samples with no SERS substrate (i.e. polystyrene data in Figure 5.16) based on the broad peak retention despite delaying the probe pulse by 800 femtoseconds. This result indicates that the signal we see on these substrates is not the same nonresonant CSRS background signal we see for pure samples.

Figure 5.18 shows the four-wave mixing signal as a function of probe pulse delay for benzenethiol on Klarite®. Figure 5.18a shows the usual signal when all three beams arrive concurrently. Figure 5.18b shows the spectrum with the probe pulse delayed by 800 fs. As seen previously, the signal decreases in amplitude, but the linewidth remains the same, indicating that we are not suppressing nonresonant background in favor of resonant Raman signal. Figure 5.18c shows the same data for a probe delay of 1600 fs. The broad signal at 1000 cm^{-1} is still visible without any signs of lineshape narrowing. When the probe delay is extended to 2400 fs (Figure 5.18d) and 3200 fs (Figure 5.18e), the amplitude has decreased significantly to the point that it is difficult to distinguish above background, indicating that the dynamics we are observing occur on the timescale of a couple of picoseconds.

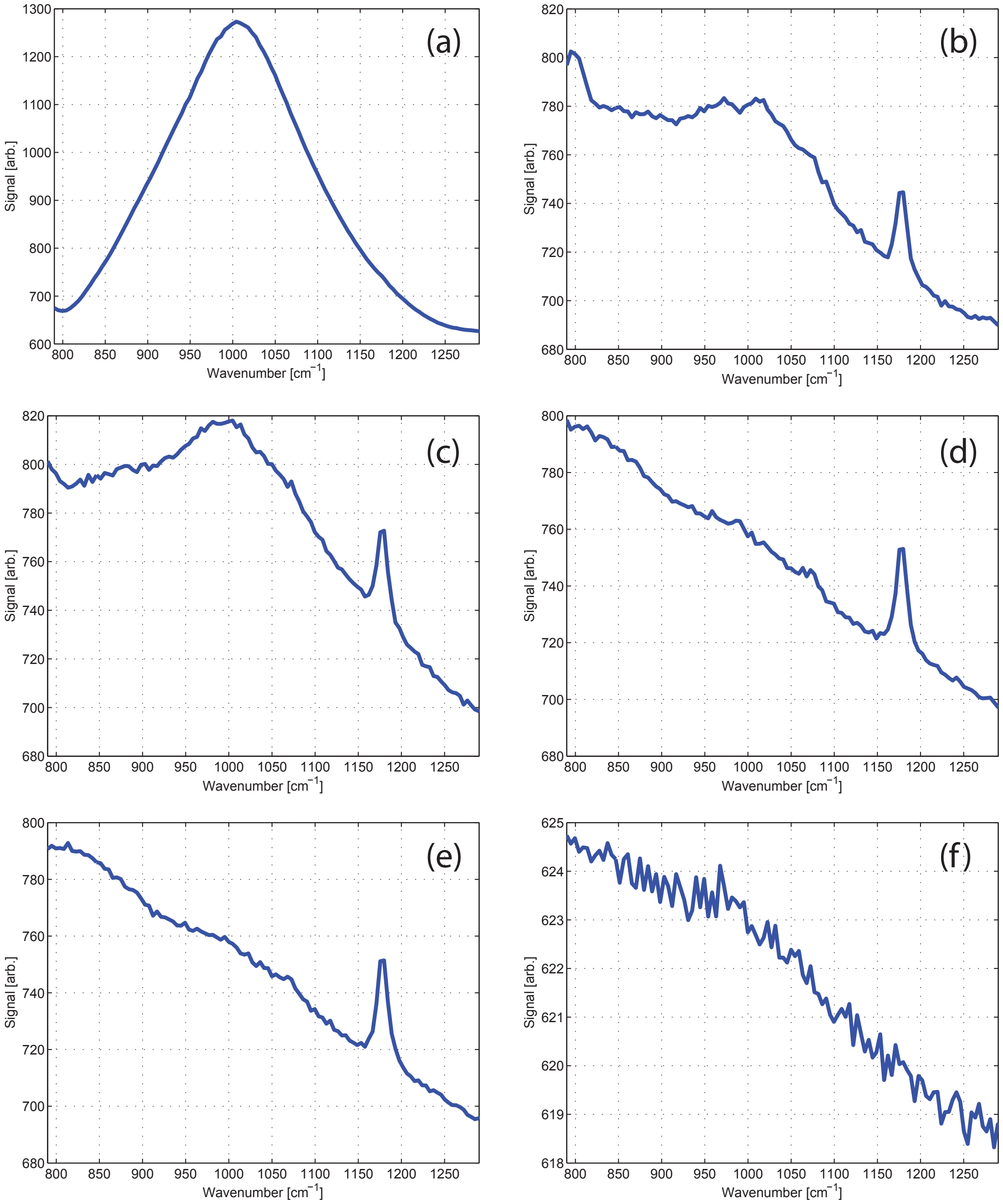

Figure 5.18: Surface-enhanced CSRS data from benzenethiol on Klarite® substrate for various probe delay times. a) 0 fs delay. b) 800 fs delay. c) 1600 fs delay. d) 2400 fs delay. e) 1800 fs delay. f) probe only. Peaks at 1170 cm^{-1} are unidentified background. Excitation conditions are 1.9 mW blue pump, 13.2 mW red pump, and 2.8 mW probe, with the laser repetition rate set to 7.5 MHz. 3 second integration time is used.

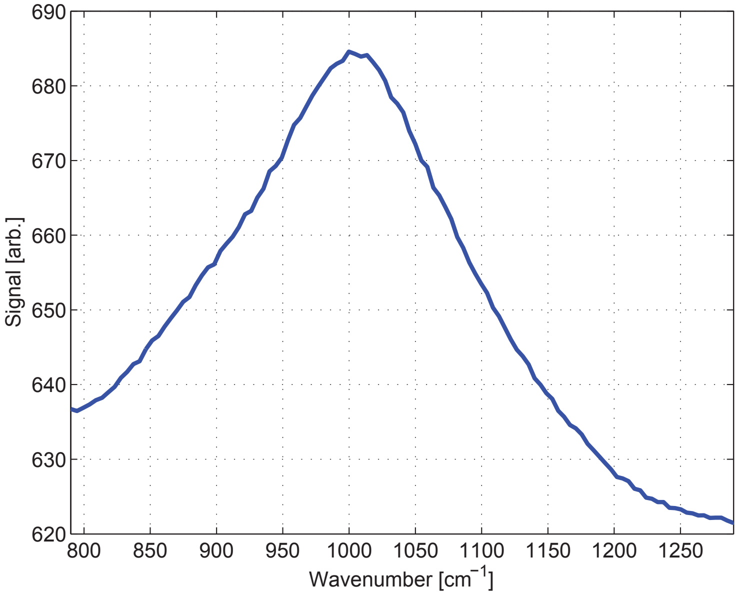

Figure 5.19: Surface-enhanced CSRS data from Klarite® substrate without benzenethiol. Excitation conditions are 1.9 mW blue pump, 13.2 mW red pump, and 2.8 mW probe, with the laser repetition rate set to 7.5 MHz. 100 ms integration time is used.

One possible explanation of this data is found in the work of Novotny, et al., who have recorded nonlinear four-wave mixing on the nano-structured gold substrates [52, 53]. They first demonstrated the nonlinear excitations of surface plasmons on a gold film by four-wave mixing, inducing a nonlinear polarization at frequency $\omega_{4wm} = 2\omega_1 - \omega_2$, which in turn excited the surface plasmons at the same frequency [52]. Similarly, in 2010, they reported on a very strong surface-enhanced nonlinear response from nanostructured gold surfaces [53]. They were able to detected emitted four-wave mixing radiation at a specific angle based on the incidence angles of the excitation beams. Notably, they explain that the nanostructured surface aids in the in and out coupling of radiation to evanescent waves generated by four-wave mixing in the metal surface. It is important to note that while this is considered an undesired background in our experiment, other groups have successfully used four-wave mixing on metal nanostructures for imaging [54].

These results are consistent with the data presented in this chapter. We failed to detect signal on the flat (non-nanostructured) section of Klarite®, but the four-wave mixing signal was readily detected on the structured portion of the substrate. This is consistent with the assertion that the nanostructure aids in coupling radiation in and out of the substrate. While the Novotny group detected an angular dependence to the emitted radiation, they used long focal length (50 mm) lenses for excitation and signal collection [53]. We use an objective lens (NA 0.4) for our measurements, meaning that we excite and collect radiation at a large range of angles. In this configuration, we can be expected to detect the four-wave mixing signal due to the large angular collection efficiency of our setup. To test whether we are detecting radiation from the benzenethiol or the Klarite® substrate itself, we take the same four-wave mixing measurements on a Klarite® substrate without benzenethiol adsorbed to the surface. Figure 5.19 shows the four-wave mixing signal from Klarite® without benzenethiol adsorbed to the surface, indicating that the signal detected is indeed a product of the substrate, rather than the analyte.

Our measurements of signal dynamics are also consistent with many recent studies of surface plasmon lifetimes. While the distribution of surface plasmon lifetimes is very broad and highly dependent on the geometry of the nanoscaled structures, many experiments have demonstrated picosecond-scale surface plasmon lifetimes in a variety of structures. Lowman's group used transient absorption to observe electron relaxation dynamics in isolated and aggregated hollow gold nanospheres, finding short and long lifetime components of (300 ± 50) fs and (730 ± 140) fs, respectively [55]. Popp's group also used transient absorption to study the surface plasmon dynamics on nanorhomb and nanosquare SERS substrates, similarly finding a surface plasmon decay lifetime of 1.1 picoseconds [56]. Finally, El-Sayed's group detected visible photoluminescence from gold nanoparticles (nanospheres and nanorods) using time-resolved fluorescence upconversion spectroscopy and used transient absorption to measure the ultrafast dynamics of nanospheres [57]. They also found a decay on the timescale of picoseconds ($\tau_3 \approx 1.5$ ps). These timescales are consistent with the timescales measured in our experiment, confirming that we are likely seeing four-wave mixing on the nanostructured substrate of Klarite® that excites localized surface plasmons, followed by the subsequent emission of radiation coupled via the nanostructure and decaying on the timescale of the surface plasmon lifetime.

The SECARS study on Klarite® substrates published during the writing of this dissertation finds an enhancement of 10^3 for SECARS over SERS for equal excitation power [28]. In our case, we measure (0.4 ± 0.2) CCD counts for SERS using 0.2 mW excitation power (see Figure 5.15c). This level of signal is consistent with what we expect given our SERS measurements taken in the Morris lab on the same sample. If the enhancement factor of 10^3 for SECARS over SERS measured by Steuwe we al. holds, we could expect to see a few thousand counts of SECARS signal on Klarite® . As Figure 5.15a shows, we detect only just over a hundred counts of total signal (including the dominant background), falling about an order of magnitude short of what we expect using their reported enhancements. It is difficult to compare the lineshapes of the results of Steuwe et al. to our work, primarily due to their > 50 cm^{-1} spectral resolution [28]. The omission of surface-enhanced spontaneous Raman data from their results also makes it difficult to verify the Raman peak locations relative to the peak locations in the SECARS spectra. We note that our experiments were performed at considerably lower excitation conditions than theirs. While they claim to have used a polarization scheme to remove background signals, they provide no detail about how this was accomplished. Further studies on Klarite® should offer a clearer picture of what kind of enhancements are possible on the substrate and whether narrow Raman lineshapes can be achieved through suppression of the broad four-wave mixing background.

5.6 Conclusions and Future Directions

We have successfully taken early steps toward improving sensitivity of Raman spectroscopy in our lab using surface-enhanced effects in nanostructured substrates. Our experiments here have shown spontaneous Raman measurements taken on structured Klarite® substrates show significant enhancement over the same measurements taken on flat gold portions of the same substrate. In attempting to perform spectral-domain CSRS on the same samples, we have encountered an unexpected source of signal likely related to four-wave mixing excitation of surface plasmons that subsequently couple to radiation through nanostructures on the surface of the gold substrate. Lifetime measurements are consistent with this hypothesis, matching lifetime measurements of surface plasmons reported by other groups. Measurements on plain Klarite® without adsorbed analyte further support this conclusion. This background ultimately makes it difficult to perform spectral-domain coherent Raman measurements on the surface of such substrates in this experimental configuration.

Future directions for similar experiments include testing polarization dependence of the emitted radiation. If there is a strong polarization dependence on the emitted radiation, surface-enhanced CSRS may still be possible by blocking the four-wave mixing signal due to the gold surface, similar to polarization-based nonresonant background suppression techniques used in CARS [58]. Other substrates should also be explored to test whether the properties of the emission observed here are unique to this substrate. Being able to utilize the high-enhancement factor in many SERS substrates may pave the way for high-sensitivity measurements of low-concentration biological analytes.

References

[1] E. J. Blackie, E. C. Le Ru, M. Meyer, and P. G. Etchegoin. Surface Enhanced Raman Scattering Enhancement Factors: A Comprehensive Study. *J. Phys. Chem. C*, 111:1374–13803, 2007.

[2] E. J. Blackie, E. C. Le Ru, and P. G. Etchegoin. Single-Molecule Surface-Enhanced Raman Spectroscopy of Nonresonant Molecules. *Journal of the American Chemical Society*, 131:14466–14472, 2009.

[3] J. T. Golab, J. R. Sprague, K. T. Carron, G. C. Schatz, and R. P. van Duyne. A surface enhanced hyper-Raman scattering study of pyridine adsorbed onto silver: Experiment and theory. *Journal of Chemical Physics*, 88:7942–7951, 1988.

[4] S. M. Nie and S. R. Emery. Probing single molecules and single nanoparticles by surface-enhanced Raman scattering. *Science*, 275:1102–1106, 1997.

[5] K. Kneipp, Y. Wang, H. Kneipp, L. T. Perelman, and I. Itzkan. Single molecule detection using surface-enhanced Raman scattering (SERS). *Physical Review Letters*, 78:1667–1670, 1997.

[6] P. L. Stiles, J. A. Dieringer, N. C. Shah, and R. P. van Duyne. Surface-Enhanced Raman Spectroscopy. *Annual Review of Analytical Chemistry*, 1:601–626, 2008.

[7] J. I. Gersten and A. Nitzan. Electromagnetic Theory of Enhanced Raman Scattering by Molecules Adsorbed on Rough Surfaces. *Journal of Chemical Physics*, 73:3023, 1980.

[8] J. I. Gersten. The Effect of Surface Roughness of Surface Enhanced Raman Scattering. *Journal of Chemical Physics*, 72:5779, 1980.

[9] J. I. Gersten. Rayleigh, Mie, and Raman-scattering by molecules adsorbed on rough surfaces. *Journal of Chemical Physics*, 72:5780, 1980.

[10] J. I. Gersten and A. Nitzan. Spectroscopic Properties of Molecules Interacting with Small Dielectric Particles. *Journal of Chemical Physics*, 75:1139–1152, 1981.

[11] S. L. McCall, P. M. Platzman, and P. A. Wolff. Surface Enhanced Raman Scattering. *Physics Letters A*, 77:381, 1980.

[12] S. L. McCall and P. M. Platzman. Raman-scattering from Chemisorbed Molecules at Surfaces. *Physicsal Review B*, 22:1660–1662, 1980.

[13] M. Kerker. Resonances in Electromagnetic Scattering by Objects with Negative Absorption. *Applied Optics*, 18:1180–1189, 1979.

[14] M. Kerker, D. S. Wang, and H. W. Chew. Surface Enhanced Raman Scattering (SERS) by Molecules Adsorbed at Spherical Particles: Errata. *Applied Optics*, 19:4159, 1980.

[15] D. S. Wang and M. Kerker. Enhanced Raman-scattering by Molecules Adsorbed at the Surface of Colloidal Spheroids. *Physical Review B*, 24:1777–1790, 1981.

[16] D. S. Wang and M. Kerker. Absorption and Luminescence of Dye-coated Silver and Gold Particles. *Physical Review B*, 25:2433–2449, 1982.

[17] M. Kerker, O. Siiman, and D. S. Wang. Effect of Aggregates on Extinction and Surface-enhanced Raman-scattering Spectra of Colloidal Silver. *Journal of Physical Chemistry*, 88:3168–3170, 1984.

[18] A. Campion and P. Kambhampati. Surface-enhanced Raman scattering. *Chemical Society Reviews*, 27:241, 1998.

[19] C. K. Chen, A. R. B. de Castro, F. deMartini, and Y. R. Shen. Surface coherent anti-Stokes Raman spectroscopy. *Physical Review Letters*, 43:946–949, 1979.

[20] Y. R. Shen. *The Principles of Nonlinear Optics.* Wiley Interscience, 2003.

[21] M. Fleischmann, P. J. Hendra, and A. J. McQuillan. Raman spectra of pyridine adsorbed at a silver electrode. *Chemical Physics Letters*, 26:163–166, 1974.

[22] D. L. Jeanmaire and R. P. van Duyne. Surface Raman Spectroelectrochemistry Part I: Heterocyclic, Aromatic, and Aliphatic Amines Adsorbed on the Anodized Silver Electrode. *J. Electroanal. Chem.*, 84:1–20, 1977.

[23] M. G. Albrecht and J. A. Creighton. Anomalously Intense Raman Spectra of Pyridine at a Silver Electrode. *Journal of the American Chemical Society*, 99:5215–5217, 1977.

[24] E. J. Liang, A. Weippert, J. M. Funk, A. Materny, and W. Kiefer. Experimental observation of surface-enhanced coherent anti-Stokes Raman scattering. *Chemical Physics Letters*, 227:115–120, 1994.

[25] T. W. Koo, S. Chan, and A. A. Berlin. Single-molecule detection of biomolecules by surface-enhanced coherent anti-Stokes Raman scattering. *Optics Letters*, 30:1024–1026, 2005.

[26] C. J. Addison, S. O. Konorov, A. G. Brolo, M. W. Blades, and R. F. B. Turner. Tuning gold nanoparticle self-assembly for optimum coherent anti-Stokes Raman scattering and second harmonic generation response. *Journal of Physical Chemistry C*, 113:3586–3592, 2009.

[27] V. Namboodiri, M. Namboodiri, G. I. C. Diaz, M. Oppermann, G. Flachenecker, and A. Materny. Surface-enhanced femtosecond CARS spectroscopy (SE-CARS) on pyridine. *Vibrational Spectroscopy*, 56:9–12, 2011.

[28] C. Steuwe, C. F. Kaminski, J. J. Baumberg, and S. Mahajan. Surface enhanced coherent anti-Stokes Raman scattering on nanostructured gold surfaces. *Nano Letters*, Article ASAP.

[29] K. Kneipp, Y. Wang, and H. Kneipp. Population pumping of excited vibrational states by spontaneous surface-enhanced Raman scattering. *Physical Review Letters*, 76:2444–2447, 1996.

[30] K. Kneipp, H. Kneipp, and R. Manoharan. Extremely large enhancement factors in surface-enhanced Raman scattering for molecules on colloidal gold clusters. *Applied Spectroscopy*, 52:1493–1497, 1998.

[31] K. Kneipp, H. Kneipp, and R. Manoharan. Near-infrared surface-enhanced Raman scattering can detect single molecules and observe 'hot' vibrational transitions. *Journal of Raman Spectroscopy*, 29:743–747, 1998.

[32] K. Kneipp, H. Kneipp, and V. B. Kartha. Detection and identification of a single DNA base molecule using surface-enhanced Raman scattering (SERS). *Physical Review E*, 57:R6281–R6284, 1998.

[33] K. Kneipp, H. Kneipp, and I. Itzkan. Surface-enhanced nonlinear Raman scattering at the single-molecule level. *Chemical Physics*, 247:155–162, 1999.

[34] J. T. Krug, G. D. Wang, S. R. Emory, and S. M. Nie. Efficient Raman enhancement and intermittent light emission observed in single gold nanocrystals. *Journal of the American Chemical Society*, 121:9208–9214, 1999.

[35] W. A. Lyon and S. M. Nie. Confinement and detection of single molecules in submicrometer channels. *Analytical Chemistry*, 69:3400–3405, 1997.

[36] W. E. Doering and S. M. Nie. Single-molecule and single-nanoparticle SERS: Examining the roles of surface active sites and chemical enhancement. *Journal of Physical Chemistry B*, 106:311–317, 2002.

[37] D. J. Maxwell, S. R. Emory, and S. M. Nie. Nanostructured thin-film materials with surface-enhanced optical properties. *Chemistry of Materials*, 13:1082–1088, 2001.

[38] A. Otto. Excitation of nonradiative surface plasma waves in silver by method of frustrated total reflection. *Zeitschrift fur Physik*, 216:398, 1968.

[39] E. Kretschmann. Determination of optical constants of metals by excitation of surface plasmons. *Zeitschrift fur Physik*, 241:313, 1971.

[40] W. Zhang, X. Cui, B. Yeo, T. Schmid, C. Hafner, and R. Zenobi. Nanoscale roughness on metal surfaces can increase tip-enhanced Raman scattering by an order of magnitude. *Nano Letters*, 7:1401–1405, 2007.

[41] N. M. B. Perney, J. J. Baumberg, M. E. Zoorob, M. D. B. Charlton, S. Mahnkopf, and C. M. Netti. Tuning localized plasmons in nanostructured substrates for surface-enhanced Raman scattering. *Optics Express*, 14:847–857, 2006.

[42] Renishaw Diagnostics. Klarite - Substrates for surface enhanced Raman scattering. Technical report, Renishaw Diagnostics, 2010.

[43] W. Zhang, T. Schmid, B. Yeo, and R. Zenobi. Near-field heating, annealing, and signal loss in tip-enhanced Raman spectroscopy. *Journal of Physical Chemistry C*, 112:2104–2108, 2008.

[44] T. Ichimura, N. Hayazawa, M. Hashimoto, T. Inouye, and S. Kawata. Tip-enhanced coherent anti-Stokes Raman scattering for vibrational nano-imaging. *Physical Review Letters*, 92:220801, 2004.

[45] A. M. Weiner, D. E. Leaird, G. P. Wiederrecht, and K. A. Nelson. Femtosecond multi-pulse impulsive stimulated Raman-scattering spectroscopy. *Journal of the Optical Society of America B - Optical Physics*, 8:1264–1275, 1991.

[46] V. V. Lozovoy, I. Pastirk, and M. Dantus. Multiphoton intrapulse interference. IV. Ultrashort laser pulse spectral phase characterization and compensation. *Optics Letters*, 29:775–777, 2004.

[47] B. W. Xu, J. M. Gunn, J. M. Dela Cruz, V. V. Lozovoy, and M. Dantus. Quantitative investigation of the multiphoton intrapulse interference phase scan method for simultaneous phase measurement and compensation of femtosecond laser pulses. *Journal of the Optical Society of America B - Optical Physics*, 23:750–759, 2006.

[48] Sigma-Aldrich Co. Benzenethiol Raman spectrum, 2011.

[49] L. Wan, M. Terashima, H. Noda, and M. Osawa. Molecular orienatation and ordered structure of benzenethiol adsorbed on gold (111). *Journal of Physical Chemistry B*, 104:3563–3569, 2000.

[50] M. Cui. *Coherent Raman scattering: applications in imaging and sensing.* PhD thesis, University of Michigan, 2009.

[51] W. M. Tolles, J. W. Nibler, J. R. McDonald, and A. B. Harvey. Review of theory and application of coherent anti-Stokes Raman spectroscopy (CARS). *Applied Spectroscopy*, 31(4):253–271, 1977.

[52] S. Palomba and L. Novotny. Nonlinear Excitation of Surface Plasmon Polaritons by Four-Wave Mixing. *Physical Review Letters*, 101:056802, 2008.

[53] J. Renger, R. Quidant, N. van Hulst, and L. Novotny. Surface-enhanced Nonlinear Four-Wave Mixing. *Physical Review Letters*, 104:046803, 2010.

[54] Y. Wang, C. Lin, A. Nikolaenko, V. Raghunathan, and E. O. Potma. Four-wave mixing microscopy of nanostructures. *Advances in Optics and Photonics*, 3:1–52, 2011.

[55] K. L. Knappenberger, Jr., A. M. Schwartzberg, A. Dowgiallo, and C. A. Lowman. Electronic Relaxation Dynamics in Isolated and Aggregated Hollow Gold Nanospheres. *Journal of the American Chemical Society*, 131:13892, 2009.

[56] D. Cialla, R. Siebert, U. Huebner, R. Moeller, H. Schneidewind, R. Matteis, J. Petschulat, A. Tuennermann, T. Pertsch, B. Dietzek, and J. Popp. Ultrafast plasmon dynamics and evanescent field distribution of reproducible surface-enhanced Raman-scattering substrates. *Analytical and Bioanalytical Chemistry*, 394:1811–1818, 2009.

[57] O. Varnavski, T. Goodson, M. Mohamed, and M. El-Sayed. Femtosecond excitation dynamics in gold nanospheres and nanorods. *Physical Review B*, 72:235405, 2005.

[58] J. X. Cheng, L. D. Book, and X. S. Xie. Polarization coherent anti-Stokes Raman scattering microscopy. *Optics Letters*, 26(17):1341–1343, Sep 1 2001.

CHAPTER VI

Conclusion

In this thesis, we have presented a variety of techniques for Raman spectroscopy and microscopy with the goal of finding methods with high sensitivity for imaging and sensing of biological samples. The most popular coherent Raman method, coherent anti-Stokes Raman spectroscopy (CARS) has long been touted as the sensible technique for biological imaging because of its purported orders of magnitude signal advantage over spontaneous Raman scattering. We have shown that under the low-concentration, low-excitation power conditions encountered in biological imaging, spontaneous Raman often provides higher signal levels than coherent anti-Stokes Raman scattering [1–3]. Spontaneous Raman has a linear dependence on concentration and power compared to the quadratic and cubic dependence of CARS on concentration and power, respectively. This gives rise to a critical power at which the two methods provide equal signal levels, given a specific sample concentration. Below this power, spontaneous Raman methods give higher signal level. As shown in **Chapter III**, this critical power is often at power and concentration levels used in biological imaging.

While signal level is one of the most important aspects in choosing a particular technique for a Raman imaging application, other factors are important as well. For example, coherent Raman methods will provide automatic 3D sectioning in imaging applications, owing to the multiphoton nature of the process. In applications where out-of-focus signal will be a major problem for producing images, this is an important factor. While this can be mitigated with spontaneous Raman using a confocal microscopy technique, it carries with it a concomitant loss of signal. Because its signal is blue-shifted with respect to the excitation wavelengths, CARS has the advantage of avoiding most fluorescence background (although multiphoton fluorescence can still be a problem). On the other hand, spontaneous Raman automatically provides high-resolution broadband spectra without the presence of a nonresonant background, while CARS is limited by the same nonresonant background. CW lasers can provide experimental simplicity for spontaneous Raman experiments, as well as significantly reducing laser-induced sample photodamage. All of these considerations must be taken into account when choosing the Raman technique for a particular imaging application.

In **Chapter IV**, we have demonstrated the first multiplexed Raman-induced Kerr effect microscopy experiment [4]. Using a narrowband fiber laser and a continuum generated by photonic crystal fiber, we have shown the ability to get high-resolution spectra in a variety of materials with low background levels. The setup is designed such that it is easy to switch between Raman-induced Kerr effect spectroscopy (RIKES) and femtosecond stimulated Raman scattering spectroscopy (FSRS) for direct comparison of the two methods without any disturbance to the experimental setup or sample position. For samples in solution, we have shown that RIKES provides a higher signal to noise ratio than FSRS under the same excitation conditions. For Raman imaging of polystyrene bead samples, we have shown that RIKES provides higher signal to noise when implemented with a chopping scheme to reduce the effect of the birefringent background. For samples with high birefringence, the signal to noise advantages of RIKES are mitigated. In real-world imaging applications, the relative S/N ratio of the two methods depends highly on the particular sample being studied, making knowledge of the sample's birefringence properties vital when deciding whether to perform imaging using RIKES or FSRS.

With the discovery of surface-enhanced effects in Raman scattering, a large field was born based on increasing the enhancement and reproducibility of Raman signals on nanostructured metal surfaces. Small, sub-wavelength nanostructures on the surface of metal films have been used to enhance Raman scattering signals by several orders of magnitude. Metal nanospheres and nanorods have been used in similar fashion. In **Chapter V**, we have performed studies of surface-enhanced effects for spontaneous and coherent Raman techniques. Using the commercial surface-enhanced Raman scattering (SERS) substrate Klarite®, we have measured large enhancement of spontaneous Raman signals with inverted pyramid nanostructures on the surface of gold films. Using the same sample with the CSRS technique used in chapter III, we have encountered a large four-wave mixing background that appears to be independent of the analyze (in our case, benzenethiol) adsorbed to the surface of the Klarite®. Measurements on blank Klarite® support this hypothesis, indicating that we are likely seeing four-wave mixing radiation coupled to the nanostructures on the substrate itself. This makes spectra detection of SECARS difficult. To perform coherent Raman detection on the substrate, methods of suppressing this four-wave mixing background must be developed.

6.1 Future Directions

While the work presented here has made significant strides towards improving Raman sensitivity with the ultimate goal of high-sensitivity biological imaging, there are many future directions to take to improve Raman methods for imaging and sensing. The results for our coherent versus spontaneous Raman experiment are very specific to the focusing conditions, laser pulse width, wavelength, and laser repetition rate of our experiment. An important step to take next is to perform a similar comparison using picosecond pulses and at longer wavelengths (where photodamage limits may be different). While picosecond pulses do not offer the ability to probe a broad bandwidth of Raman vibrational modes, they are commonly used in single-mode imaging applications. Because video rate imaging currently relies on the excitation of only a single Raman band (multiplex detectors are too slow to perform video-rate imaging), picosecond pulses are often used in these applications for their narrow bandwidth and long pulse length, which mitigates sample photodamage by offering lower peak intensities. We expect similar conclusions for picosecond pulses, implying that video-rate spontaneous Raman imaging may be possible if restricted to imaging single strong Raman modes such as the C-H stretch.

The next step in future RIKES experiments is to perform similar imaging techniques on biologically interesting samples (tissue, etc.). RIKES imaging performed on such samples will provide information about the feasibility of the technique in real-world imaging applications. If the birefringence induced on the probe pulse is too high in tissue, FSRS will likely be the method of choice as it is insensitive to the birefringence of the sample. On the other hand, if the birefringence is not a problem in such samples, RIKES can be readily implemented in many of the clinical applications currently occupied by coherent anti-Stokes Raman scattering microscopy and stimulated Raman scattering microscopy. Potential improvements to the RIKES experiment would be the implementation of a lock-in camera to perform high-speed multiplex imaging. A balanced heterodyne detection scheme could also improve sensitivity for RIKES imaging.

Future experiments on SERS substrates should involve the investigation of the four-wave mixing background we encountered in trying to perform SECARS. The background appears to be long-lived compared to the nonresonant background of CARS, making the time-delay CSRS implementation of our setup ineffective. If this background can be suppressed using polarization techniques or other methods, SE-

CARS may be able to be performed in the spectral domain. Future studies should include an experimental setup that can be conveniently switched between coherent and spontaneous Raman excitation for direct comparison on SERS substrates, similar to our setup implemented in **Chapter III**. The experiments should also be repeated on a variety of other SERS substrates and analytes. If the four-wave mixing signals from the substrate can be fully understood and suppressed, surface-enhanced CARS may be extremely useful in the detection of biological samples, particularly those of extremely low concentration. Ultimately, it could enable high sensitivity tip-enhanced CARS imaging.

The ideal Raman imaging experiment would be a video-rate, high-sensitivity, multiplex Raman setup with high spectral resolution. While none of these techniques are able to achieve that (with the improving technology of lock-in cameras, this should be possible, provided the Raman signal is large enough), they all represent small steps in the direction of increasing sensitivity and thus imaging speed. As laser sources, detector technology, and measurement techniques improve, these and future experiments will continue to approach this ideal Raman imaging setup.

References

[1] M. Cui, B. Bachler, and J. P. Ogilvie. Comparing coherent and spontaneous Raman scattering under biological imaging conditions. *Optics Letters*, 34:773–775, 2009.

[2] Brandon R. Bachler, Meng Cui, Sarah R. Nichols, and Jennifer P. Ogilvie. A comparison between coherent and spontaneous Raman scattering for biological imaging. 7367(1):73670V, 2009.

[3] Brandon R. Bachler, Meng Cui, Sarah R. Nichols, and Jennifer P. Ogilvie. Comparing coherent and spontaneous Raman scattering signals for biological imaging applications. 7569(1):75690O, 2010.

[4] B. R. Bachler, M. E. Fermann, and J. P. Ogilvie. Multiplex Raman induced Kerr effect microscopy. *Optics Express*, (in revision), 2011.